

# **Spatiotemporal dynamics of dryland vegetation photosynthesis and greenness under hydroclimatic extremes**

**by Song Leng**

Thesis submitted in fulfilment of the requirements for  
the degree of Doctor of Philosophy

under the supervision of Prof. Alfredo Huete

University of Technology Sydney

Faculty of Science

## Certificate of original authorship

I certify that the work in this thesis has not previously been submitted for a degree nor has it been submitted as part of requirements for a degree except as fully acknowledged within the text.

I also certify that the thesis has been written by me. Any help that I have received in my research work and the preparation of the thesis itself has been acknowledged. In addition, I certify that all information sources and literature used are indicated in the thesis.

This research is supported by an Australian Government Research Training Program and the Joint CSC-UTS Scholarship between China Scholarship Council and University of Technology Sydney.

Signature of student: Song Leng

Date: 28-10-2021

# Acknowledgements

First of all, I would like to express my deep and sincere grateful to my principle supervisor Distinguished Professor Alfredo Huete for his guidance, assistance, support, and expertise during my four-year doctoral candidature progress. It was a great privilege and honor to study and work under his supervision. I gained and learnt a lot from him, including not only professional knowledge, technical skills, scientific writing, but also developing critical thinking as a Ph.D. researcher. I would also like to thank him for his friendship and empathy.

Also, many thanks to my co-supervisor Professor Qiang Yu who introduced me to Prof. Alfredo when I prepared for the Ph.D. application. Thanks to Professor Derek Eamus, Dr. James Cleverly, Dr. Xuanlong Ma, and Dr. Zunyi Xie for their help and share of their experience. I am also grateful to our team members Dr. Sicong Gao, Dr. Jie He, Dr. Wenjie Zhang, Ekena Rangel, Dr. Ha Nguyen, Dr. Nguyen Ngoc Tran, Dr. Paras Sidiqi, Dr. Leandro Giovannini, Dr. Qiayun Xie, and Yuxia Liu for their invaluable academic and technical support, as well as all my friends Dr. Qinggaozi Zhu, Minxi Zhang, Hong Zhang, Jianguo Li, Rong Gan, Lijie Shi for their help.

My deepest thank to my family for their support and understanding throughout my candidature. Their unconditional support constantly helped me to overcome negative feelings and release pressure during four-year oversea study.

Finally, I appreciate the China Scholarship Council and University of Technology Sydney for their cooperation in providing CSC-UTS Joint Scholarship, which supported my thesis project.

# Publications

Ma, X., Huete, A., Moore, C., Cleverly, J., Huetly, L., Beringer, J., Leng, S., Xie, Z., Yu, Q., and Eamus, D., 2020. Spatiotemporal partitioning of savanna plant functional type productivity along NATT. *Remote Sensing of Environment*, 2020, 246

Tian, F., Wu, J., Liu, L., Leng, S., Yang, J., Zhao, W., and Shen, Q. Exceptional Drought across Southeastern Australia Caused by Extreme Lack of Precipitation and Its Impacts on NDVI and SIF in 2018. *Remote Sensing*, 2019, 12(1), 54

# Table of Contents

<i>Certificate of original authorship</i> .....	<i>ii</i>
<i>Acknowledgements</i> .....	<i>iii</i>
<i>Publications</i> .....	<i>v</i>
<i>Table of Contents</i> .....	<i>vi</i>
<i>List of figures</i> .....	<i>ix</i>
<i>List of tables</i> .....	<i>xii</i>
<i>Abbreviations</i> .....	<i>xiii</i>
<i>Abstract</i> .....	<i>xvi</i>
<b>Chapter 1 Introduction</b> .....	<b>1</b>
<b>1.1 Climate Extremes</b> .....	<b>1</b>
1.1.1 Climate change and climate extremes .....	1
1.1.2 Global carbon cycle under climate change.....	3
<b>1.2 Dryland ecosystem</b> .....	<b>5</b>
1.2.1 Global drylands .....	5
1.2.2 Major dryland biomes in Australia.....	8
<b>1.3 Satellite observation of vegetation</b> .....	<b>14</b>
1.3.1 Reflectance-based vegetation indices.....	14
1.3.2 Land surface phenology .....	17
<b>1.4 Solar-induced chlorophyll fluorescence (SIF)</b> .....	<b>19</b>
1.4.1 Photosynthesis and chlorophyll fluorescence.....	19
1.4.2 Remote sensing of SIF .....	21
<b>1.5 Aims and objectives</b> .....	<b>25</b>
<b>Chapter 2 Response of Dryland Vegetation under Extreme Wet Events with Satellite Measures of Greenness, Fluorescence</b> .....	<b>28</b>
<b>Abstract</b> .....	<b>28</b>
<b>2.1 Introduction</b> .....	<b>29</b>
<b>2.2 Materials and Methods</b> .....	<b>34</b>
2.2.1 Study region .....	34
2.2.2 Satellite Data .....	36
2.2.3 Eddy covariance data.....	39
2.2.4 Wet intensity classification .....	40
2.2.5 Statistics.....	41
<b>2.3 Results</b> .....	<b>42</b>
2.3.1 Wet Pulse Characteristics in 2010-2011 and 2016-2017 .....	42
2.3.2 Response of vegetation per major vegetation type.....	49

2.3.3 SIF-EVI-GPP relationship.....	54
<b>2.4 Discussion .....</b>	<b>58</b>
2.4.1 Spatiotemporal response to extreme wet pulse .....	58
2.4.2 Sensitivity of Mulga and Hummock to water availability .....	60
2.4.3 Assessment with tower-based GPP .....	62
<b>2.5 Conclusions.....</b>	<b>63</b>
<b><i>Chapter 3 Assessing the Impact of Extreme Droughts on Dryland Vegetation by Satellite</i></b>	
<b><i>Solar-induced Chlorophyll Fluorescence .....</i></b>	<b>65</b>
<b>Abstract .....</b>	<b>65</b>
<b>3.1 Introduction.....</b>	<b>66</b>
<b>3.2 Materials and Methods.....</b>	<b>71</b>
3.2.1 Study area .....	71
3.2.2 Satellite data .....	73
3.2.3 Climate Data and Land cover map.....	77
3.2.4 Eddy Covariance data.....	78
3.2.5 Analysis.....	79
<b>3.3 Results.....</b>	<b>81</b>
3.3.1 Spatiotemporal dynamics of the 2018-2019 extreme drought .....	81
3.3.2 Responses of dryland vegetation to drought at diverse severity and time scales.....	86
3.3.3 Comparison of SIF and EVI in response to extreme drought .....	90
3.3.4 Cross-comparison with in-situ measurements.....	93
<b>3.4 Discussion .....</b>	<b>95</b>
3.4.1 Potential of space-borne SIF for drought monitoring over water-limited ecosystems.....	95
3.4.2 Dynamics of dryland vegetation under different drought scenarios .....	98
<b>3.5 Conclusions.....</b>	<b>100</b>
<b><i>Chapter 4 Spatiotemporal variations of dryland vegetation phenology revealed by satellite-</i></b>	
<b><i>observed fluorescence and greenness across the North Australian Tropical Transect .....</i></b>	<b>101</b>
<b>Abstract .....</b>	<b>101</b>
<b>4.1 Introduction.....</b>	<b>102</b>
<b>4.2 Materials and Methods.....</b>	<b>107</b>
4.2.1 Study area .....	107
4.2.2 Satellite data .....	108
4.2.3 Climate Data and Land cover map.....	111
4.2.4 Eddy Covariance data.....	112
4.2.5 Phenological metrics .....	112
<b>4.3 Results.....</b>	<b>115</b>
4.3.1 Seasonal and inter-annual variations over local sites.....	115
4.3.2 Biogeographic patterns of vegetation phenology.....	119
4.3.3 Interaction between environmental drivers and vegetation variables .....	124
<b>4.4 Discussion .....</b>	<b>126</b>
4.4.1 Ground interpretations of the satellite-observed vegetation phenology.....	126
4.4.2 Spatial patterns of vegetation phenology .....	128
<b>4.5 Conclusions.....</b>	<b>130</b>

**Chapter 5 Conclusions..... 131**

**5.1 Summary of key methodology, results, and conclusions.....131**

5.1.1 Chapter 2 .....131

5.1.2 Chapter 3 .....132

5.1.3 Chapter 4 .....133

**5.2 Limitation and future research directions .....134**

**References ..... 136**

# List of figures

Figure 1-1 Global distribution of drylands based on observations (reanalysis combined with station and satellite observations) for the 1981–2010 baseline (Koutroulis 2019). .....	6
Figure 1-2 Spatial distribution of major dryland biomes in Australia based on Australia’s National Vegetation Information System - Major Vegetation Groups (Version 5). .....	9
Figure 1-3 (a) the Mulga viewed at ground level; (b) the Mulga viewed from above the canopy at the Alice Spring Mulga (AU-ASM) eddy covariance tower (Eamus et al. 2016).....	10
Figure 1-4 Hummock grasslands during (a) dry and (b) wet growing seasons (Rammig & Mahecha 2015).....	13
Figure 1-5 Typical vegetation reflectance spectrum (Roman & Ursu 2016) .....	15
Figure 1-6 Schematic diagram of photosynthesis and chlorophyll fluorescence (Baker, 2008) .....	20
Figure 1-7 Spatial comparison between TROPOMI, GOME-2, and OCO-2 SIF in the Nile region based on data acquired between 23 and 29 November 2017 (Köhler et al. 2018) .....	23
Figure 2-1 Map of reclassified major vegetation groups over central Australia (map source: NVIS Version 5.0). Black dot and triangle represent AU-ASM, AU-TTE flux tower sites respectively; Black pentagams refer to the three selected test-points as well as the extent of 3×3 pixels labelled as blue dashed square; Grids refer to a fishnet at 0.5° spatial resolution, consistent with pixel size of GOME-2 SIF data. Top-left figure displays the locations of the study area over Australian continent (image source: Google Earth). Left column shows the spatial distributions of relative homogenous pixels of three major biomes at a 0.5° resolution. (g. refers to grassland, w. refers to woodland, s. refers to shrubland, selection percentages are listed in parentheses).....	35
Figure 2-2 The region-wide mean seasonal cycle of (a) precipitation, (b) soil moisture, (c) EVI, and (d) SIF over study area during 2010-2011, 2016-2017 and non-wet years. The shaded area represent ±1 standard deviation ( $\sigma$ ). The vertical rectangles refer to extreme wet periods of 2010-2011 (yellow) and 2016-2017 (blue) respectively. ....	44
Figure 2-3 Spatial patterns of standard anomalies of (a) precipitation, (b) SM, (c) SIF, and (d) EVI during 2010-2011 wet pulse as well as following three months. Bottom panel shows frequency map of each SA (standard anomaly) category of the corresponding variable during the five months.....	46
Figure 2-4 Spatial patterns of standard anomalies of (a) precipitation, (b) SM, (c) SIF, and (d) EVI during 2016-2017 wet pulse as well as following three months.....	47
Figure 2-5 Spatial characteristics of wet pulses. (a, b) Spatial pattern of wet intensity during 2010-2011 and 2016-2017 wet pulses; (c, d) percentages of each wet level over three major vegetation types.....	49
Figure 2-6 Seasonal variation in spatial averaged anomalies of EVI and SIF of major biomes by each wet level in 2010-2011 (a-f) and 2016-2017 (g-l). Colorful areas represent ±1 standard deviation of the corresponding wet level. The vertical rectangles refer to extreme wet periods (2-month). .....	50
Figure 2-7 Cross-site relationship (a-d) between mean annual precipitation, soil moisture, SIF, EVI over three selected pixels. Vertical dashed lines refer to the multi-year mean of precipitation and soil moisture; Solid lines refer to the linear regression and the coefficient of determination ( $r^2$ ) of each TP are listed with corresponding color. (e-j) Seasonal trajectory between SM and SIF, EVI during wet season (Nov-Apr). k refers to the slopes of linear regression between SM and SIF, EVI during wet year and non-wet year.....	53
Figure 2-8 Relationship between soil moisture and EVI, SIF (a) Boxplot of maximum correlation coefficients between monthly Soil Moisture and EVI, SIF during 2007-2017 along with (b) the	

corresponding time lags (months). Above the dashed line represents p value below than 0.01 and vice versa.....54

Figure 2-9 Comparison of satellite observation and tower-based measurement. (a, b) Seasonal variation in monthly GPP over AU-ASM and AU-TTE; (c-g) relationship between normalized GPP and SIF, EVI over flux tower sites during wet pulse years (2010-2011, 2016-2017) and non-wet year mean (2012-2015).....56

Figure 2-10 Coefficients of determination between multi-year series of tower-based GPP and EVI, EVI and SIF, GPP and SIF at a range of spatial resolution from 0.25 km to ~50 km (0.5°). Dashed orange rectangle refer to the footprints of satellite observation overlapped between AU-ASM and AU-TTE. ....57

Figure 3-1 (a) Land cover map based on national Dynamic Land Cover Dataset (DLCD). (b) Spatial pattern of aridity index. Black triangles refer to five flux tower sites. ....72

Figure 3-2 (a) Region-wide mean monthly SPEI<sub>6-month</sub> along with pixel counting under extreme dry (SPEI ≤ -2) from 2000-2019 and (b) monthly SPEI<sub>1-month</sub> during 2018-2019. ....82

Figure 3-3 (a) Spatial pattern of drought severity based on SPEI<sub>6-month</sub> during 2018-2019 monsoon season (November - April). (b) Pixel-wise number of extreme-dry months during 2018-2019 monsoon season based on SPEI<sub>1-month</sub>. Four pairs of ROIs (1-4) are shown in Fig.3a. The black boundary represents the extent of extreme (within) and medium (outside) dry in 2018-2019.....83

Figure 3-4 The spatially-averaged seasonal cycles of GOME-2A SIF, SIF<sub>PAR</sub>, MODIS EVI, and FluxSat GPP within (a, e, i, k) medium and (b, f, j, l) extreme dry extent from July 2018 to June 2019. The grey curves represent the monthly multiyear mean of each variable between 2007 and 2018. Vertical lines refer to ±1 standard deviation. (c, d, g, h) the spatially-averaged seasonal profiles of SIF, SIF<sub>PAR</sub> from TROPOMI and GOME-2B in 2018-2019 respectively. ....84

Figure 3-5 The spatial distributions of the standardized anomalies of IMERG precipitation, ERA-5 surface and root zone soil moisture, MODIS LST, GOME-2A SIF, SIF<sub>PAR</sub>, EVI, and FluxSat GPP averaged from November 2018 to March 2019. Pixel density of vegetation variables within the extent of extreme and medium dry respectively are shown in right column.....86

Figure 3-6 Region-wide seasonal cycles and anomalies of (a, c, g, i) EVI and (b, d, h, j) SIF within four pairs of ROIs in 2018-2019. Seasonal profiles of SIF and EVI within (e, f) ROI-2 in 2012-2013 and (k, l) ROI-4 in 2015-2016. Bottom panels of each figure refer to the anomalies of SIF or EVI relative to climatology (2007-2018). ....88

Figure 3-7 The boxplot of anomalies of (a) EVI and (b) SIF by different extreme-dry months along all pixels grouped by aridity index during 2018-2019.....90

Figure 3-8 The boxplot of anomalies of EVI and SIF under extreme and medium drought along all pixels grouped by major biome types and aridity index during 2018-2019.....91

Figure 3-9 (a, b, c) Monthly and (d, e) 16-day time series of the percentage of drought-induced vegetation reduction indicated by EVI, SIF, and SIF<sub>PAR</sub> under moderately (< -0.5σ), severely (< -1σ) and extremely (< -2σ) negative anomalies. σ indicates the standard deviation of the monthly SIF, EVI during 2007–2018 as well as 16-day SIF/EVI during 2013–2018. The text of x-axis in Fig.9d, 8e refer to the day of year (DOY) from November 2018 to March 2019.....92

Figure 3-10 Seasonal cycles of monthly tower-based GPP, satellite-observed SIF, EVI over five flux tower sites from July 2018 to June 2019 as well as multiyear mean. The grey area refers to ±1 standard deviation. ....94

Figure 3-11 Relationship between tower-based GPP and satellite-based SIF, EVI in 2018-2019 across five flux tower sites at different spatial (0.5°, 0.05° grid) and temporal (monthly, 16-day) resolution. (p value < 0.001).....95

Figure 4-1 Land cover map of the Northern Australian Tropical Transect (NATT) study area. Black triangles refer to the five flux tower sites. ....108

Figure 4-2 Schematic diagram of phenological metrics retrieval. The curve refers to the seasonal SSA re-reconstructed EVI or SIF profile at daily scale. SOS: the start of growing season; POS: the peak of growing season; EOS: the end of growing season; RSP: the rate of spring green-up; RAU: the rate of autumn senescence.....114

Figure 4-3 Time series of SSA-reconstructed tower-based GPP, GOME-2 SIF, MODIS EVI over 5 flux tower sites. R-squared ( $r^2$ ) refer to the correlations between GPP and EVI (green), GPP and SIF (orange) respectively. Vertical dashed lines refer to the peak of growing season in each hydrological year. ....117

Figure 4-4 Seasonal cycle (mean) of tower-based GPP, GOME-2 SIF, MODIS EVI, and EVI×PAR over 5 selected local sites during 2014-2019. Curves are normalized with respect to unity at the maximum annual value. Satellite observations were extracted within a 3×3 window centered at each flux tower site (SIF: 1.5°×1.5°, EVI and EVI×PAR: 0.15°×0.15°).....118

Figure 4-5 Spatial patterns of vegetation phenology based on EVI over the NATT study area across three representative hydrological years (2014-2015 normal year, 2016-2017 wet year, 2018-2019 dry year). The filled pixels (grey shaded areas) are either water body or without detectable phenology. 121

Figure 4-6 Spatial patterns of vegetation phenology based on SIF over the NATT study area across three representative hydrological. (2014-2015 normal year, 2016-2017 wet year, 2018-2019 dry year). The filled pixels (grey shaded areas) are either water body or without detectable phenology.....123

Figure 4-7 Scatter plot between spring green-up rates (RSP) and autumn senescence rates (RAU) of EVI and SIF among four major biomes across entire study region. Red dashed lines refer to -1:1 diagonal.....124

Figure 4-8 Relationship between environmental drivers and vegetation variables averaged by four major biome types across NATT. (p value < 0.001) .....126

# List of tables

Table 1-1 Summary of primary satellite-based instrument for SIF retrieval.....	23
Table 2-1 Summary of wet pulse intensity classification.....	40
Table 4-1 Summary of differences (days) in SOS and EOS derived from SIF, EVI compared with that derived from tower-based GPP. MAE: mean absolute error. Negative values represent an earlier green-up (SOS) or senescence (EOS) of SIF, EVI relative to that of GPP. ....	118

# Abbreviations

AI	Aridity Index
AU-ASM	Alice Springs Mulga
AU-Dry	Dry River
AU-How	Howard Springs
AU-Stp	Sturt Plains
AU-TTE	Ti Tree East
CERES	Cloud and Earth's Radiant Energy System
CPA	Cumulative Precipitation Anomalies
DJF	December-January-February
DLCD	Dynamic Land Cover Dataset
DOY	Day of Year
ENSO	El Niño-Southern Oscillation
ESA	European Space Agency
EVI	Enhanced Vegetation Index
EUMETSAT	European Organisation for the Exploitation of Meteorological Satellites
fPAR	Fraction of Photosynthetically Active Radiation
GOME-2	Global Ozone Monitoring Experiment-2
GOSAT	Greenhouse Gases Observing Satellite
GPP	Gross Primary Productivity
GRACE	Gravity Recovery and Climate Experiment

IMERG	Integrated Multi-Satellite Retrievals for Global Precipitation Measurement
LAI	Leaf Area Index
LSP	Land Surface Phenology
LST	Land Surface Temperature
LUE	Light Use Efficiency
MVGs	Major Vegetation Groups
NASA	National Aeronautics and Space Administration
NATT	North Australian Tropical Transect
NDVI	Normalized Difference Vegetation Index
NEP	Net Ecosystem Production
NIR	Near Infra-Red
NVIS	National Vegetation Information System
OCO-2	Orbiting Carbon Observatory-2
PAR	Photosynthetically Active Radiation
PET	Potential Evapotranspiration
POS	Peak of Growing Season
RAU	Rate of Autumn Senescence
ROI	Region of Interest
RSP	Rate of Spring Green-up
SA	Standardized Anomaly
SD	Standard Deviation
SIF	Sun-Induced chlorophyll Fluorescence
SM	Soil Moisture
SOS	Start of Growing Season
SPEI	Standardized Precipitation Evapotranspiration Index
TPs	Test-pixels
TRMM	Tropical Rainfall Measuring Mission

TROPOMI	TROPOspheric Monitoring Instrument
TWSA	Total Water Storage Anomaly
VI	Vegetation Indices
VPD	Vapour Pressure Deficit
WUE	Water-Use Efficiency

# Abstract

Australia's dryland ecosystems play a critical role in regulating the climate system and considerably influence the interannual variability in global carbon cycle. However, the dynamics of dryland vegetation under climate variability and extreme events have not been as thoroughly investigated as in other ecosystems. Spaceborne solar-induced chlorophyll fluorescence (SIF) provide a fresh means to evaluate vegetation photosynthetic activity and detect vegetation stress. Considering its spatially coarse resolution, studies with reference to the application of SIF over heterogeneous dryland ecosystem are rarely reported.

The main goal of this thesis is to explore the spatial and temporal dynamics of Australia's dryland vegetation under hydro-climatic extremes using satellite-estimated fluorescence and greenness. To achieve this goal, I first utilized a strong wet pulse in 2016-2017 as well as in the 2011 big wet period as natural experiments to assess the response of major dryland biomes in central Australia. Next, I investigated the impact of a recent extreme drought on spatiotemporal variability of Australia's dryland vegetation indicated by multi-source satellite-based SIF. Finally, I analysed the spatial pattern and seasonal variations in dryland vegetation phenology under climate variability.

The results showed semiarid ecosystems to have the largest variability and were most sensitive to climate extremes. SIF derived from the Global Ozone

Monitoring Experiment-2 (GOME-2) at  $0.5^\circ$  spatial resolution has an insufficient capacity for capturing spatiotemporal dynamics over xeric central Australia as a result of low signal level and high retrieval noise. In contrast to humid ecosystems, both SIF and enhanced vegetation index (EVI) simultaneously captured the declines of arid/semiarid plant growth from the beginning of extreme drought events at 16-day scale. SIF data retrieved from TROPospheric Monitoring Instrument (TROPOMI) at a  $0.05^\circ$  spatial grid exhibits promising capability of mapping and characterizing the dynamics of heterogeneous dryland vegetation in future.

This thesis highlights that the incorporation of satellite-observed greenness and fluorescence can potentially contribute to an improved understanding of dryland vegetation dynamics and can advance our ability to detect ecosystem alterations under future changing climates.

# **Chapter 1 Introduction**

## **1.1 Climate Extremes**

### **1.1.1 Climate change and climate extremes**

Accompanied by rapidly increasing anthropogenic emissions of greenhouse gases, the climate has considerably shifted, especially as regards temperature, precipitation, and CO<sub>2</sub> concentration (Stocker et al. 2014). Climate change is a long-term change in the average weather patterns that have come to define Earth's local, regional and global climates. Climate change, inevitably leading to alteration in climate variability and frequency of extreme events (Thornton et al. 2014), is a major threat to marine and terrestrial ecosystems, biodiversity, as well as human society (Hiddink, Burrows & García Molinos 2015; Knapp et al. 2015). Globally, anomalies of seasonal mean temperature have shifted toward a steep rising trend (Hansen, Sato & Ruedy 2012). Therefore, improvements in the science and observations of climate change contribute to an enhanced understanding of the inherent variability of Earth's climate system and its probable response to human and natural impacts (Moss et al. 2010).

In regard to changes under a future climate, global warming is expected to intensify the hydrological cycle (Wu, Christidis & Stott 2013), and climate modelling studies suggest that an increase in heavy rainfall has likely occurred over the majority of global land in the 21st century (Madsen et al. 2014).

Generally, precipitation amounts diverge from multiyear mean by

approximately 40% in extreme wet years and 30% in extreme dry years over humid regions, and the magnitude of variations rose to 60% for dry years and to 150% for wet years in water-limited areas (Knapp et al. 2015).

Extreme weather or extreme climate events includes unexpected, unusual, severe, or unseasonal weather; weather at the extremes of the historical distribution—the range that has been seen in the past. Climatic extreme events may have substantial influences on sectors closely associated with climate, such as water resource and agriculture, food security, and tourism, and concomitantly in countries whose economies primarily rely on such sectors (Trenberth, Fasullo & Shepherd 2015). Scientific studies have reported the widespread consequences of climate extremes on terrestrial ecosystems as well as global carbon cycle, for instance the 2005 and 2015-2016 extreme drought over Amazon rainforest (Phillips et al. 2009; Yang et al. 2018), the La Nina with intense wetness over almost entire continent of Australia in 2010-2011 (Boening et al. 2012; Poulter et al. 2014), and the 2012 summer drought across the contiguous United States (Wu et al. 2018). Through examining the response of grassland productivity under extreme drought and rainfall, Kath et al. (2019) found grassland decline and recovery trends were congruent for hydro-climatic variables. Along with the increasing frequency, intensity, and duration of extreme heat waves, carbon sink of extensive regions in Australia is possibly non-sustainable in a future climate (Van Gorsel et al. 2016). Besides terrestrial

ecosystems, a marine heatwave in 2010-2011 leads to substantial losses from the world's largest seagrass carbon stocks in western Australia (Arias-Ortiz et al. 2018). Understanding the response of vegetation to climate extreme is of great importance for quantifying the carbon-cycle climate feedback and highly relevant to climate change assessments (Zscheischler et al. 2014).

### **1.1.2 Global carbon cycle under climate change**

The carbon cycle is the biogeochemical cycle by which carbon is exchanged among the biosphere, pedosphere, geosphere, hydrosphere, and atmosphere of the Earth. Global carbon cycle performs a critical role in our environment (Braswell et al. 1997; Cao & Woodward 1998), and carbon is cycled among five major pools: atmosphere, ocean, biosphere, soil organic matter and lithosphere (Dixon et al. 1994). Interannual variations in carbon uptake are associated with variations in hydro-climate that affect net ecosystem productivity. Reichstein et al. (2013) emphasized the probability that climate extremes and their influences on the global carbon budget may result in an amplification of positive climate-carbon cycle feedbacks.

Drought can be considered as a strictly meteorological phenomenon. It can be evaluated as a meteorological anomaly characterized by a prolonged and abnormal moisture deficiency. Extreme drought and heat wave are the major trigger of the reduction in the terrestrial carbon sink (Ma et al. 2012). As a result of the century drought during 2000-2004, a remarkable drying of the terrestrial

biosphere was observed and the area-integrated strength of the western North American carbon sink decreased by 30-298 Tg C yr<sup>-1</sup> (Schwalm et al. 2012). During the 2003 European extreme drought, the reduction in the amount of carbon absorbed was estimated to be equivalent to the amount of CO<sub>2</sub> absorption in the past three to five years under non-drought condition (Reichstein et al. 2007; Vetter et al. 2008). Besides, the aforementioned 2015 Amazon drought-induced fires exceeded the extent from previous years, highlighting the fact that large swaths of the Amazon may burn in a hotter and drier future, resulting in massive carbon emission (Aragão et al. 2018).

On the other side, the amount of extreme precipitation is projected to increase about three times as much as average precipitation, with diverse regional patterns (Sillmann et al., 2019). Extreme wet event is likewise a dominant cause of the variations of biomass carbon budget. As record-breaking rains in 2010-2011 triggered a boom in plant growth, it caused a massive global land carbon sink anomaly, of which half was contributed by Australia (Poulter et al. 2014). Compensating for more than 90% of the drought-induced losses, substantially enhanced growth after extreme wetness is observed and sustained 1 to 5 years over global arid/semiarid regions (Jiang et al. 2019). The interannual variability of aboveground biomass carbon in water-limited ecosystems were found to primarily agree with rainfall patterns in southern Africa and northern Australia, partially ascribed to El Niño Southern Oscillation and La Niña conditions, such

as two peaks during two intensely wet La Niña conditions (2000/2001, 2010/2011) of the previous twenty years (Liu et al. 2015). Through changes in the strength of carbon sink or losses, the striking global carbon balance in turn influence climate system (Frank et al. 2015).

Owing to the impact of multiple large-scale climate modes such as the El Niño-Southern Oscillation and the Indian Ocean Dipole (Xie et al. 2019; Xie et al. 2016), Australia is characterized by extreme climate variability. As prolonged drought and severe wet events are projected to increase both frequently and intensely (Huang et al. 2016; Min et al. 2011) that exacerbate profound impacts on water resources, ecosystems, economy and society (Evans, Meng & McCabe 2017), it is essential to enhance understanding of Australia's ecosystem functioning under future changing climate.

## **1.2 Dryland ecosystem**

### **1.2.1 Global drylands**

Drylands are commonly defined as zones where precipitation is balanced by evaporation from surfaces and transpiration by vegetation (Huang et al. 2017; Middleton & Thomas 1997). Dryland systems, including cultivated lands, scrublands, shrublands, grasslands, savannas, semi-deserts and true deserts, are ecosystems characterized by a lack of water. Globally, dryland vegetation, covering approximately 41% of the land surface (Reynolds et al. 2007), is exceedingly susceptible to climate conditions, mainly owing to the chronic

physiological stress (Walker, De Beurs & Wynne 2014). Besides, drylands account for about 40% of the global net primary production (Grace et al. 2006; Wang et al. 2012), and support more than one third of the population worldwide (Huang et al. 2017; Reynolds et al. 2007). Figure 1-1 displays the global distribution of drylands during 1981-2010 (Koutroulis 2019). Based on satellite observations combined with field measurement, the estimation of drylands is approximately 47% of total Earth's lands, of which 9.6% are characterized as hyper-arid, 13.3% arid, 16.6% semiarid and 7.5% dry-subhumid, defined by the ratio between precipitation and potential evapotranspiration (Koutroulis 2019). The drylands cover the Sahara Desert, Arabian Peninsula, Central and East Asia, western United States, the west coast of South America, and the majority of Australia's continent (Huang et al. 2016; Koutroulis 2019).

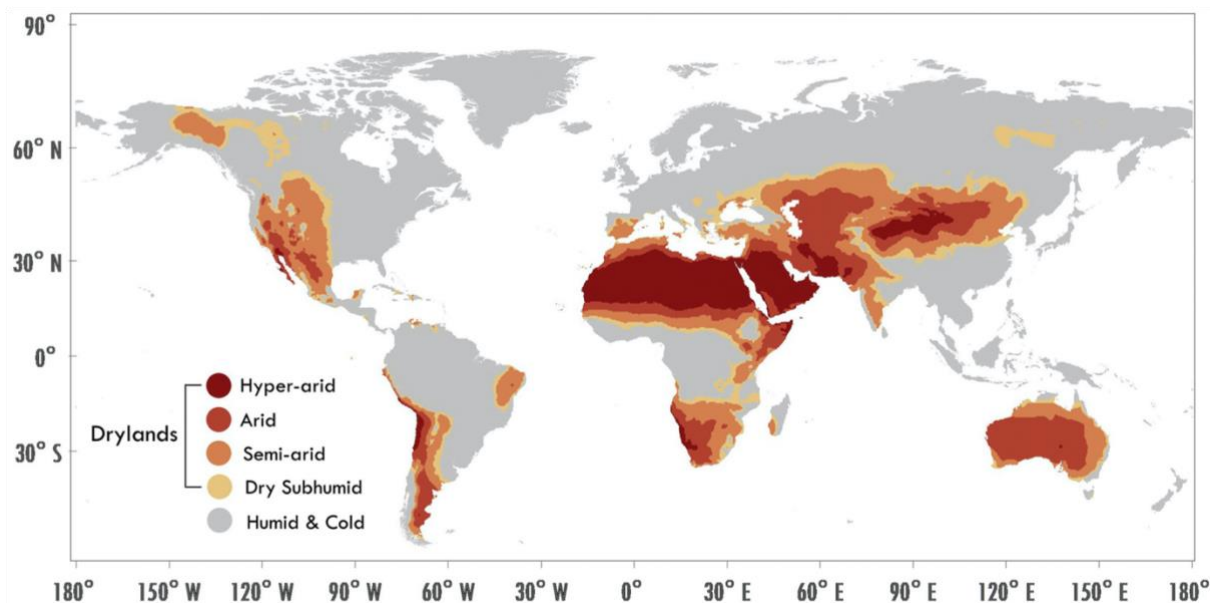


Figure 1-1 Global distribution of drylands based on observations (reanalysis combined with station and satellite observations) for the 1981–2010 baseline (Koutroulis 2019).

With rising aridity under global warming as well as promptly increasing human population, worldwide dryland expansion has been observed during the recent decades (Huang et al. 2016). Research suggest that the areal coverage of drylands would rise by additional 7% of the total land by the end of this century under climate change (Koutroulis 2019).

Dryland ecosystems are highly susceptible to environmental change, and the major drivers dominating the variability of dryland vegetation comprise climate, fire regime, grazing, and agriculture (Andela et al. 2013). The principal climatic process dominating the variability of dryland vegetation is water availability controlled by precipitation and evapotranspiration (Gonsamo et al. 2019). The significant spatiotemporal variations in dryland biomes with diverse tree-grass ratios implies that grass-containing xeric savanna is especially sensitive and vulnerable to hydro-climatic variability (Ma et al. 2020). Given the mixed and heterogeneous arrangement of water-limited ecosystems confounds the extraction of phenology. Walker, De Beurs & Wynne (2014) assessed the dynamics of dryland vegetation phenology across an elevation gradient in Arizona, USA through fusing satellite imagery, which was dependent on the precipitation patterns of growing season. On the basis of the complex composition of plant functional types as well as low rates of biological activity, the characteristic phenology responses of dryland vegetation to baseline climate

conditions as well as climatic extremes have not been as thoroughly examined as in humid temperature-driven ecosystems (Walker, De Beurs & Wynne 2014).

### **1.2.2 Major dryland biomes in Australia**

Australia is the driest inhabited continent worldwide, of which 70% is encompassed with arid or semiarid ecosystems across the vast interior and dominated by three major biomes along a woodland-savanna-grassland continuum (Bowman, Boggs & Prior 2008; Cleverly et al. 2013; Cleverly, Eamus, Van Gorsel, et al. 2016; Xie et al. 2016). Figure 1-2 presents the spatial distributions of major dryland biomes in Australia based on Australia's National Vegetation Information System - Major Vegetation Groups (NVIS-MVGs).

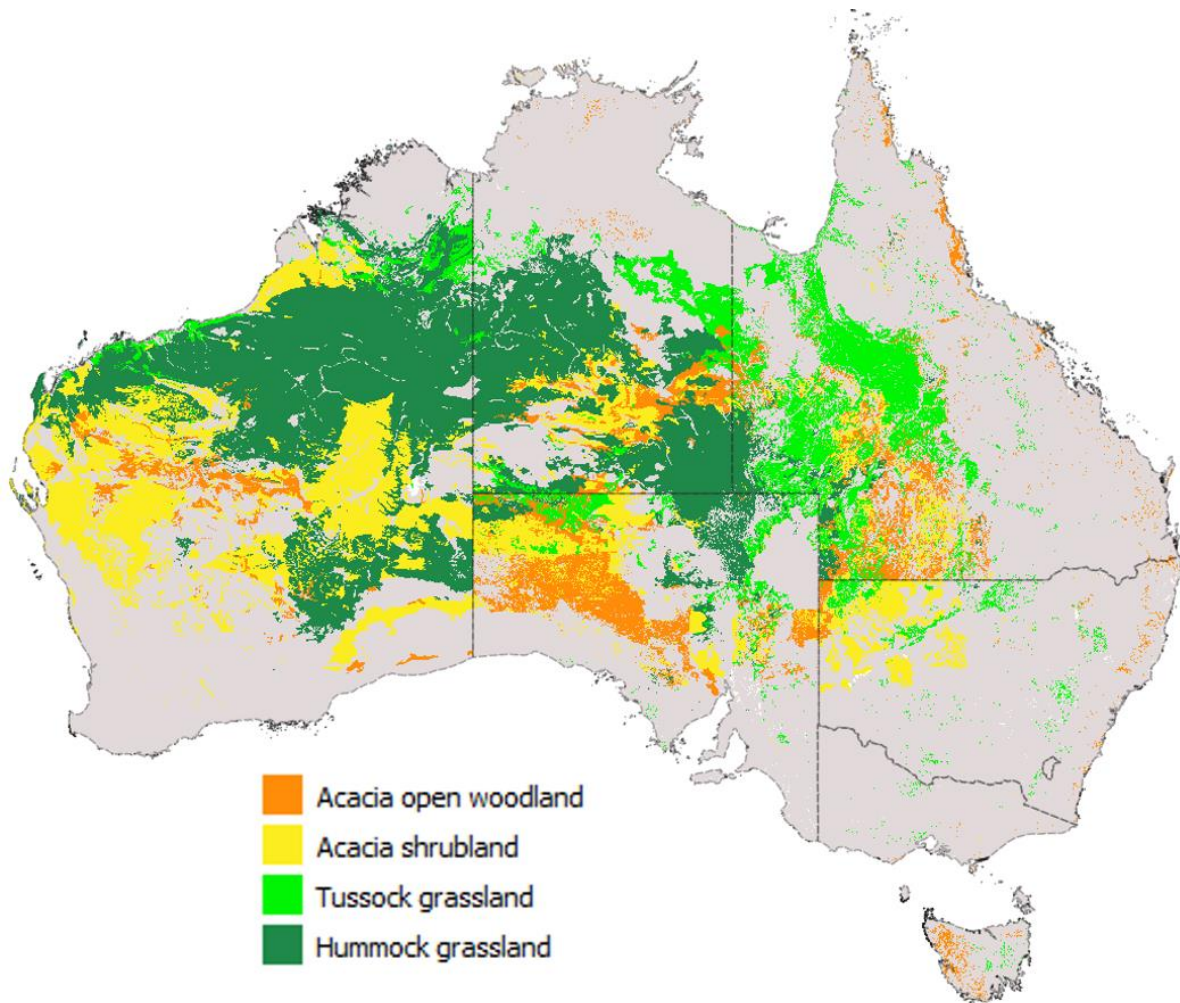


Figure 1-2 Spatial distribution of major dryland biomes in Australia based on Australia's National Vegetation Information System - Major Vegetation Groups (Version 5).

### 1.2.2.1 Mulga woodlands/shrublands

Mulga woodlands/shrublands, covering approximately 20%~25% of the continental land area from tropical and sub-tropical arid to semi-arid interior of Australia (Bowman, Boggs & Prior 2008), are comprised of a complex of closely related *Acacia* spp. (Eamus et al. 2016). Mulga trees range in height (2-10 meters), and growth forms are likewise highly dynamic varying from a very sparse canopy to a relatively closed canopy (Eamus et al. 2016). Figure 1-3 shows the images of Mulga woodlands viewed (a) at ground level and (b) from

above the canopy around the Alice Spring Mulga (AU-ASM) eddy covariance tower site (Eamus et al. 2016).

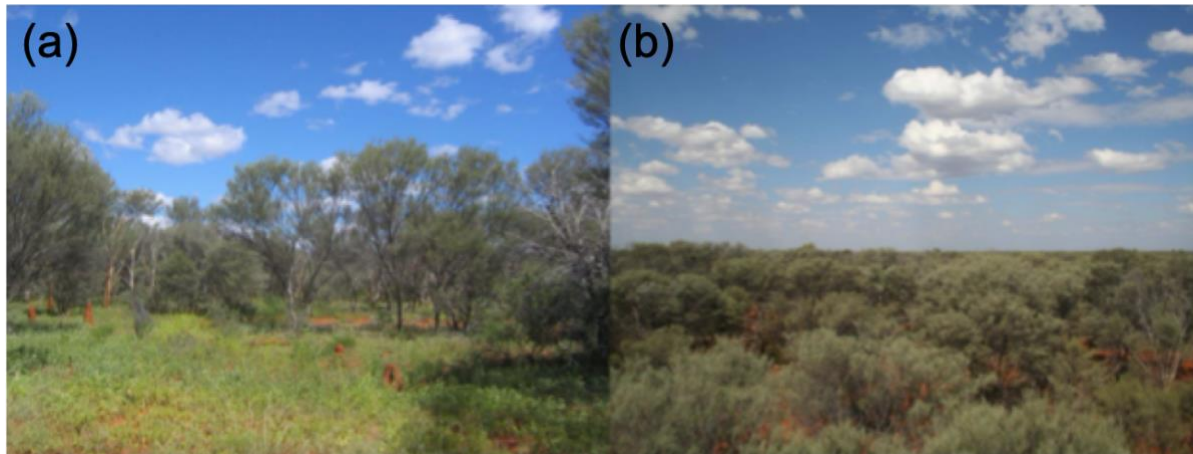


Figure 1-3 (a) the Mulga viewed at ground level; (b) the Mulga viewed from above the canopy at the Alice Spring Mulga (AU-ASM) eddy covariance tower (Eamus et al. 2016).

Owing to the demand of substantial moisture storage capacities in the substrate, Mulga usually is distributed on flat terrain with low rates of drainage past the relatively shallow roots (Cleverly, Eamus, Restrepo Coupe, et al. 2016; Eamus et al. 2016). The carry-over of soil moisture, as potential water source for supporting physiological activity during dry spell, can affect phenology and productivity of Mulga (Chen et al. 2016; Flanagan & Adkinson 2011). Similar with other arid/semiarid biomes, photosynthetic production in Mulga woodlands is primarily driven by pulses of precipitation (Cleverly, Eamus, Restrepo Coupe, et al. 2016; Cleverly, Eamus, Van Gorsel, et al. 2016). Interannual variability in rainfall is the predominant cause of interannual differences in the strength of carbon sink in Mulga woodlands (Eamus et al. 2016). Utilizing the normalised difference vegetation index (NDVI) from satellite observation,

greenness in undisturbed Mulga was found to be delayed behind precipitation by approximately 0-10 days (Moreno-de las Heras et al. 2012). With particular emphasis on eddy covariance data of landscape fluxes of CO<sub>2</sub>, Eamus et al. (2016) demonstrated that Mulga contributed markedly to the large 2011 anomaly in terrestrial carbon uptake. By contrast, during the following drought of 2012-2013, the net ecosystem production (NEP) in Mulga woodlands was closely to zero (Cleverly et al. 2013), mainly attributed to storage of soil moisture within the root zone (Cleverly, Eamus, Restrepo Coupe, et al. 2016). In spite of nearly equal amount of precipitation, the temporal distribution of rainfall during wet season has also remarkable impacts on the patterns of soil moisture and therefore the response of Mulga (Cleverly, Eamus, Restrepo Coupe, et al. 2016).

Apart from the determinant of rainfall on phenology and productivity, the growth of Mulga can be suppressed by canopy temperatures that surpass Mulga's thermal limit (38°C) during hot-summer monsoon season (Cleverly, Eamus, Van Gorsel, et al. 2016; Nix & Austin 1973). On account of correspondence between meteorological drivers and precipitation, the influences of air temperature, vapour pressure deficit (VPD), and solar radiation on photosynthetic production of Mulga are strongly associated with variations in soil moisture (Cleverly et al. 2013). Regardless of wet or dry season, inherent water-use efficiency (WUE) in Mulga largely relies on soil moisture content,

demonstrating the coordinated regulation of NEP and evapotranspiration by soil water availability, VPD, and temperature (Eamus et al. 2013; Eamus et al. 2016).

#### **1.2.2.2 Hummock grasslands**

Hummock grasslands, the largest single vegetation group covering more than 20% of Australia's land surface, are typically distributed in areas with annual rainfall ranging from 150 mm to 350 mm (Dickman et al. 2014). They are ecologically vital and provide shelter for a large diversity of reptiles and small marsupials in the interior of Australia (Anderson et al. 2019; Pianka 1972).

Hummock grasslands (*Triodia* spp.), often less than 0.5 m high with rigid and spiny foliage, are characterised by flammable, perennial, xerophytic, hummock-forming C<sub>4</sub> grasses (Nicholas, Franklin & Bowman 2011), commonly with emergent trees or shrubs with a foliage of cover less than 10% (Beard et al. 2013). In the northern arid areas where wet growing season occurs in hot summer, the landscapes of hummock grasses are regularly punctuated by *Acacia*, *Corymbia* and *Eucalyptus* woodlands (Dickman et al. 2014). The pictures of Hummock grasslands during dry and wet growing seasons are shown in Figure 1-4 (Rammig & Mahecha 2015).

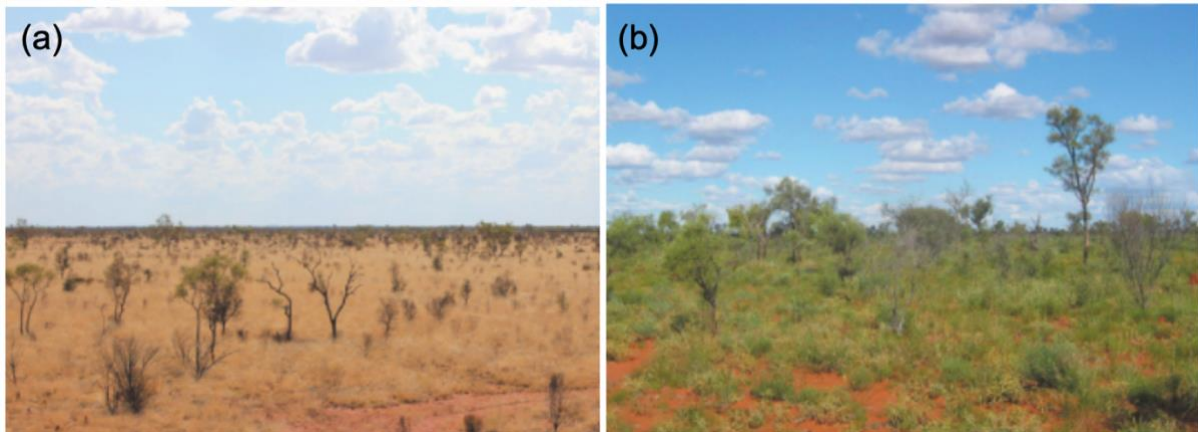


Figure 1-4 Hummock grasslands during (a) dry and (b) wet growing seasons (Rammig & Mahecha 2015)

Rather than common grasses, growth form of Hummock is functionally that of a shrub, whose roots are able to reach depths of exceeding 10 m (Reid, Hill & Lewis 2008). The growth rates of hummock grasses are dynamic and strongly related to rainfall. The large variations of the Australian climate periodically provoke multi-year heavy rainfall alternating with several years of extreme dry spell, that rise hummock's flammability (Bliege Bird, Bird & Codding 2016). Density, height and form of hummock grasses, as well as composition of co-occurring species, rely on fire regimes (Allan & Southgate 2002).

The abrupt ecotone between spinifex-dominated hummock grasslands and mulga-dominated woodlands/shrublands is a noteworthy characteristic of the landscape over extensive inland Australia (Griffin & Hodgkinson 1986).

Likewise, semiarid ecosystems including hummock grasses contributed largely to the 2011 global carbon sink anomaly (Ahlström et al., 2015; Rammig & Mahecha, 2015). The following drought in 2011-2012 promptly diminished the massive net

carbon uptake over central Australia (Ma et al. 2016), of which Corymbia savanna interspersed with Hummock grass was a very large net carbon source in contrast to the extreme drought tolerance of Mulga as approximately carbon neutral (Cleverly, Eamus, Van Gorsel, et al. 2016). Therefore, as a result of their intrinsic sensitivity and complexity, the spatiotemporal dynamics of biome-specific dryland vegetation under climate variability and extreme climatic events remains challenging (Walker, De Beurs & Wynne 2014).

### **1.3 Satellite observation of vegetation**

#### **1.3.1 Reflectance-based vegetation indices**

Satellite-based sensors providing large-scale observations of ecosystem states and landscapes dynamics, are regarded as priceless tools to support filling the spatial gaps of in-situ measurements, and refine the accuracies of models (Broich et al. 2014). Fundamentally, the properties of electromagnetic radiation show that different forms of radiation energy are able to provide diverse information concerning terrain surface characteristics (Campbell & Wynne, 2011) and that different applications of earth observation are probably benefit from sensing in dissimilar sections of the radiation range (Ustin et al. 2004).

The reflectance features of plants depend on a synthetical association of leaf biochemistry and canopy properties including the orientation and the structure (Asner & Martin 2008). The amount of energy reflected for a specific wavelength is determined by photosynthetic pigments, leaf water content,

explicit leaf area, leaf area index, leaf angle distribution and canopy architecture (Asner & Martin 2008). Biophysical characteristics, for instance leaf area index, biomass, chlorophyll content, and fraction of absorbed radiation, are among the most significant vegetation parameters for ecological studies, and for depicting vegetation (Lu et al. 2003; Qi et al. 1995; Yang et al. 1998). One eventual target is the assessment of biomass and the monitoring of vegetation changes therein.

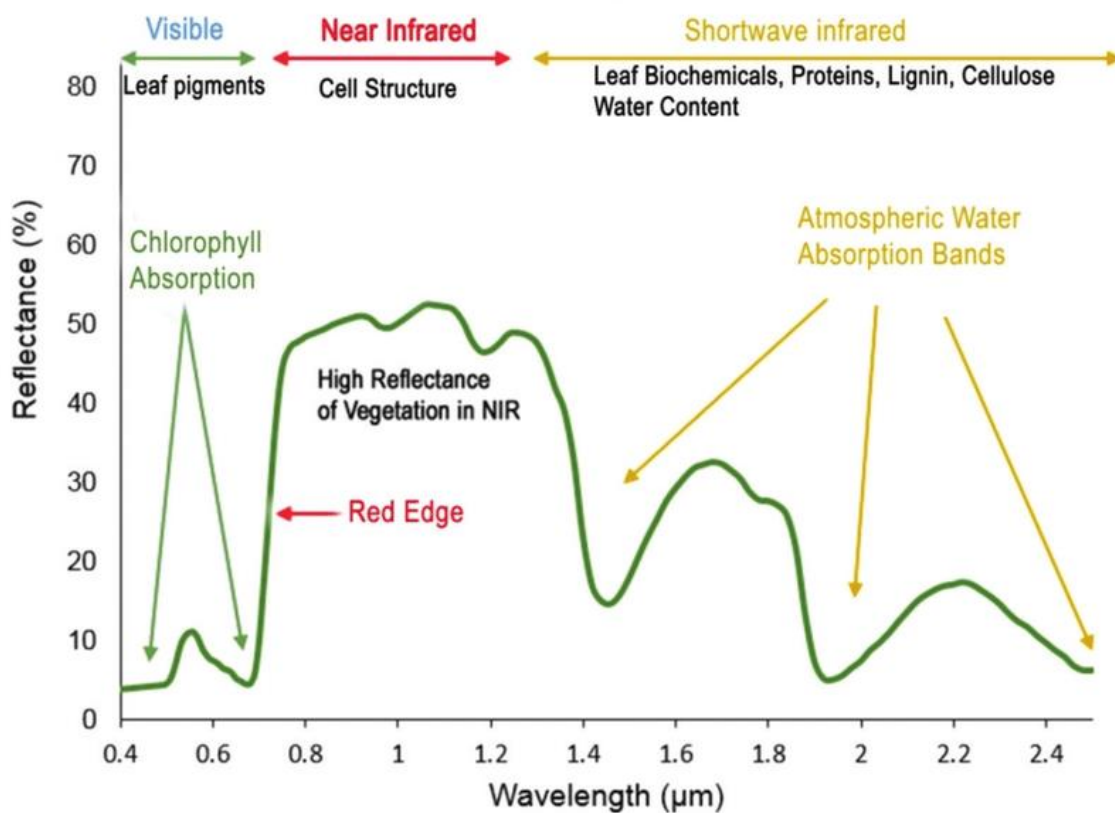


Figure 1-5 Typical vegetation reflectance spectrum (Roman & Ursu 2016)

Vegetation Indices (VIs) are combinations of surface reflectance at two or more wavelengths designed to highlight a particular property of vegetation. Figure 1-5 presents the typical vegetation reflectance spectrum. Vegetation Indices have been historically classified based on a range of attributes, including the number of spectral bands (2 or more than 2); the method of calculations (ratio or

orthogonal), depending on the required objective. Many of the indices make use of the inverse relationship between red and near-infrared reflectance associated with healthy green vegetation. The Normalized Difference Vegetation Index (NDVI) and Enhanced Vegetation Index (EVI) are the most popular and frequently-used VIs (Huete et al. 2002; Huete et al. 2008; Tucker 1979). Among a variety of VIs, EVI is an optimized combination of blue, red, NIR bands, designed to extract canopy greenness (Huete et al. 2002). Compared with NDVI, it is designed to enhance the vegetation signal with improved sensitivity in high biomass regions and improved vegetation monitoring through a decoupling of the canopy background signal and a reduction in atmosphere influences through introducing blue band as well as canopy background adjustment. The equation defining EVI is:

$$EVI = (1 + L) \times \frac{\rho_{NIR} - \rho_{red}}{\rho_{NIR} + C_1 \cdot \rho_{red} - C_2 \cdot \rho_{blue} + L} \quad (1)$$

where  $\rho_{NIR}$ ,  $\rho_{red}$ , and  $\rho_{blue}$  are reflectance of the near infrared, red, and blue bands respectively;  $L$  is the canopy background adjustment; and  $C_1$ ,  $C_2$  are the coefficients of the aerosol resistance term, which uses the blue band to correct for aerosol influences in the red band. (Huete et al. 2002). It is demonstrated that EVI is less sensitive to soil background and outperform over arid/semiarid heterogeneous landscape relative to NDVI (Hmimina et al. 2013; Huete et al. 2002; Wang, Beringer, et al. 2019).

Increasing studies using time-series VI profiles as a benchmark of how biophysical parameters shift connect with the environmental drivers (Ma et al. 2013; Ma et al. 2014). VIs (e.g. EVI, NDVI) are widely applied to assess the effects of extreme climate on ecosystem functioning and vegetation productivity at regional, continental, or global scale (Broich et al. 2018; Kath et al. 2019; Wang, Yang, et al. 2019; Xu et al. 2018). Dramatic impacts of climate extremes on vegetation dynamics (as measured by EVI) with abrupt changes in phenology and productivity over southeast Australia demonstrates that semiarid ecosystems exhibit the largest sensitivity to hydro-climatic variations (Ma et al. 2015).

### **1.3.2 Land surface phenology**

Vegetation phenology, the study of the periodic biological life cycle events of plants, is a critical regulator of carbon and water cycling in terrestrial ecosystems (Peng et al. 2018). The trend of global warming has aroused great interests in understanding and monitoring the dynamics of vegetation phenology under the changing climate (Piao et al. 2019). Phenological studies are usually conducted at the species- or ecosystem-level through ground-based field techniques (Ma et al. 2013), such as visual inspection, eddy covariance flux towers, near-surface spectral radiometer and digital cameras (Verger et al. 2016). During the past decades, remote sensing technique, providing the unique feasible way for examining broader scale phenomena with its synoptic

characteristics across large temporal and spatial scales (Ma et al. 2013), has notably expanded the horizon of traditional phenology observation (Piao et al. 2019). Distinguishing with conventional phenology definitions which refer to specific life cycle, land surface phenology (LSP) are observing patterns connected with biological phenomena at the landscape level from the regional to global scale (Friedl et al. 2006). As a valuable indicator of climate variability and ecosystem responses (Peng et al. 2018), accurate measurements of land LSP is crucial for better explicating the land-atmosphere-energy exchange and its representation in terrestrial biosphere models (Ma et al. 2013; Zhang, Kong, et al. 2018). Vegetation indices can depict spatiotemporal patterns of the timing of plant growth, senescence, and dormancy at seasonal and inter-annual time scales (Broich et al. 2018). The enhanced vegetation index (Huete et al. 2002), normalized difference vegetation index (Tucker 1979) , and leaf area index (LAI) derived from optical satellite sensors are widely applied for tracking large-scale vegetation seasonality.

Phenology metrics, including ‘green-up’ (start of growing season), ‘brown-down’ (end of growing season), peak period of the growing season, length of active growth season, are quantitative indicators of vegetation seasonality that are consistently application for spatial-temporal patterns (Hufkens et al. 2012). There are several approaches for deriving phenology metrics from VI profiles, and respectively are threshold-based, derivative-based, smoothing function-

based, and model fitting-based (De Beurs & Henebry 2005). Each method has its merits and drawbacks, and is suitable for different characteristics of landscapes or ecosystem. Broich et al. (2015) released the first Australian LSP products in 2013, named the Dataset Australian Land Surface Phenology Products (Version 1), which is a continental-specific synoptic dataset. This dataset enables the quantitative analysis of Australian LSP derived from the MODIS EVI satellite image data stream using a modelling algorithm designed to fit the high climatic and resulting high LSP variability of Australia.

LSP products have been applied for diverse ecosystems and ecoregions, however, there are still remaining many challenges and opportunities for improvement, for instance the problem of long-term continuity and cross-scale comparison. With the fast pace of technologies and learning from the past lessons, it is an urge to explore novel methods for LSP monitoring and to seek global application algorithms with suites of new-launched advanced satellites.

## **1.4 Solar-induced chlorophyll fluorescence (SIF)**

### **1.4.1 Photosynthesis and chlorophyll fluorescence**

Through photosynthesis by terrestrial ecosystems, gross primary production constitutes the largest global carbon sink. Photosynthesis, the process by which plants absorb solar radiation to generate sugar and oxygen from CO<sub>2</sub> and water, is the principal source of energy for most life on Earth (Guanter et al. 2014).

Sunlight absorbed by chlorophyll pigments is primarily used to drive

photosynthesis, and the remaining energy can be dissipated as heat or re-radiated at longer wavelengths (660–800 nm) (Yang et al. 2015), as shown in Figure 1-6. This near-infrared light re-emitted from plants is termed solar-induced chlorophyll fluorescence (SIF) (Yang et al. 2015). The fluorescence emission with two peaks is known as the red (near 685 nm) and far-red (near 740 nm) emission features (Yoshida et al., 2015). This phenomenon offers a novel way to estimate photosynthesis using fluorescence.

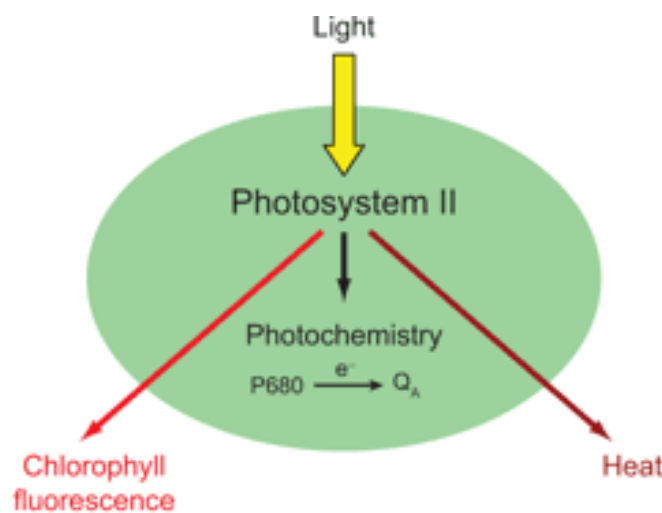


Figure 1-6 Schematic diagram of photosynthesis and chlorophyll fluorescence (Baker, 2008)

In the light use efficiency model, SIF can be expressed as,

$$SIF = f_{PAR} \times PAR \times LUE_f \times f_{esc} \quad (2)$$

where  $LUE_f$  is the light use efficiency for fluorescence and  $f_{esc}$  is the escape ratio of fluorescence at canopy scale;  $PAR$  refers to the photosynthetic active radiation (unit:  $W\ m^{-2}$ ) and  $f_{PAR}$  refers to the fraction of absorbed photosynthetic active radiation. SIF is usually given in radiance units ( $mW\ m^{-2}$ )

$\text{nm}^{-1} \text{sr}^{-1}$ ) and varies marginally with viewing geometry (Joiner et al. 2013).

Likewise, GPP can be simplified with the light use efficiency model,

$$GPP = f_{PAR} \times PAR \times LUE_p \quad (3)$$

where  $LUE_p$  is the light use efficiency for photosynthesis. If we eliminate  $PAR \times f_{PAR}$  and combine the equations (2, 3), we obtain

$$GPP \propto SIF \cdot \frac{LUE_p}{LUE_f} \quad (4)$$

Theoretically, there is a strong relationship between SIF-GPP. Fluorescence measurements directly from the core of photosynthetic machinery present a fresh manner of monitoring vegetation growth and response (Frankenberg et al. 2011; Guan et al. 2015; Sun et al. 2017). The incorporation of SIF can more accurately estimate GPP and further contribute to enhanced understanding of the role of drylands in driving interannual variability of global carbon cycle (Biederman et al. 2017).

#### **1.4.2 Remote sensing of SIF**

The instruments to measure SIF from spaceborne platforms (e.g., from the Japanese Greenhouse gases Observing SATellite, GOSAT; Global Ozone Monitoring Experiment-2, GOME-2; Orbiting Carbon Observatory-2, OCO-2; or TROPOspheric Monitoring Instrument, TROPOMI; The SCanning Imaging Absorption spectroMeter for Atmospheric CHartographY, SCIAMACHY)

present a means for assessing photosynthesis from satellite-based SIF (Table 1-1) (Yang et al. 2015). The spectrometer of GOSAT covering the 755-775 nm with spectral resolution of 0.025 nm (Frankenberg et al. 2011) therefore is able to extract SIF signal at the 757 and 770 nm of Fraunhofer line. GOME-2 onboard MetOp-A or MetOp-B launched by the European Space Agency are used to retrieve the SIF dataset with spatial resolution increased to 40 km×40 km (Joiner et al. 2016). Even though, the coarse spatial resolution of the aforementioned spaceborne SIF products impedes the full capacity for understanding the mechanistic SIF-photosynthesis relationship (Yu et al. 2019), as well as the application over heterogeneous ecosystems. More recently, OCO-2 and TROPOMI with substantially improved spatiotemporal resolution (OCO-2, 1.3 km ×2.25 km; TROPOMI, 7 km × 3.5 km) are already launched and benefit for assessing the relationship of SIF-GPP at ecologically meaningful scale (Köhler et al. 2018; Sun et al. 2017). Figure 1-7 presents the spatial comparison of SIF retrieved from TROPOMI, OCO-2, and GOME-2 (Köhler et al. 2018).

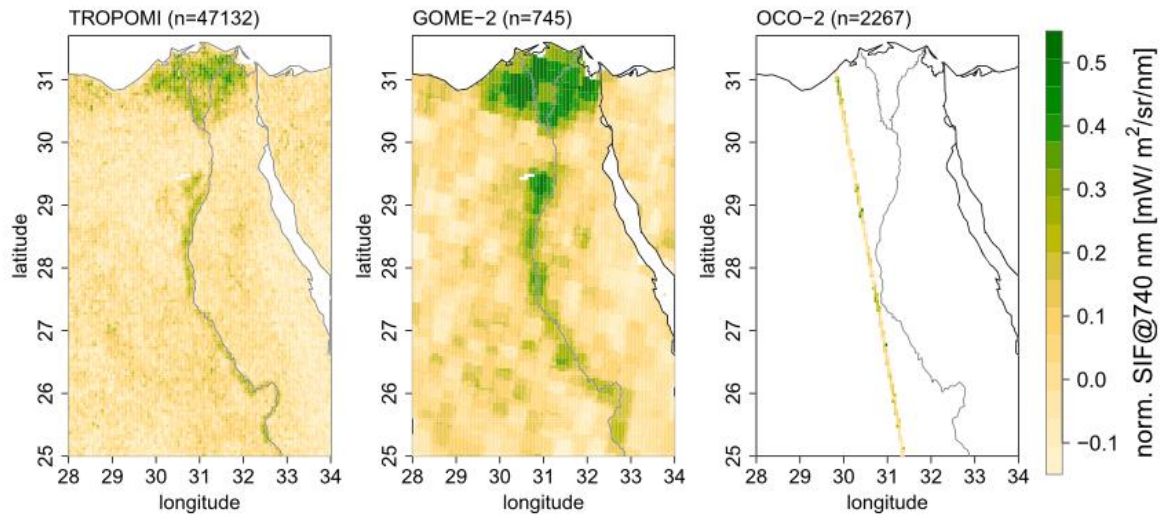


Figure 1-7 Spatial comparison between TROPOMI, GOME-2, and OCO-2 SIF in the Nile region based on data acquired between 23 and 29 November 2017 (Köhler et al. 2018)

Many studies found that satellite-based observations of SIF can detect interannual and seasonal variations in gross primary production of vegetation in North America (Yang et al. 2015; Zhang et al. 2016; Zuromski et al. 2018). Wu et al. (2018) found strong spatiotemporal consistency between satellite-based SIF and GPP products across the contiguous United States. Based on the eddy covariance flux sites in the vicinity of OCO-2 orbit, the SIF-GPP relationships are shown to be strong and more consistent among different vegetation types relative to results of previous studies (Sun et al., 2017).

Table 1-1 Summary of primary satellite-based instrument for SIF retrieval

Instrument	Operational	Footprint (Nadir)	Overpass time (local time)	Spectra (SIF retrieval)
GOME-2	2007-present	40km×40km*	9:30	734–758 nm
OCO-2	2014-present	1.29km×2.25km	13:30	757–775 nm
GOSAT-FTS	2009-present	10.5km in diameter	13:00	758–775 nm
TROPOMI	2017-present	7km×3.5 km	13:30	725–775 nm

\* The footprint of GOME-2 onboard MetOp-A is 80km×40km before 15 July 2013, and 40km×40km since 15 July 2013.

Although photosynthesis and greenness exhibit an analogous seasonality in deciduous forests, satellite chlorophyll fluorescence measurements reveal large-scale decoupling of photosynthesis and greenness dynamics in boreal evergreen forests (Chang et al. 2019; Walther et al. 2016). By comparing with EVI and photochemical reflectivity index, Smith et al. (2018) demonstrated that chlorophyll fluorescence more accurately captures seasonal and interannual variations of gross primary productivity across dryland ecosystems of southwestern North America. Through evaluating the SIF time series with tower-based GPP in Australia, Sanders et al. (2016) found natural biome types, such as savanna and open woodland, showed weaker correlations relative to managed biomes. Taking into account sparse sampling of spaceborne SIF signals as well as a structural continuum with varying mixtures in Australia's dryland ecosystem, a spatially contiguous SIF product was utilized to explore the phenology dynamics of dryland ecosystems along the North Australian Tropical Transect (Wang, Beringer, et al. 2019). They found this modelled SIF data outperformed EVI for characterizing seasonal onset and senescence of dryland vegetation, and suggested it had potential for large-scale mapping of phenology dynamics as opposed to traditional reflectance-based vegetation indices. Continuous observations of both SIF and vegetation indices contributes to the understanding of the differences between, and information carried by,

seasonal variations vegetation structure and greenness and physiology (Jeong et al. 2017).

### **1.5 Aims and objectives**

The overall goal of this thesis is to explore the spatiotemporal dynamics of dryland vegetation in Australia under climate extremes using multi-satellite observations as well as in-situ measurements. More specifically, I utilized a recent wet pulse (2016-2017) as a natural experiment to investigate two major dryland biomes (Mulga and Hummock) in response to the extreme wet events in the context of anomalous carbon uptake. Subsequently, I present an analysis of the impact of 2018-2019 extreme drought on greenness and fluorescence of Australia's dryland vegetation. Furthermore, I assessed the seasonal and interannual variability of biome-specific dryland vegetation along the North Australian Tropical Transect. The objectives and research questions of this thesis are described below, by chapter;

Chapter 1 provided an introduction to this thesis. It began by describing the broad context of climate change, climate extreme, as well as its impact on global carbon cycle. Then dryland ecosystems, including major arid/semiarid biomes in Australia was introduced, those play critical role in dominating interannual variability of global carbon sink. Moreover, I presented a comprehensive literature review with regard to satellite-based vegetation observation, such as reflectance-based vegetation indices and solar-induced

chlorophyll fluorescence. Lastly, I listed the aims and objectives of each research chapter of this thesis.

Chapter 2 investigates the response of satellite-observed SIF and EVI to 2010-2011 big wet as well as a recent extreme wet pulse in 2016-2017 over arid central Australia mainly covered by Hummock grasslands, Mulga woodlands/shrublands. I further examined relationship between satellite-observed soil moisture and vegetation variables that underlay the influences of two contrasting wet regimes. The specific objectives of Chapter 2 are to (1) characterize the spatial-temporal traces in greening and drying of arid and semi-arid Australia's dryland vegetation under extreme wet pulses; (2) investigate the extreme climate responses of major biome types (Hummock, Mulga) in terms of magnitude and rate; (3) examine the potential benefits of satellite-based SIF to monitor dryland ecosystem dynamics in central Australia.

Chapter 3 investigated the spatial and temporal responses of SIF and EVI of dryland vegetation to 2018-2019 extreme drought over Australia using multi-source satellite-based SIF observations. In addition, I examined the potential of SIF data retrieved from newly-launched TROPOMI over heterogeneous landscape. The specific objectives of Chapter 3 are to (1) assess the potential of spaceborne SIF for monitoring drought dynamics over water-limited ecosystems; (2) identify spatiotemporal patterns in the response of dryland vegetation to major drought at different severity and time scales; (3) contrast the

variability of fluorescence and greenness of dryland biomes under extreme drought.

Chapter 4 explored the seasonal and interannual variability of biome-specific dryland vegetation using satellite-observed SIF and EVI along the North Australian Tropical Transect. Specifically, I aim to: (1) evaluate the spatial patterns and seasonal variations of dryland vegetation phenology derived from SIF and EVI; (2) determine the phenology dynamics of major plant function types, C3-dominated woodlands/shrublands (Mulga, Eucalypt) and C4-dominated grasslands (Hummock, Tussock); (3) assess the interaction of environmental drivers and vegetation function types on photosynthetic dynamics.

Chapter 5 summarises all of the findings, highlighted significant results, and drew conclusions from each research chapter (Chapters 2-4) within the broader context. The limitations of this research and directions for future related studies are also discussed in this chapter.

## **Chapter 2 Response of Dryland Vegetation under Extreme Wet Events with Satellite Measures of Greenness, Fluorescence**

### **Abstract**

An exceptionally 'big wet' event occurred in central Australia during 2010-2011, triggering a huge vegetation response that was largely responsible to a large global land carbon sink anomaly. This was repeated with another extreme wet pulse during 2016-2017 monsoon season in central Australia. While the impact of big wet on terrestrial carbon budget has been well recognized, it remains unclear to what extent these extreme events could alter greenness and photosynthesis of biome-specific dryland vegetation in the context of anomalous carbon uptake. We therefore investigated responses of major biomes (Mulga woodland/shrubland and Hummock grassland) to these two wet pulses, utilising multi-satellite observations of (1) solar-induced chlorophyll fluorescence (SIF) as a proxy for photosynthetic activity, (2) enhanced vegetation index (EVI) as a measure of surface chlorophyll or greenness, as well as in-situ flux measurement. Considering that soil water content is an excellent predictor of plant growth over water-limited ecosystem, we further examined relationship between satellite-observed soil moisture and vegetation variables that underlay the influences of two contrasting wet regimes. The results showed EVI with markedly amplified seasonal amplitude was considerably responsive to both extreme wet events. Due to weak

responsiveness of Hummock grassland in 2016-2017 wet pulse, enhancement of SIF was notably slighter than that in 2010-2011. Mulga woodland was invariably most responsive among major biomes, ascribed to its strong sensitivity to soil moisture availability. Despite a robust linear SIF-Gross Primary Production (GPP) relationship at site level, spatially coarse SIF derived from the Global Ozone Monitoring Experiment-2 (GOME-2) has imperfect capacity for capturing spatiotemporal dynamics over xeric central Australia. Our study implies that satellite observations of greenness and fluorescence potentially offer an improved understanding of dryland vegetation dynamics and can advance our ability to detect ecosystem alterations under future changing climates.

## **Keywords**

Wet Pulse, EVI, SIF, Mulga woodland/shrubland, Hummock grassland

## **2.1 Introduction**

Drylands (arid, semiarid, and subhumid), covering approximately 41% of global land surface (Reynolds et al. 2007), play a critical role in regulating the climate system and predominantly drive the trend and interannual variability in the global land carbon uptake over the last three decades (Ahlström et al. 2015; Haverd, Smith & Trudinger 2016; Li et al. 2017; Poulter et al. 2014). Recent studies report a massive global land carbon sink anomaly in 2010-2011 was driven by growth in semiarid vegetation of the south hemisphere, with almost

60% occurring in Australia as a consequence of the record-breaking rains (Detmers et al. 2015; Ma et al. 2016; Rammig & Mahecha 2015). As prolonged drought and severe wet events are projected to increase both frequently and intensely (Huang et al. 2016; Min et al. 2011) that exacerbate profound impacts on water resources, ecosystems, economy and society (Evans, Meng & McCabe 2017), it is essential to enhance understanding of dryland ecosystem functioning under future changing climate.

Australia is the driest inhabited continent worldwide, of which 70% are encompassed with arid or semiarid ecosystems across the vast interior and dominated by three major biomes along a woodland-savanna-grassland continuum (Bowman, Boggs & Prior 2008; Cleverly et al. 2013; Cleverly, Eamus, Van Gorsel, et al. 2016; Xie et al. 2016). Among them, hummock grasslands (*Triodia* spp.), mulga woodlands (*Acacia aneura*), and mulga shrublands varied in photosynthetic pathway ( $C_4$  grass,  $C_3$  tree respectively), are widely distributed and juxtaposed in xeric zone of central Australia (Cleverly, Eamus, Van Gorsel, et al. 2016; Eamus et al. 2013). Relative to mesic northern vegetation, these semiarid biomes show the largest temporal variability in phenology, and exhibit much greater overall responsiveness to hydro-climatic variability (Ma et al. 2013).

Quantifying response of vegetation to extreme hydro-climatic events is crucial for effectively managing environment and global change research (Broich et al.

2018), and usually utilised observation-based methods, such as field measurement, airborne and spaceborne observation (Yang et al. 2018). With particular emphasis on eddy covariance data of landscape fluxes of CO<sub>2</sub>, Eamus et al. (2016) demonstrated that Mulga contributed markedly to the large 2011 anomaly in terrestrial carbon uptake. The following drought in 2011-2012 promptly diminished the massive net carbon uptake over central Australia (Ma et al. 2016), of which Corymbia savanna interspersed with Hummock grass was a very large net carbon source in contrast to the extreme drought tolerance of Mulga as approximately carbon neutral (Cleverly, Eamus, Van Gorsel, et al. 2016).

Satellite remote sensing offers a new perspective to monitor vegetation status at regional, continental or global scale (Huete et al. 2008), especially valuable for the remoteness of most Australia's interior with sparse monitoring site. Through normalized difference vegetation index (NDVI) as vegetation productivity proxies derived from satellite time series data, Ratzmann et al. (2016) investigated functional response of dryland vegetation to altered rainfall patterns over semiarid regions in Africa and indicated that higher interannual rainfall variability might favour a more dynamic vegetation response. Likewise, Broich et al. (2018) found substantial differences in timing, magnitude and duration of vegetation responses and its dependence on rainfall and flooding during a period of extreme hydro-climatic variability over semiarid area across

Australia's Murray Darling Basin. Dramatic impacts of climate extremes on vegetation dynamics (as measured by EVI) with abrupt changes in phenology and productivity over southeast Australia also demonstrates that semiarid ecosystems exhibit the largest sensitivity to hydro-climatic variations (Ma et al. 2015).

In contrast to traditional vegetation indices, satellite retrievals of SIF based on energy reemitted by plants rather than reflected present a fresh manner to observe vegetation growth and response (Frankenberg et al. 2011; Guan et al. 2015; Sun et al. 2017). SIF appears to better capture interannual variations in GPP across dryland ecosystems of southwestern North America (Smith et al. 2018). The incorporation of SIF can more accurately estimate GPP and further contribute to enhanced understanding of the role of drylands in driving interannual variability of global carbon cycle (Biederman et al. 2017).

Moreover, previous studies reveal that spaceborne SIF has excellent potential to early detect drought-related and heat stress condition across a variety of ecosystems, such as cropland, grassland and forest (Song et al. 2018; Sun et al. 2015; Yang et al. 2018; Yoshida et al. 2015). Nevertheless, considering spatially coarse satellite-based SIF products, studies with reference to the application of SIF over heterogeneous dryland or savanna under extreme wet events thus far remain unknown.

Numerous studies manifest that vegetation phenology and productivity in arid ecosystem are largely controlled by soil water content (Cleverly, Eamus, Restrepo Coupe, et al. 2016; Madani et al. 2017), accordingly it can be used as an outstanding predictor for plants growth under changing climates. Chen et al. (2014) illustrates that satellite derived soil moisture is markedly correlated with NDVI in most areas of Australia continent with a typical time scale of NDVI lagging by one month, and implies that the influence of soil water availability on vegetation at varied temporal scales. More importantly, the integration of synchronous large-scale satellite-based observations of soil moisture and SIF conduces significantly to advances in the predictive understanding of global terrestrial coupled carbon-water cycles (Qiu et al. 2018).

The aims of this study were to evaluate varying responses of major biomes to extreme wet events in terms of greenness and photosynthesis and to provide new insights of the potential of spaceborne SIF over xeric interior of Australia. Specifically, we address three scientific questions: (1) how are the temporal and spatial variations of SIF and EVI related to those of hydro-climatic drivers under extreme wet pulses? (2) how do C<sub>3</sub>-dominated woodland (Mulga) and C<sub>4</sub>-dominated grassland (Hummock) differ in magnitude and rate of responses? (3) can SIF accurately track the dynamics of wet-induced carbon sink, following tower-based GPP?

## 2.2 Materials and Methods

### 2.2.1 Study region

This study was conducted at a sub-continental scale over central Australia, encompassing an area of nearly 2.7 million km<sup>2</sup> between 18°S to 30°S and 120°E to 140°E (Figure 2-1). This vast area has a Mean Annual Precipitation (MAP) ranging from 200 mm to 600 mm according to a 30-year (1981-2010) average annual rainfall (Australian Bureau of Meteorology, <https://www.bom.gov.au>), is comprised by majority of dominant vegetation types, such as Hummock grassland, Mulga woodland, Mulga shrubland, Eucalypt woodland and Tussock grassland, covering 43.5%, 11.6%, 16.2% 7.7%, and 6.6% respectively. We note that categories of Acacia open woodlands and Acacia Forests and woodlands were reclassified as *Mulga woodlands*. The remaining woody (Casuarina, Melaleuca forests and woodlands, Mallee woodlands), shrub (Heathlands, Chenopod, Samphire shrublands, Forblands) and grass groups were sorted as *Other Woodlands*, *Other Shrublands*, and *Other Grasslands* separately (Figure 1, Data source: National Vegetation Information System (NVIS), Major Vegetation Groups (MVGs), Version 5.1, <https://www.environment.gov.au/>).

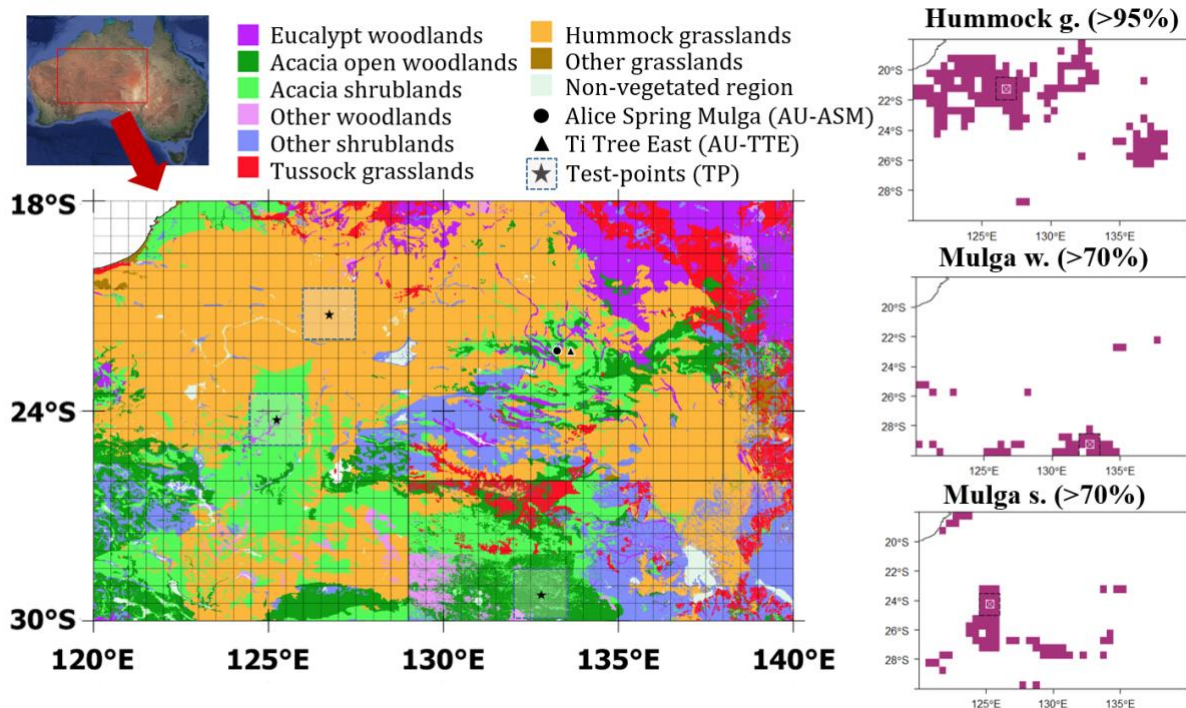


Figure 2-1 Map of reclassified major vegetation groups over central Australia (map source: NVIS Version 5.0). Black dot and triangle represent AU-ASM, AU-TTE flux tower sites respectively; Black pentagrams refer to the three selected test-points as well as the extent of 3×3 pixels labelled as blue dashed square; Grids refer to a fishnet at 0.5° spatial resolution, consistent with pixel size of GOME-2 SIF data. Top-left figure displays the locations of the study area over Australian continent (image source: Google Earth). Left column shows the spatial distributions of relative homogenous pixels of three major biomes at a 0.5° resolution. (g. refers to grassland, w. refers to woodland, s. refers to shrubland, selection percentages are listed in parentheses).

Two eddy covariance tower sites within this extent, respectively are Alice

Spring Mulga (AU-ASM, [22.28°S 133.25°E]) and Ti Tree East (AU-TTE,

[22.28°S 133.64°E]) separated by approximately 40 km

(<http://www.ozflux.org.au/>). The AU-ASM is located in a high-dense Mulga

woodland but with sparse canopy, in contrast to the AU-TTE in a *Corymbia*

savanna containing scattered trees above a matrix of Hummock grass (Cleverly,

Eamus, Restrepo Coupe, et al. 2016; Cleverly, Eamus, Van Gorsel, et al. 2016).

Detailed description of two sites with reference to floristics, soil and landscape

can be found in Eamus et al. (2016) and Cleverly, Eamus, Van Gorsel, et al. (2016).

To examine variation in response to extreme wet events across vegetation types along with biome-specific vegetation-moisture relationship, we only selected three “pure” test-pixels because those were all that could be identified at the coarse 0.5° spatial resolution of the SIF data, especially for Mugla woodland, Mulga shrubland (as shown in Figure 2-1). Pixels selection criteria: (1) given there was more Hummock grassland, pixels with coverage percent of Hummock grassland above 95%, Mulga woodland & Mulga shrubland above 70% based on NVIS MVGs were chosen; (2) As satellite variables were averaged within 3×3 (pixels) window centered at TP, pixels within the extent of 1.5°×1.5° around the test-points needs to be covered by coherent vegetation type. We only selected three “pure” test-pixels because those was all that could be identified at the coarse 0.5° spatial resolution of the SIF data, especially for Mugla woodland, Mulga shrubland (as shown in Figure 2-1). The selected TPs were respectively TP-Hummock grassland [21.25°S 126.75°E], TP-Mulga woodland [29.25°S 132.75°E], and TP-Mulga shrubland [24.25°S 125.25°E].

### **2.2.2 Satellite Data**

EVI is an optimized version of vegetation index that effectively reduces soil background influences and is widely used as a proxy of canopy greenness (Huete et al. 2002). We used 11-years (2007-2017) of the Moderate Resolution

Imaging Spectroradiometer (MODIS, Collection 6) MYD13Q1 (250 m, 16-day, tile: H30V11) and MYD13C2 EVI data set with climate modelling grid (0.05°, monthly) downloaded from NASA Earth Observation data (<https://search.earthdata.nasa.gov/search>). To reduce noise and uncertainties, only best quality data was remained in this study through removing pixels of which quality control flag of the first 2 bits neither 00 nor 01. The 16-day EVI with finer spatial resolution (MYD13Q1) were aggregated into monthly data by temporal averaging to conform with other satellite-based dataset. The algorithm operates on a per-pixel basis and requires multiple observations (days, or pre-composited as in collection 6) to generate a composited EVI value that will represent the full period. On account of orbit overlap, multiple observations from the same date occur in same pixel. The objective of the compositing method is to extract a single value of each pixel from all the retained filtered data, which refer to the pixel for the specific 16-day period.

Spaceborne SIF data in this study were retrieved from GOME-2 onboard the European Organisation for the Exploitation of Meteorological Satellites (EUMETSAT) Meteorological Operational Satellites. The GOME-2 instrument is a nadir-scanning spectrometer, which measures at around 9:30 local equator crossing time, and it has a relatively large footprint (approximately 40 km x 80 km at nadir, before 15 July 2013, and 40 km x 40 km since 15 July 2013). GOME-2 comprises four main optical channels with the spectral range from

240 to 790 nm, and the fourth channel ranges between 590 and 790 nm with a spectral resolution of approximately 0.5 nm and a relatively high signal-to-noise ratio (Joiner et al., 2013; Song et al., 2018a). This dataset is primarily retrieved from the filling-in of solar Fraunhofer lines in the vicinity of the 740 nm far-red fluorescence emission peak, based on a simplified radiative transfer model in the company of a principal component analysis in order to disentangle the fluorescence signals from atmospheric absorption and surface reflectance (Joiner et al. 2013; Köhler, Guanter & Joiner 2015). GOME-2 SIF records substantially enhanced sampling and precision relative to the filling-in signal at 758 nm from Japanese Greenhouse gases Observing SATellite (GOSAT) TANSO-FTS instrument (Joiner et al., 2013). Approximately 11 years (February 2007 to December 2017) of monthly SIF data at a spatial resolution of 0.5° (level 3, version 28) was obtained from National Aeronautics and Space Administration (NASA) Goddard Space Flight Centre (<https://avdc.gsfc.nasa.gov/>). Although various filtering are applied (Joiner et al., 2013), Level-3 data are monthly gridded averages, yet there still exists negative value due to imperfect bias correction, noise. Negative SIF values were treated as zero for further analysis (Joiner et al. 2013).

The monthly Soil Moisture (SM) at 0.25° spatial resolution was downloaded from the European Space Agency (ESA) Climate Change Initiative (CCI, version 4.4) data portal (<http://www.esa-soilmoisturecci.org>) (Dorigo et al.,

2017; Gruber et al., 2017; Liu et al., 2011, 2012; Wagner et al., 2012). Derived from several microwave sensors (e.g. Soil Moisture Active Passive, Soil Moisture and Ocean Salinity, the Global Precipitation Measurement Microwave Imager instrument, and the Tropical Rainfall Measuring Mission's Microwave Imager), the ESA CCI dataset merging active microwave with passive microwave soil moisture products through harmonization approach represents surface soil moisture (Chen et al. 2014). Satellite-based precipitation dataset from Tropical Rainfall Measuring Mission (TRMM) Multi-satellite Precipitation Analysis (TMPA) mission were utilised with monthly 0.25° resolution (3B43, Level 3, version 7) downloaded from NASA Precipitation Processing System (<https://pps.gsfc.nasa.gov/>).

### **2.2.3 Eddy covariance data**

The original Level 5 (AU-TTE, ranging from 2012-2017) and Level 6 data (AU-ASM, ranging from 2010-2017) provided by the OzFlux network (<http://www.ozflux.org.au/>) were used to pre-process, including quality control assessment, removal of outliers, and gap-filling (Cleverly et al. 2013). Flux partitioning for Level 5 data was conducted in open source R scientific computation environment (Version 3.5.1) associated with REddyProc package (Version 1.2). The half hour flux data were aggregated into monthly GPP to match with satellite-based observations.

## 2.2.4 Wet intensity classification

Owing to strong seasonality of rainfall (wet season: November-April), monthly anomalies of precipitation were calculated as a deviation from their corresponding multiyear (2007-2017) mean of each month. We used the hydrological year from July to end of June on account of study region located in the South Hemisphere. Two extreme wet periods were analyzed: (a) from February to March of 2010-2011, and (b) from December to January of 2016-2017. Cumulative Precipitation Anomalies (CPA) representing the accumulated amount of precipitation increment during the periods of wet pulse were computed for each grid cell respectively. Wet intensity defined by CPA were classified as five categories including *Extreme wet*, *Severe wet*, *Intense wet*, *Moderate wet*, and *Dry* (Table 2-1).

Table 2-1 Summary of wet pulse intensity classification

<b>Cumulative Precipitation anomaly (mm)</b>	<b>Intensity</b>	<b>Wet level</b>
CPA > 300	Extreme wet	<b>4</b>
$300 \geq \text{CPA} > 200$	Severe wet	<b>3</b>
$200 \geq \text{CPA} > 100$	Intense wet	<b>2</b>
$100 \geq \text{CPA} > 0$	Moderate wet	<b>1</b>
$0 \geq \text{CPA}$	Dry	<b>0</b>

### 2.2.5 Statistics

With the purpose of wet-related signals detection, monthly anomalies of vegetation variable ( $X_A$ ) were calculated as a deviation from their corresponding multiyear (2007-2017) mean of each month. To further account for spatiotemporal variability leading to diverse influence on vegetation response (Vicente-Serrano et al. 2013), we applied standardized anomalies ( $X_{SA}$ ) of all the aforementioned variables over each grid cell for further examining the moisture-vegetation relationship across space and time. The equation is:

$$X_{SA} = \frac{X_{ij} - \bar{X}_j}{\sigma_j} \quad (5)$$

where  $i$  is the yearly temporal coverage from 2007 to 2017,  $X_{ij}$  is the monthly ranging from July to June,  $\bar{X}_j$  and  $\sigma_j$  are the mean and standard deviation of time series  $x$  at month  $j$ .

We assessed the relationship between hydro-meteorological and vegetation variables over three TPs at annual and monthly scale respectively through calculating coefficient of determination ( $r^2$ ) as well as linear regression slope ( $k$ ) by a least square fit, representing the strength of relationship and the sensitivity of vegetation to moisture availability respectively. A  $t$  test was utilized to examine the statistical significant level of the relationships ( $p$ -value). To quantify temporal response of vegetation to water availability along with comparison of SIF-EVI per each biome, pixel-wise maximum Pearson's

correlation coefficient ( $r_{max}$ ) between SM and SIF, as well as SM and EVI within finite time lags analysis was examined by shifting vegetation variables one month forward at a time across a domain.

From a perspective of validation of satellite observations as well as comparison of effective indicators for quantifying dryland ecosystem dynamics, we evaluated the correlations of tower-based GPP and satellite-based SIF, EVI using coefficient of determination ( $r^2$ ) and linear regression slope ( $k$ ) during wet years (2010-2011, 2016-2017) and normal year mean (2012-2016) separately. Given a huge mismatch between footprint of flux tower and satellite observation, especially for spatially coarse SIF, we reviewed the correspondence ( $r^2$ ) between multi-year series of GPP and EVI during 2010-2017 at a variety of satellite-observed footprints increasing from 0.25 km to ~450 km, along with relationship between multi-year series of EVI and SIF, GPP and SIF.

## **2.3 Results**

### **2.3.1 Wet Pulse Characteristics in 2010-2011 and 2016-2017**

Spatially averaged seasonal variation in precipitation, SM, EVI, SIF during wet pulse years (2010-2011, 2016-2017) and climatology (non-wet years mean) are shown in Figure 2-2. It was found that both wet pulses sustained two months occurring respectively in early autumn of 2010-2011(Feb-Mar) and in hot summer of 2016-2017 (Dec-Jan) when rainfall was over approximately 3 times

SD (standard deviation) larger than non-wet year mean (Figure 2-2a). Soil moisture exhibited resembling temporal trajectories, almost reaching the peak simultaneously in conjunction with precipitation, however it maintained above the climatology (more than 1 SD larger) after extreme wet period, especially in 2010-2011 (Figure 2-2b). The seasonal amplitude of EVI in both wet years were enhanced pronouncedly relative to multi-year mean, particularly during the extreme wet periods as well as post-wet phase (Figure 2-2c). Correspondingly, SIF exhibited markedly enlarged seasonal patterns in both wet years compared with climatology, especially the maximum in 2010-2011 exceeding 2 SD larger than the peak of 2016-2017 (Figure 2-2d). Throughout post-wet period of both wet years, SIF declined sharply after climaxing in comparison to gradual decrease of EVI.

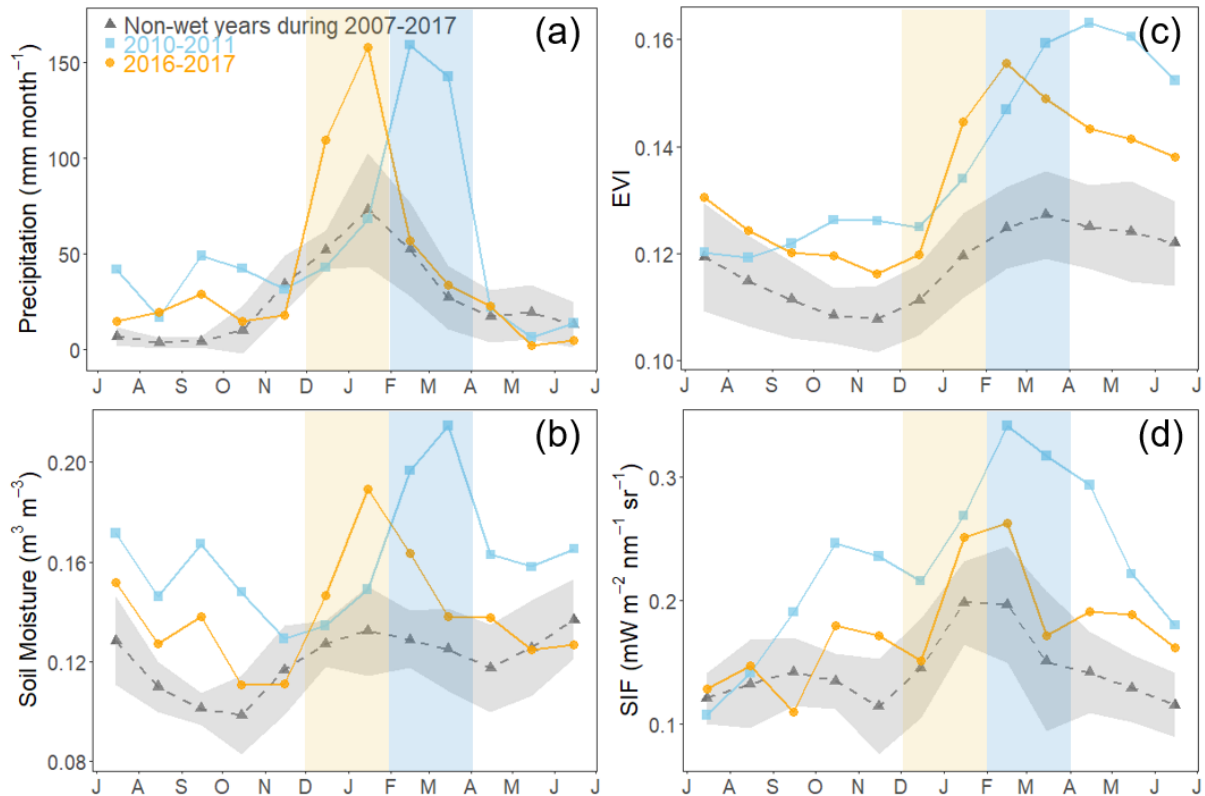


Figure 2-2 The region-wide mean seasonal cycle of (a) precipitation, (b) soil moisture, (c) EVI, and (d) SIF over study area during 2010-2011, 2016-2017 and non-wet years. The shaded area represent  $\pm 1$  standard deviation ( $\sigma$ ). The vertical rectangles refer to extreme wet periods of 2010-2011 (yellow) and 2016-2017 (blue) respectively.

Spatiotemporal distributions of standardized anomalies of precipitation, Soil

moisture, SIF, and EVI during 2010-2011 (Figure 2-3) and 2016-2017 (Figure 2-4) wet pulse as well as following three months are presented, respectively.

Across roughly whole study region (over 95%), rainfall and soil moisture with predominantly positive anomalies ( $SA > 0$ ) exhibited congruent spatial patterns during extreme wet period from February to March of 2010-2011 (Figure 2-3a, 2-3b). Afterwards, two hydro-meteorological variables varied at the post-wet stage in which SM within the majority of area (over 93%) remained positive anomalies in contrast to over half region of precipitation dropping below

average ( $SA < 0$ ). Overall,  $SIF_{SA}$  and  $EVI_{SA}$  tended to be spatially consistent with  $SM_{SA}$ , where both vegetation variables within the majority of domain (82% for  $SIF_{SA}$  and 96% for  $EVI_{SA}$ ) were larger than average (Figure 2-3c, 2-3d). In particular, EVI within 75.3% of study area maintained considerably positive anomalies ( $SA > 1$ ) since March 2011, however, the percentages of  $SIF_{SA}$  above 1 reduced from 48.5% to 29.4%.

On the other side, precipitation and SM in 2016-2017 wet pulse (Dec-Jan) were also larger than average ( $SA > 0$ ) across most region (~90% for  $Precipitation_{SA}$  and ~98% for  $SM_{SA}$ , shown in Figure 2-4a, 2-4b), however not as significant as those in 2010-2011 wet pulse. The percentages ( $SA > 2$ ) in 2010-2011 was over 40% for both hydro-meteorological variables relative to 32.3% for  $Precip_{SA}$  and 18.1% for  $SM_{SA}$  in 2016-2017 wet pulse. EVI displayed positive anomalies over most region (95.8%) since January 2017 (Figure 2-4d), while  $SIF_{SA}$  exhibited controversially spatial pattern of which over nearly half region (44.7%) was below than average ( $SA < 0$ ) throughout 2016-2017 wet pulse as well as following three months (Figure 2-4c). Besides, SIF with less than 23% region was significantly positive ( $SIF_{SA} > 1$ ) as compared to 73.9% of EVI ( $EVI_{SA} > 1$ ).

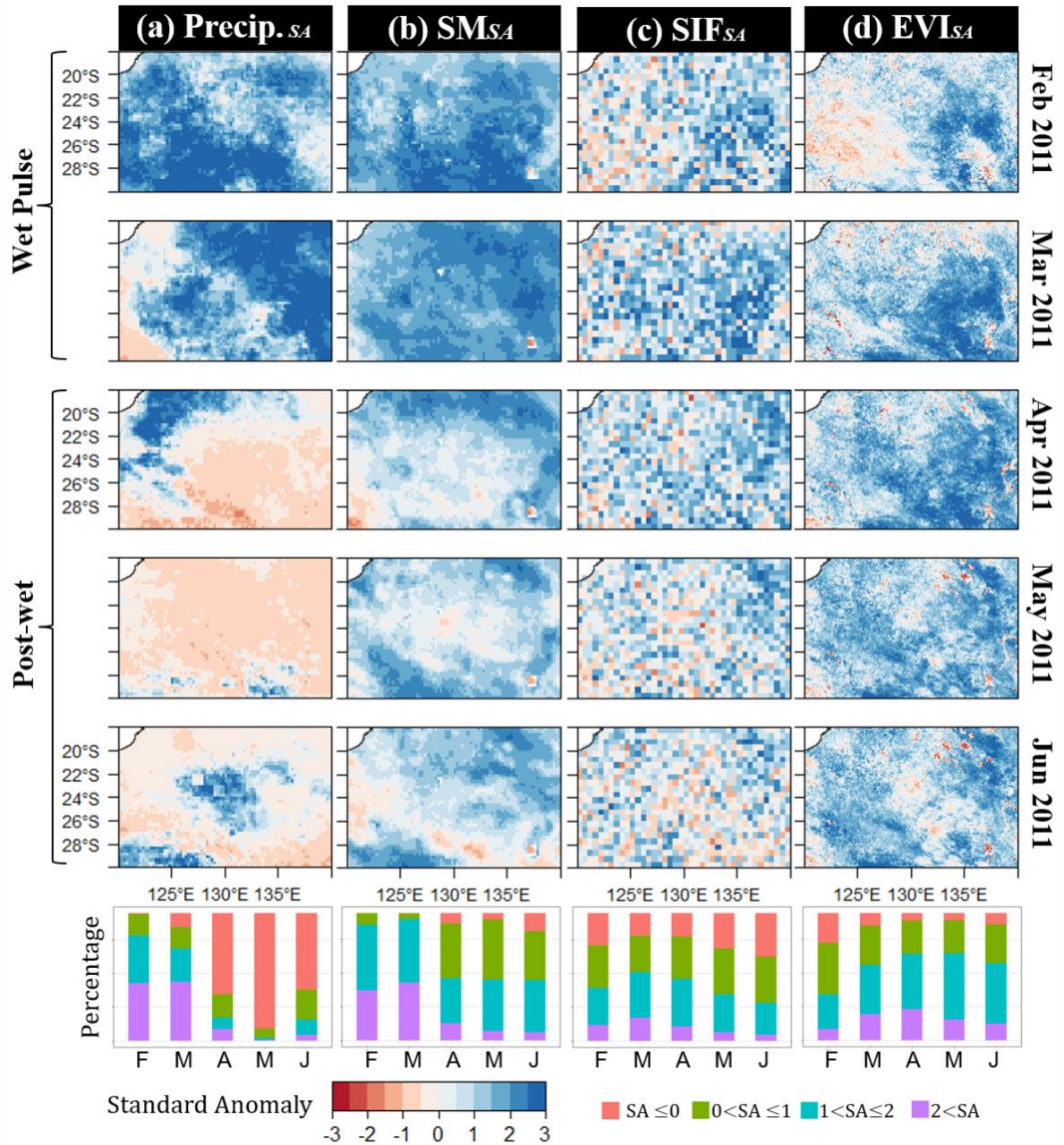


Figure 2-3 Spatial patterns of standard anomalies of (a) precipitation, (b) SM, (c) SIF, and (d) EVI during 2010-2011 wet pulse as well as following three months. Bottom panel shows frequency map of each SA (standard anomaly) category of the corresponding variable during the five months.

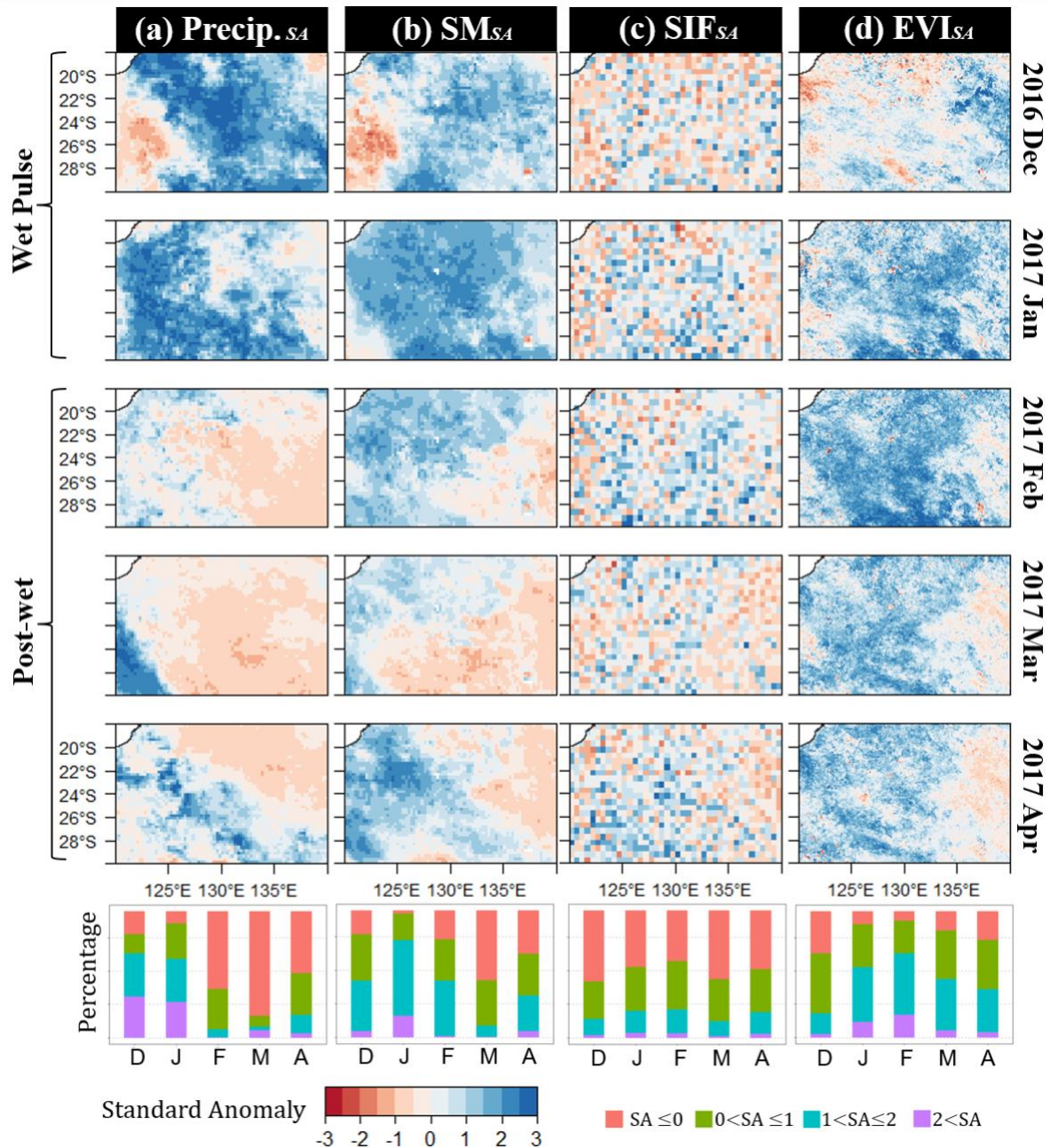


Figure 2-4 Spatial patterns of standard anomalies of (a) precipitation, (b) SM, (c) SIF, and (d) EVI during 2016-2017 wet pulse as well as following three months.

Region-wide map of wet intensity during 2010-2011 and 2016-2017 wet pulses were generated by cumulative precipitation anomalies (Figure 2-5a, 2-5b). The wet pulse of 2010-2011 wherein the majority of region experienced intense rainfall anomalies (Wet level  $\geq 2$ ) was apparently a more intense event relative

to that of 2016-2017. Additionally, extreme rainfall anomalies (Wet level  $\geq 3$ ) mainly occurred in the northeast as well as a patch of southwest in the first wet pulse (2010-2011), relative to the northwest between 121°E-127°E and 19°S-23°S in the later wet event (2016-2017). The percentages of each wet level in both wet pulses are illustrated along with three dominant vegetation types (Figure 2-5c, 2-5d). Only 17.1% of major biomes in 2016-2017 underwent severe or extreme wet situation (Wet level  $\geq 3$ ), mainly occurring over Hummock grasslands, in comparison to 36% of those in 2010-2011, comprising 11.3% of Mulga woodlands and Mulga shrublands.

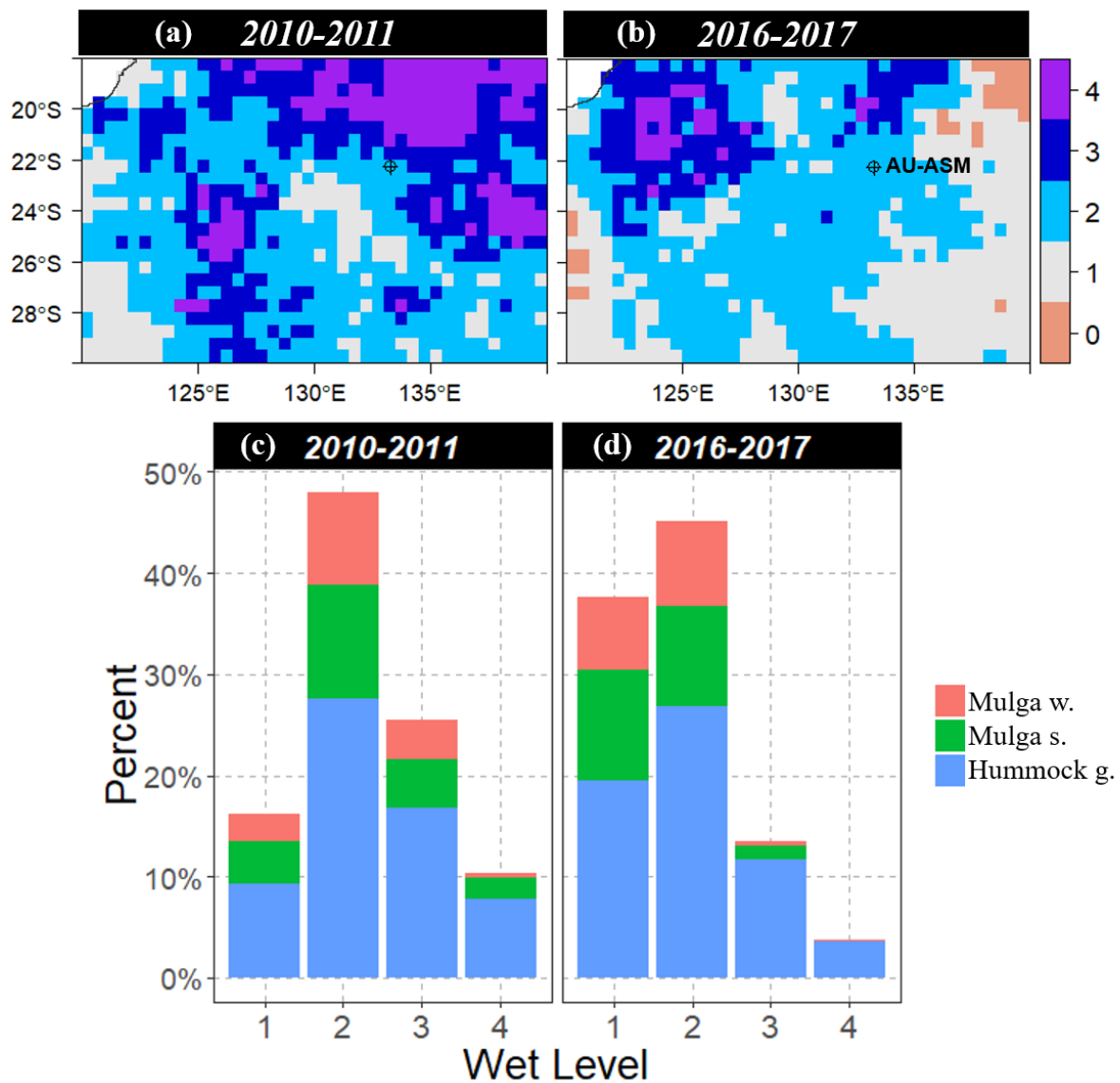


Figure 2-5 Spatial characteristics of wet pulses. (a, b) Spatial pattern of wet intensity during 2010-2011 and 2016-2017 wet pulses; (c, d) percentages of each wet level over three major vegetation types.

### 2.3.2 Response of vegetation per major vegetation type

Seasonal profiles of  $EVI_A$  and  $SIF_A$  of three major biomes averaged by wet intensity (Wet level from 1 to 4) in 2010-2011 and 2016-2017 are depicted (Figure 2-6). The magnitude of  $EVI_A$  and  $SIF_A$  of Mulga woodlands were remarkably enlarged along with increasing wet intensity (Figure 2-6c, 2-6d, 2-

6i, 2-6j), and both vegetation indicators of that in 2010-2011 showed largest positive anomalies in severe wet (Wet level = 3) among all categories (Figure 2-6c, 2-6d). Contrarily, the enhancement of  $SIF_A$  and  $EVI_A$  of Hummock grasslands and Mulga shrublands was generally constant regardless of severe or extreme wet (Wet level  $\geq 3$ ) in both wet pulses. Whilst 2016-2017 wet pulse,  $SIF$  of Hummock grasslands was continuously close to the average ( $SIF_A \sim 0$ ) even under extremely wet situation (Wet level  $\geq 3$ , Figure 2-6h). Likewise, the later wet event (2016-2017) raised marginally the amplitude of  $EVI_A$  of Hummock grasslands (Figure 2-6g). In addition,  $EVI_A$  of all major biomes sustained positive values and decreased gradually after extreme wet periods of both wet events, in comparison to the rapid decline of  $SIF_A$  as a result of decrease in photosynthetic activity resulting from reducing soil water availability arise promptly through stomatal closure.

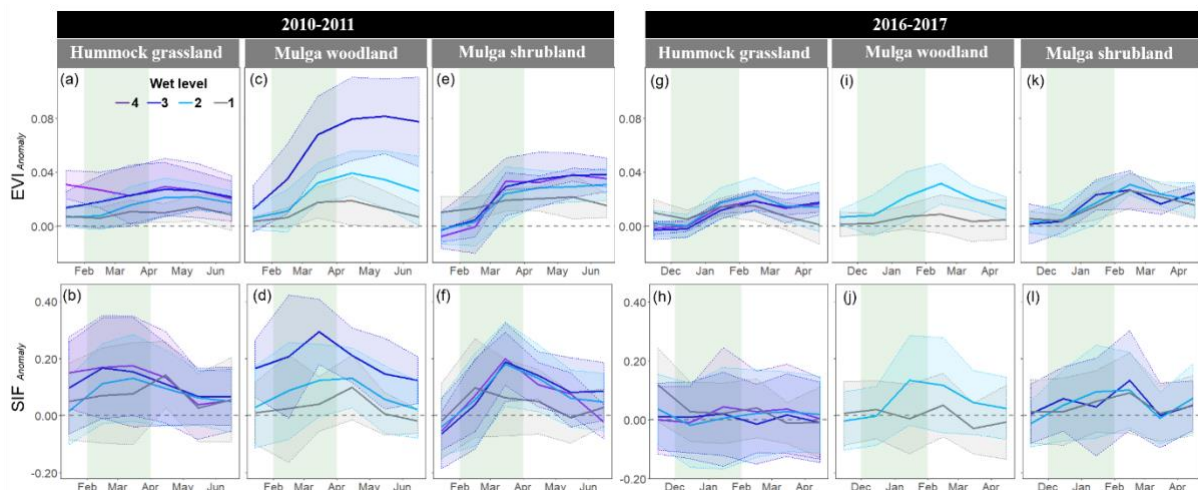
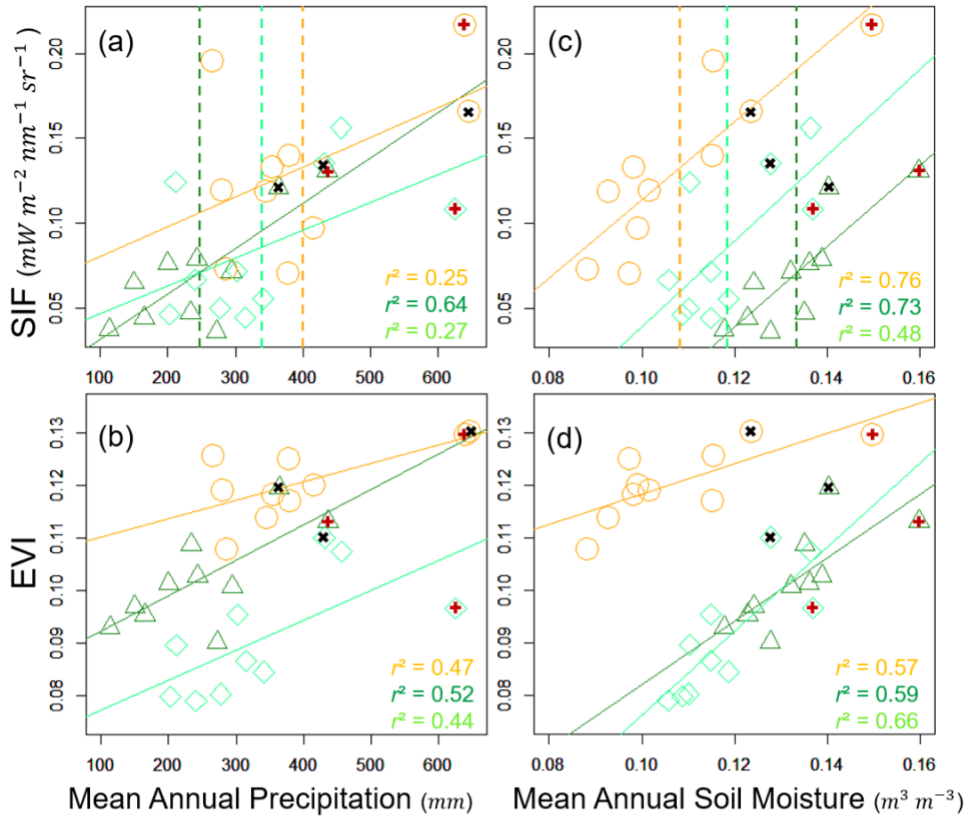


Figure 2-6 Seasonal variation in spatial averaged anomalies of EVI and SIF of major biomes by each wet level in 2010-2011 (a-f) and 2016-2017 (g-l). Colorful areas represent  $\pm 1$  standard deviation of the corresponding wet level. The vertical rectangles refer to extreme wet periods (2-month).

To further investigate the relationship between moisture condition and vegetation function, scatter plots between annual mean of precipitation, SM, SIF, EVI over three selected sites are depicted (Figure 2-7a~7d). Both SIF and EVI of all three TPs were more tightly correlated with soil moisture ( $r^2$  ranging from 0.48 to 0.76) than precipitation ( $r^2$  ranging from 0.25 to 0.64). The slope of linear regression between SM and EVI of TP-Hummock grassland was notably lower than that of two TP-Mulga woody sites (Figure 2-7d). Conversely, the parallel regression lines based on SM and SIF among all three TPs indicated slopes were nearly equivalent (Figure 2-7c). Figure 2-7e, 2-7f, 2-7g, 2-7h, 2-7i, and 2-7j show the seasonal trajectories between soil moisture and SIF, EVI during wet season (November - April) of 2010-2011, 2016-2017, and non-wet year mean respectively. In general, the slopes ( $k_{wet}$ ) between soil moisture and SIF, EVI in wet years were considerably larger relative to those ( $k_{non-wet}$ ) in non-wet year. Consistent with interannual comparison, the slopes ( $k_{wet}$ ) between SM and EVI in TP-Mulga were almost 1.5-2 times than that of TP-Hummock in contrast to comparable slopes ( $k_{wet}$ ) between SM and SIF.

## Inter-Annual

○ TP-Hummock g.    △ TP-Mulga w.    ◇ TP-Mulga s.    + 2010-2011    \* 2016-2017



## Seasonal

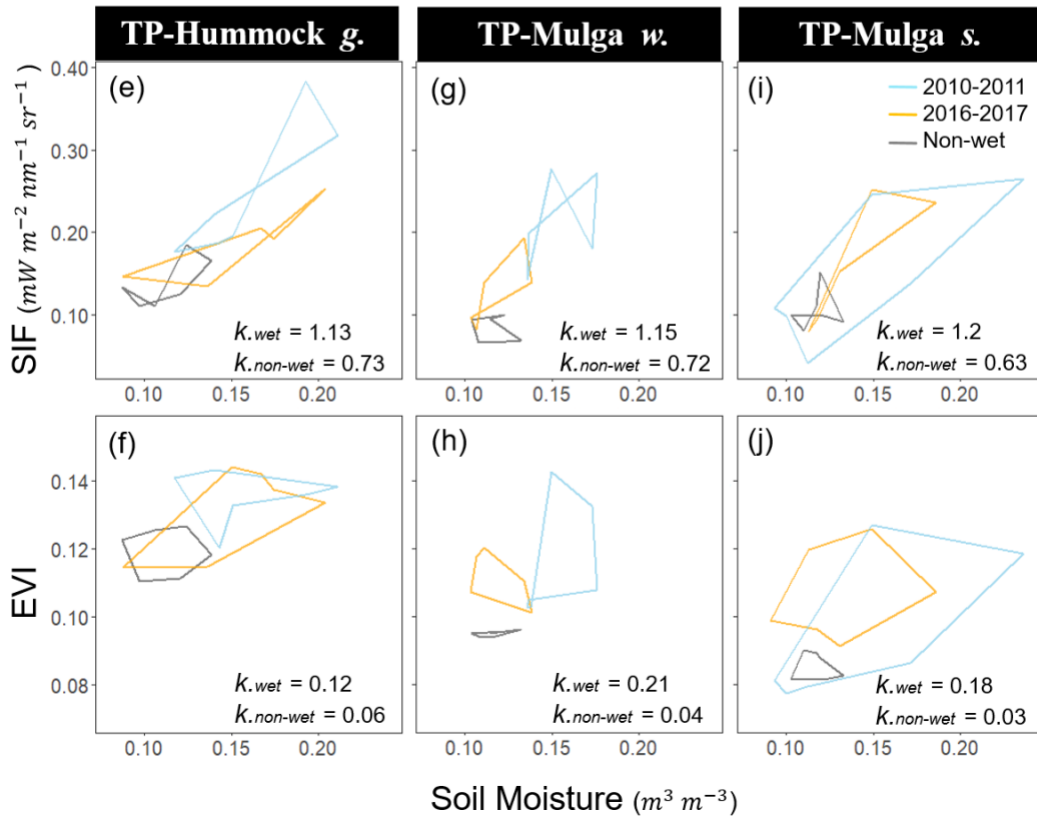


Figure 2-7 Cross-site relationship (a-d) between mean annual precipitation, soil moisture, SIF, EVI over three selected pixels. Vertical dashed lines refer to the multi-year mean of precipitation and soil moisture; Solid lines refer to the linear regression and the coefficient of determination ( $r^2$ ) of each TP are listed with corresponding color. (e-j) Seasonal trajectory between SM and SIF, EVI during wet season (Nov-Apr). k refers to the slopes of linear regression between SM and SIF, EVI during wet year and non-wet year.

Figure 2-8a presents the boxplots of pixel-wise maximum Pearson's correlation coefficients between 11-year series of monthly soil moisture and EVI and SIF among three major biomes. Satellite-based soil moisture can satisfactorily ( $p < 0.01$ ) explain seasonal and inter-annual variation in EVI of all major biomes ( $r_{max}$  ranging from 0.4 to 0.8), relative to less pronounced relevance with SIF ( $r_{max}$  ranging from 0 to 0.5). Apart from this, relationship between SIF and SM with larger standard deviation, especially among Hummock grassland and Mulga shrubland, tended to be more spatial variability (Figure 2-8a). In contrast to Hummock grassland and Mulga shrublands, EVI in Mulga woodland with minimum time lags (Lags = 0 or 1) was most sensitive to soil moisture availability, whereas SIF exhibited similarly proportional time lags for three biomes (Figure 2-8b). With reference to SIF within 17.8% of Hummock grasslands showing simultaneous response (Lag = 0), roughly all Hummock grassland (~99%) of EVI were lagging one month or more behind soil moisture.

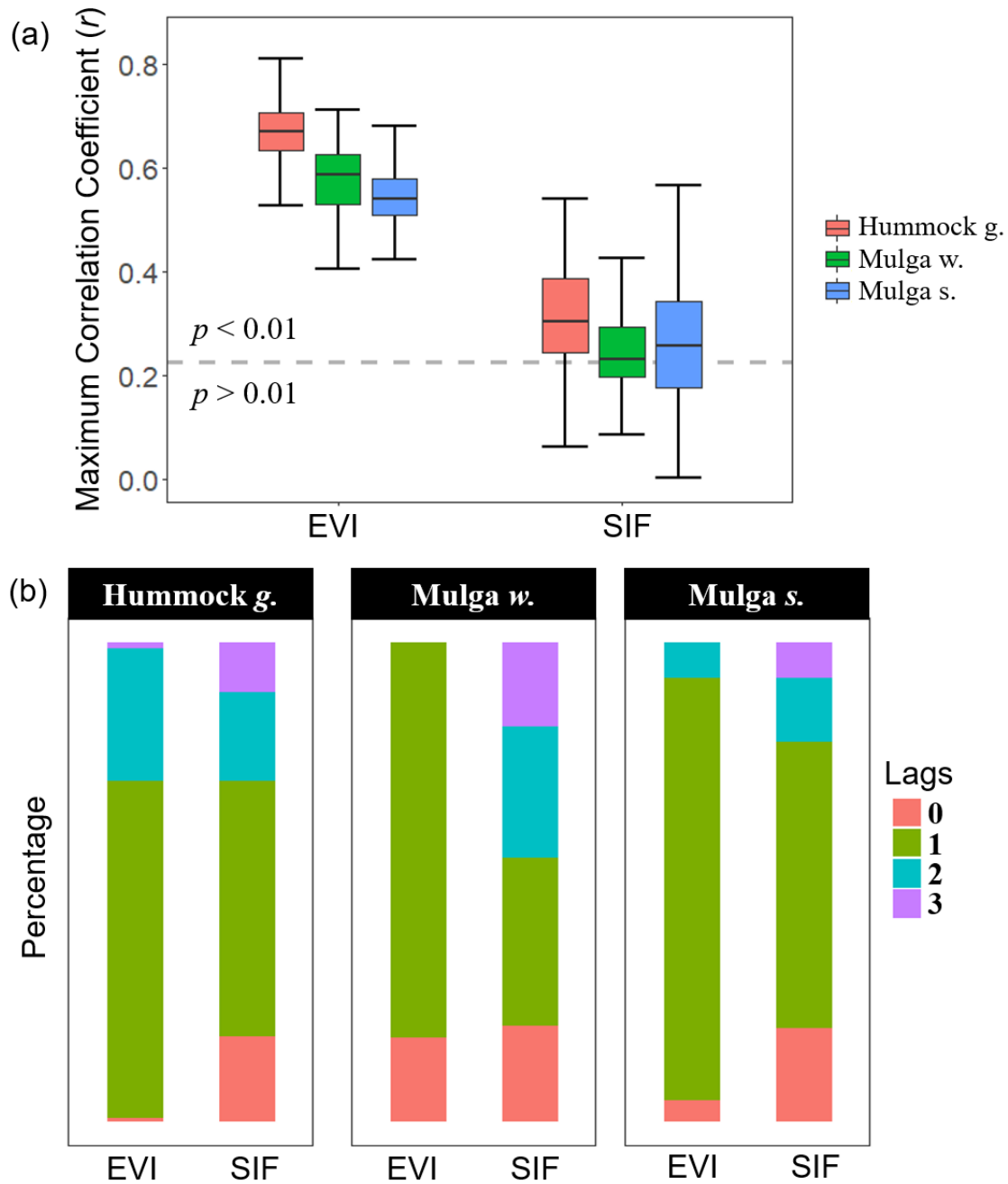


Figure 2-8 Relationship between soil moisture and EVI, SIF (a) Boxplot of maximum correlation coefficients between monthly Soil Moisture and EVI, SIF during 2007-2017 along with (b) the corresponding time lags (months). Above the dashed line represents  $p$  value below than 0.01 and vice versa.

### 2.3.3 SIF-EVI-GPP relationship

Both extreme wet events substantially raised the seasonal amplitude of GPP at AU-ASM, as well as AU-TTE in 2016-2017 (Figure 2-9a, 2-9b). The peak of

productivity of AU-ASM in 2016-2017 ( $GPP_{max} = 129.4 \text{ gC m}^{-2} \text{ mon}^{-1}$ ) slightly exceeded that in 2010-2011 ( $GPP_{max} = 114.9 \text{ gC m}^{-2} \text{ mon}^{-1}$ ) as well as that of AU-TTE in 2016-2017 ( $GPP_{max} = 116.3 \text{ gC m}^{-2} \text{ mon}^{-1}$ ). We found enhanced correspondence between GPP and SIF ( $r^2$ : 0.76, 0.62, and 0.85), GPP and EVI ( $r^2$ : 0.74, 0.91, and 0.6) in wet years relative to non-wet years ( $r^2$ : 0.44, 0.43, 0.59, and 0.71) for both AU-ASM and AU-TTE (Figure 2-9c~9f). Furthermore, the linear regression between GPP and two satellite-based variables in wet years ( $k$  ranging from 0.85 to 1.03) were closer to 1:1 diagonal, compared with those in non-wet year ( $k$  ranging from 0.63 to 0.82).

To examine the impact of mismatch footprint between flux tower measurement and satellite observation, relationships between multi-year series of GPP and vegetation variables are summarized with respect to a range of spatial resolution from 0.25 km to ~ 450 km (Figure 2-10). The correlation between GPP and EVI at AU-ASM were generally constant with increasing footprints of satellite observations from 0.25 km to 35 km ( $r^2$  ranging from 0.6 to 0.62), which were consistently stronger than those at AU-TTE ( $r^2$  ranging from 0.38 to 0.53). Subsequently, relationships at both sites decreased along with the footprints arising from 5 km to 45 km, especially for AU-TTE ( $r^2$  declined from 0.53 to 0.4). At a 0.5° spatial resolution of SIF data, correlations of SIF and EVI, SIF and GPP at two sites analogously increased and then decreased in conjunction with the extending size from 50 km to 450 km.

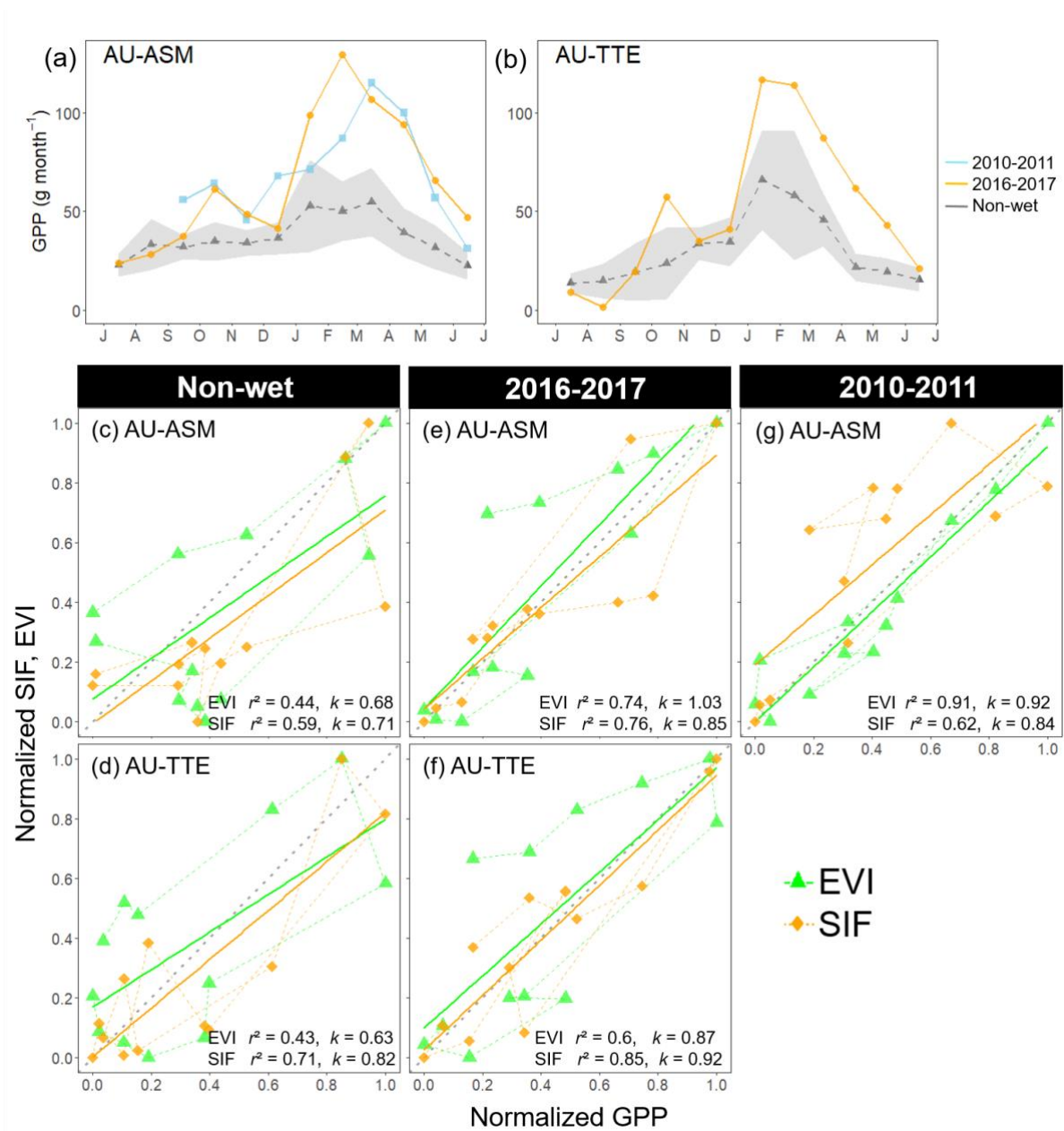


Figure 2-9 Comparison of satellite observation and tower-based measurement. (a, b) Seasonal variation in monthly GPP over AU-ASM and AU-TTE; (c-g) relationship between normalized GPP and SIF, EVI over flux tower sites during wet pulse years (2010-2011, 2016-2017) and non-wet year mean (2012-2015).

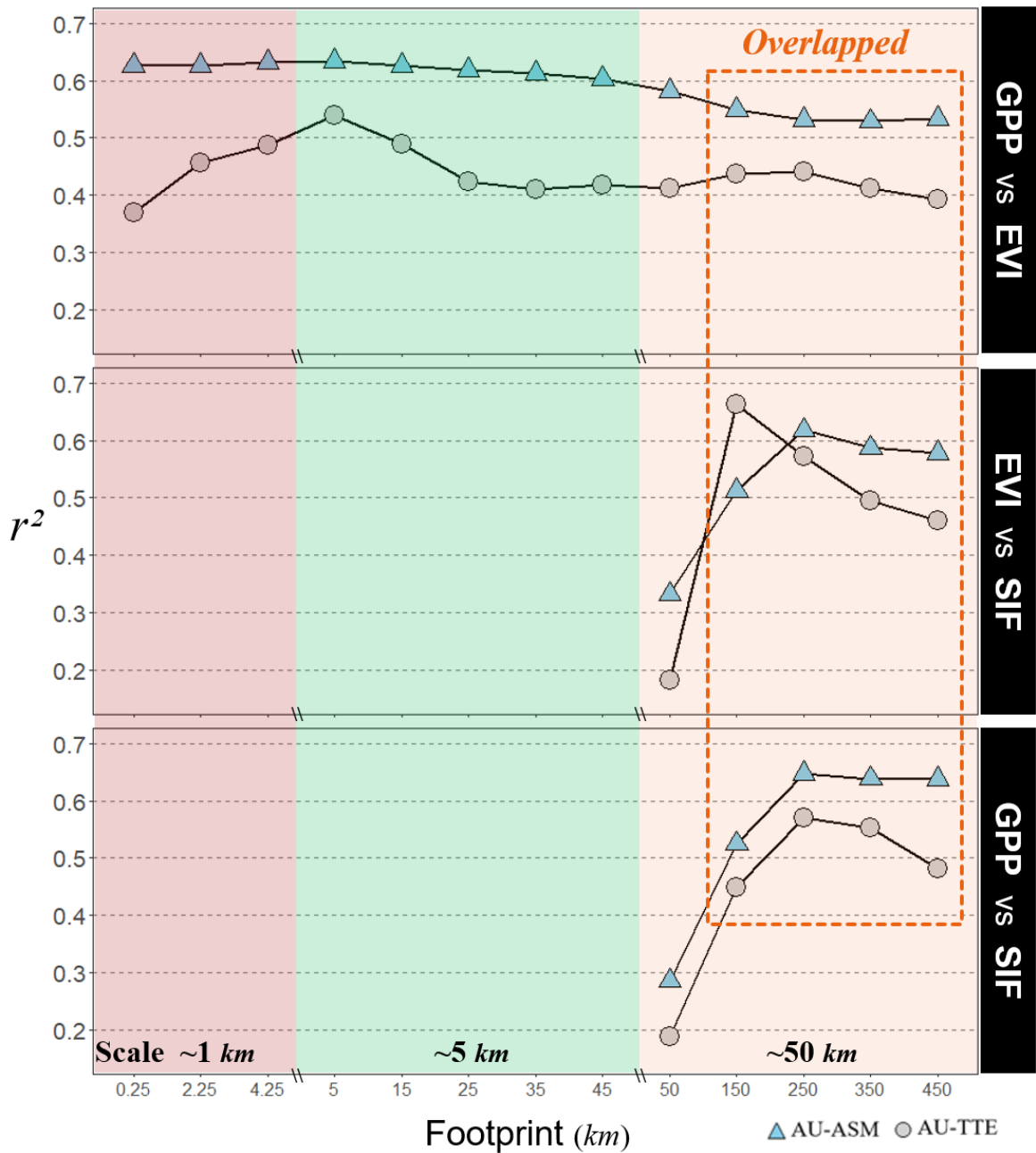


Figure 2-10 Coefficients of determination between multi-year series of tower-based GPP and EVI, EVI and SIF, GPP and SIF at a range of spatial resolution from 0.25 km to ~50 km ( $0.5^\circ$ ). Dashed orange rectangle refer to the footprints of satellite observation overlapped between AU-ASM and AU-TTE.

## **2.4 Discussion**

### **2.4.1 Spatiotemporal response to extreme wet pulse**

Both extreme wet pulses greatly promoted seasonal amplitude of SIF and EVI in comparison with non-wet years mean (Figure 2-2). Resembling seasonal profiles between hydro-meteorological and vegetation variables in both wet years implies that hydro-climatic variation exerts an impressive influence on vegetation dynamic across xeric interior of Australia, congruent with previous studies (Andrew, Guan & Batelaan 2017; Chen et al. 2014; Cleverly, Eamus, Restrepo Coupe, et al. 2016; Yang et al. 2014). In particular, EVI and SIF almost synchronously and rapidly reacting to extreme increasing moisture, however, varied in the post-wet period (Figure 2-2, 2-3). Our findings that EVI gradually decreased relative to the swift decline of SIF were also in line with other studies, ascribing this to a much slower of chlorophyll degradation compared with the reduction in photosynthesis (Jenkins et al. 2007; Ma et al. 2013). This rapid decline in SIF is due to the fact that a decrease in photosynthetic activity resulting from lowering soil water availability arise promptly through stomatal closure (Ma et al. 2013). In addition, differences in decreasing rates between SIF and EVI during the post-wet period is probably related to the accumulation of non-photosynthetic vegetation, and only the photosynthetic materials of plants drive photosynthesis process.

Unlike the corresponding spatiotemporal evolutions of EVI and SIF in the first wet event (Figure 2-3), two vegetation variables in 2016-2017 wet pulse exhibited inconsistent trends, of which EVI across almost entire domain was considerably positive anomalies in comparison to controversially spatial pattern of SIF<sub>SA</sub> (Figure 2-4). This result reveals that water availability may not be the only limiting factor for vegetation photosynthesis in semiarid ecosystem under extreme wet scenario, in addition to the occurrence of later wet pulse in hot summer (DJF: December-January-February). By measuring radiometric canopy temperature of Mulga in order to assess the thermal environment within the context of its photosynthetic thermal tolerances, previous studies found that 30°C was the thermal optimum for Mulga, and the response of Mulga to rainfall can be restricted by canopy temperature that surpass its thermal tolerance of 38°C as a result of constrained photosynthesis and growth (Eamus et al. 2016; Nix & Austin 1973). There is evidence that, on a seasonal basis, the primary drivers of vegetation productivity in an Australian tropical savanna respectively were soil moisture in the dry season and solar radiation in the wet season (Moore et al. 2018). Owing to above-average photosynthetically active radiation (PAR) in 2016-2017 wet pulse, another feasible reason causing discrepant responses between SIF and EVI is the degradation of GOME-2 instrument after operating over 11 years giving rise to the loss of signal-to-noise ratio, especially over low-productivity region (A et al. 2017; Dikty et al. 2011; Zhang, Joiner, et al. 2018).

#### **2.4.2 Sensitivity of Mulga and Hummock to water availability**

Responses of dryland vegetation to rainfall pulse depend on receipt of sufficient water to trigger a response (Cleverly et al. 2013). Besides, discrepancies in photosynthetic capacity between C<sub>3</sub>-dominated Mulga and C<sub>4</sub>-dominated Hummock dictate the timing and strength of ecosystem photosynthetic response (Barron-Gafford et al. 2012). Regardless of both wet events sustaining two-month, they differed in timing, magnitude and extent, in which extreme rainfall anomalies of 2016-2017 wet pulse mainly occurred over Hummock grasslands in contrast to that of 2010-2011 involving most vegetation types with extended coverage (Figure 2-5). At a given wet intensity, Mulga woodland showing invariably larger amplified magnitude of both EVI<sub>A</sub> and SIF<sub>A</sub> was most responsive among major biomes (Figure 2-6). Greenness of Mulga woodlands tended to be consistently more sensitive to soil moisture availability with larger slopes ( $k$ ) as well as least time delays (Figure 2-7, 2-8), indicating that rate of chlorophyll accumulation of Mulga is faster than that of Hummock grasslands. However, SIF of three major biomes exhibited comparable sensitivity with almost equal slopes as well as analogously proportional time lags, in spite of weaker correlation. Compared with EVI, the majority of SIF signal also lagged behind soil moisture, congruent with previous findings in central Australia (Detmers et al. 2015). In the xeric interior of Australia with sparse vegetation cover, satellite-based vegetation indices were found to be highly associated with

soil water content, with a one-month lag (Chen et al. 2014). Likewise, SIF signals derived from GOME-2 also correlates with greenness-based vegetation index (NDVI) and lags behind soil moisture (Detmers et al. 2015), which is consistent with our findings.

Soil moisture, rather than precipitation, could explain most vegetation variations both seasonally and interannually (Figure 2-7, 2-8), reflecting that satellite-observed soil moisture can be an effective indicator of dryland vegetation growth (Nicolai-Shaw et al. 2017; Qiu et al. 2018). Chen et al. (2014) reported that satellite-derived soil moisture was significantly positive related with NDVI across mainland Australia with a typical time scale of soil moisture preceding NDVI by one month. Similar findings in (Yang et al. 2014) demonstrate total water storage anomaly (TWSA) derived from the Gravity Recovery and Climate Experiment (GRACE) is a better sign of surface greenness over mainland Australia relative to precipitation, and they argued spaceborne soil moisture was measured within top several centimeters, rather than root-zone moisture.

Nevertheless, Mulga has a dimorphic root distribution with the majority of the root biomass in the top 10 cm of the soil (Cleverly, Eamus, Restrepo Coupe, et al. 2016) and is highly susceptible to minor variation in the upper moisture content (Eamus et al. 2013). Along with follow-on GRACE mission launched in 2018 (Flechtner et al. 2018), it offers a chance to comprehensively evaluate

interactions between vegetation dynamics and multiple hydro-meteorological drivers in future research.

### **2.4.3 Assessment with tower-based GPP**

Based on the mechanism introduced by the Equation 2-4, many previous studies revealed that spaceborne SIF was shown to strongly correlated with gross primary production, and the SIF-GPP (tower-based measurement) linear relationship has been validated (Chang et al., 2019; Chen et al., 2019; Guanter et al., 2014). In this study, we found moderate correspondence between satellite-observed SIF, EVI and tower-based GPP monthly climatologies in non-wet years (Figure 2-9c, 2-9d), consistent with findings of Madani et al. (2017), in which they suggested that the weaker relationship in central Australia reflect greater SIF uncertainty over sparsely vegetated region relative to mesic ecosystem. By contrast, remarkably enhanced correlations between GPP and SIF, GPP and EVI in both wet years of 2010-2011 and 2016-2017 (Figure 2-9e~9g), along with closer slopes ( $k \cong 1$ ), suggests that satellite-based variables can better estimate productivity of dryland vegetation under wet condition.

Considering notable mismatch between footprints of flux tower measurement and satellite observation, we investigated the relationships at a range of spatial resolution (Figure 2-10). On account of located in an extensive high-density Mulga woodlands, the coefficient of determination at AU-ASM were constantly around 0.6 regardless of increasing footprints from 0.25 km to 45 km,

consistently larger than those at AU-TTE as a consequence of higher heterogeneous landscape (Cleverly, Eamus, Van Gorsel, et al. 2016). Since a coarser spatial resolution (~50 km), the relationship between GPP and EVI were weaker than those at around 5 km footprints, and the strength of correspondence of both sites were closer owing to overlapped footprints. Conversely, widely fluctuated relationships with respect to SIF reveal that this product perhaps remains with much uncertainty and its high retrieval noise in low productivity region induces notable speckling relative to EVI and GPP (A et al. 2017; Gentine & Alemohammad 2018). On a basis of spatially coarse resolution and degradation of GOME-2 instrument, heterogeneity remains in the biome-level analysis though we set stringent criteria for “pure” pixels selection. For a more in-depth study, improved SIF datasets with higher spatiotemporal resolution in comparable with the footprint of flux tower measurement would be highly needed. In addition, scarcity of flux tower sites in the interior of Australia impedes broad validation of satellite observations over most vegetation types.

## **2.5 Conclusions**

We have examined the response of satellite-observed SIF and EVI to 2010-2011 big wet as well as a recent extreme wet pulse in 2016-2017 over arid central Australia mainly covered by Hummock grasslands, Mulga woodlands, and Mulga shrublands. We found EVI with markedly amplified seasonal amplitude was significantly responsive to both extreme wet events. In contrast to

predominantly positive anomalies of SIF in 2010-2011, SIF over nearly half region showed negative anomalies in 2016-2017 wet pulse. Although C<sub>4</sub>-dominated Hummock grasslands experienced larger amount of rainfall in 2016-2017, C<sub>3</sub>-dominated Mulga woodland was invariably most responsive biome, ascribed to its strong sensitivity to moisture availability. In spite of a robust linear SIF-GPP relationship at site level, SIF derived from GOME-2 has imperfect capacity for capturing spatial dynamics over xeric central Australia. This research provides a case study to reveal the process regarding interactions between climate anomalies and vegetation anomalies, which could be beneficial to other precipitation-driven ecosystems. With projection of increasing extreme events in the future, identifying ecological responses to climate disturbances contributes to our understandings for sustainable managing of ecosystem services.

# **Chapter 3 Assessing the Impact of Extreme Droughts on Dryland Vegetation by Satellite Solar-induced Chlorophyll Fluorescence**

## **Abstract**

Over the past two decades of the new century, the 2018-2019 extreme drought across inland Australia was recorded as the worst event, with vast areas suffering from exceedingly rainfall deficit as well as contemporaneous heat waves. Satellite-estimated solar-induced chlorophyll fluorescence (SIF) is proved to be as an effective indicator for dynamic drought monitoring, however the capability of SIF to assess the variability of dryland vegetation under water and heat stress remains unclear. This study presents an analysis of the responses of Australia's dryland vegetation to the drought events at different severity and time scales using multi-source spaceborne SIF as well as enhanced vegetation index (EVI). The results demonstrate satellite-observed SIF has potential for characterizing and monitoring the spatiotemporal dynamics of drought over water-limited ecosystems in spite of high-retrieval noise. While SIF could earlier detect drought-related loss in vegetation than EVI over northern mesic ecosystem, both variables simultaneously captured the losses of arid/semiarid plants growth in the beginning of drought at monthly and 16-day scales. Semiarid ecosystems showing the largest reductions were most sensitive to climate extremes regardless of drought severity and time scales. Furthermore, our study highlights that SIF retrieved from recently launched TROPospheric

Monitoring Instrument (TROPOMI) featuring substantially enhanced spatiotemporal resolution has promising capability of accurately tracking the drought-induced variation of heterogeneous dryland vegetation.

## **Keywords**

Extreme drought, SIF, EVI, Dryland

## **3.1 Introduction**

Large-scale drought, as one of most costly and pressing natural hazards, has profound impacts on terrestrial ecosystems, water resource, agriculture, and social economics (Jiao, Chang & Wang 2019). As a consequence of highly variable climate, Australia is particularly vulnerable to extreme drought, as evident by Millennium Drought (2001-2009) in Murray-Darling basin as well as 2012-2013 drought over arid inland (Ma et al. 2016; van Dijk et al. 2013).

Australia tends to be a global hot spot for variability, with semiarid vegetation in that country exhibiting increased carbon uptake (Haverd et al. 2017). By persisting through the ‘big dry’ and responding favourably in a following ‘big wet’ (Xie et al. 2019), Australia’s ecosystems play a significant role in regulating the global water and carbon cycles (Ma et al. 2016). Enhancing our understanding with respect to dryland ecosystem in response to climate extreme is paramount for effectively managing environment and global change research (Broich et al. 2018).

Satellite-based observation offers a new perspective to monitor and characterize the spatiotemporal dynamics of vegetation under changing climates (Huete et al. 2008), especially valuable for the remoteness of Australia's interior with sparse monitoring sites. Traditional reflectance-based vegetation indices (e.g. EVI, NDVI) are widely applied to assess the effects of extreme drought on ecosystem functioning and vegetation productivity at regional, continental, or global scale (Broich et al. 2018; Kath et al. 2019; Wang, Yang, et al. 2019; Xu et al. 2018). Dramatic impacts of climate extremes on vegetation dynamics (as measured by EVI) with abrupt changes in phenology and productivity over southeast Australia demonstrates that semiarid ecosystems exhibit the largest sensitivity to hydro-climatic variations (Ma et al. 2015). Although vegetation-index-based approaches are essential for evaluating vegetation variation under large-scale drought event, the observations they provide are not directly associated with vegetation functioning (Sun et al. 2015).

During recent years, satellite retrievals of SIF based on energy reemitted directly from the core of photosynthetic machinery present a fresh manner to observe vegetation growth and response (Frankenberg et al. 2011; Guan et al. 2015; Sun et al. 2017). On account of energy conservation, variations in SIF signal include information regarding vegetation physiological, biochemical, and metabolic functions in addition to the amount of absorbed photosynthetically active radiation (Sun et al. 2015). Numerous studies have examined the

relationship between GPP and SIF for each biome at various scales retrieved from different satellite sensors (Frankenberg et al. 2018; Guan et al. 2016; Kira & Sun 2020; Yang et al. 2015), implying that SIF can be an unbiased monitoring of vegetation productivity and further contribute to understanding of global terrestrial carbon cycle (Biederman et al. 2017; Guanter et al. 2014). Both SIF and GPP based on Moderate Resolution Imaging Spectroradiometer (MODIS) respond to water availability in much same direction beyond their previously determined correlations, despite biome-specific distinction remains manifest (Short Gianotti et al. 2019).

Relative to traditional VIs, spaceborne SIF or fluorescence yield ( $SIF_{yield}$ ) was found to show earlier and more significant responses to rainfall deficits and heat stress over tropical vegetated region, forest, and cropland at monthly scale (Song et al. 2018; Zhang et al. 2019). It highlights that SIF is sensitive to both the structural and physiological variations of vegetation and can be beneficial to timely monitor and characterize the development of drought and heatwave (Qian, Qiu & Zhang 2019; Wang, Qiu, et al. 2019). During the extreme drought of 2015-2016 driven by a strong El Nino event, large-scale decoupling of greenness and photosynthesis over Amazon forests was observed by satellite, of which SIF showed a pronounced reduction as opposed to slightly increase of canopy greenness (Yang et al. 2018). The magnitude of divergence in greenness (as measured by EVI) and photosynthesis (as measured by SIF) that are related

to times of fluctuant soil moisture differ in sign along a tree cover gradient, of which those of forested ecosystems display contrasting average responses (Walther et al. 2019). Conversely, both greenness and photosynthesis of nonwoody semiarid ecosystems exhibiting strong response to the availability of soil moisture usually alter contemporaneously (Walther et al. 2019). To assess the effect of drought-related stress on terrestrial ecosystems, a superior remotely-sensed indicator is needed, which can measure not only how green the plants are, but also what the rate of photosynthetic activity is.

By investigating the response of vegetation growth to the 2019 extreme heatwave in central Australia, Qiu et al. (2020) concluded SIF observed by both GOME-2 and Orbiting Carbon Observatory-2 (OCO-2) are more sensitive to water and heat stress than is the greenness-based vegetation index (EVI). In addition, OCO-2 SIF exhibits more pronounced decrease and one-month earlier than does GOME-2 SIF, primarily owing to the diverse timing of observations (overpass timing: GOME-2 at near 09:30 a.m. and OCO-2 at 1:36 p.m. local solar time). Nonetheless, this study was conducted at a relatively coarse scale (1-degree grid and monthly) as well as limited baseline years (2015-2019), and it therefore remains uncertainties for relatively heterogeneous dryland vegetation under highly dynamic climate. The newly launched TROPOMI facilitates a considerable enhancement in SIF observation as a result of unprecedented spatial resolution (up to  $7 \text{ km} \times 3.5 \text{ km}$  at nadir) and near-daily

global coverage as contrasted with GOME-2 and OCO-2 (Doughty et al. 2019; Köhler et al. 2018), that enables to assess the relationship of SIF-GPP at ecologically meaningful scale.

Characteristic drought time-scale can play a critical role in determining the sensitivity of biome-specific vegetation to drought (Vicente-Serrano et al. 2013). Arid and humid biomes mostly respond to short time-scales, while semiarid and subhumid biomes respond at long time scales (Vicente-Serrano et al. 2013). The response of the annual crop yield in five main dryland cultivations in the United States to different time-scales of drought is highly spatial variable, of which some crops (e.g. winter wheat) responded to drought at medium to long Standardized Precipitation Evapotranspiration Index (SPEI) time-scales, while other crops (e.g. soybean and corn) responded to short or long drought time-scales (Peña-Gallardo et al. 2019). While there remains unclear how does major biome type of natural dryland vegetation respond to drought at diverse drought severity as well as various drought duration.

Here, we utilise the large-scale 2018-2019 drought across Australia as a natural experiment to investigate and characterize the spatiotemporal response of dryland biomes to this extreme event using multiple-source satellite observations of solar-induced chlorophyll fluorescence and vegetation greenness. Specifically, our objectives are: (1) to assess the potential of spaceborne SIF for monitoring drought dynamics over water-limited

ecosystems; (2) to identify spatiotemporal patterns in the response of dryland vegetation to major drought at different severity and time scales; (3) to contrast the variability of fluorescence and greenness of dryland biomes under extreme drought.

## **3.2 Materials and Methods**

### **3.2.1 Study area**

This study was conducted at a sub-continental scale between 10°S to 26°S and 113°E to 138°E, which encompassed northern and central Australia by a relatively constant decrease in rainfall with distance inland (Figure 3-1). This region, particularly for northern Australia, has a classic monsoon climate pattern, which receives more than 80% of annual precipitation during November to April (Ma 2013). From northern mesic tropics to the xeric central Australia, mean annual rainfall ranges from 1700 mm to approximately 300 mm (Ma 2013), in line with the aridity index (AI) decreasing from 0.8 to nearly 0.1 (Figure 3-1b).

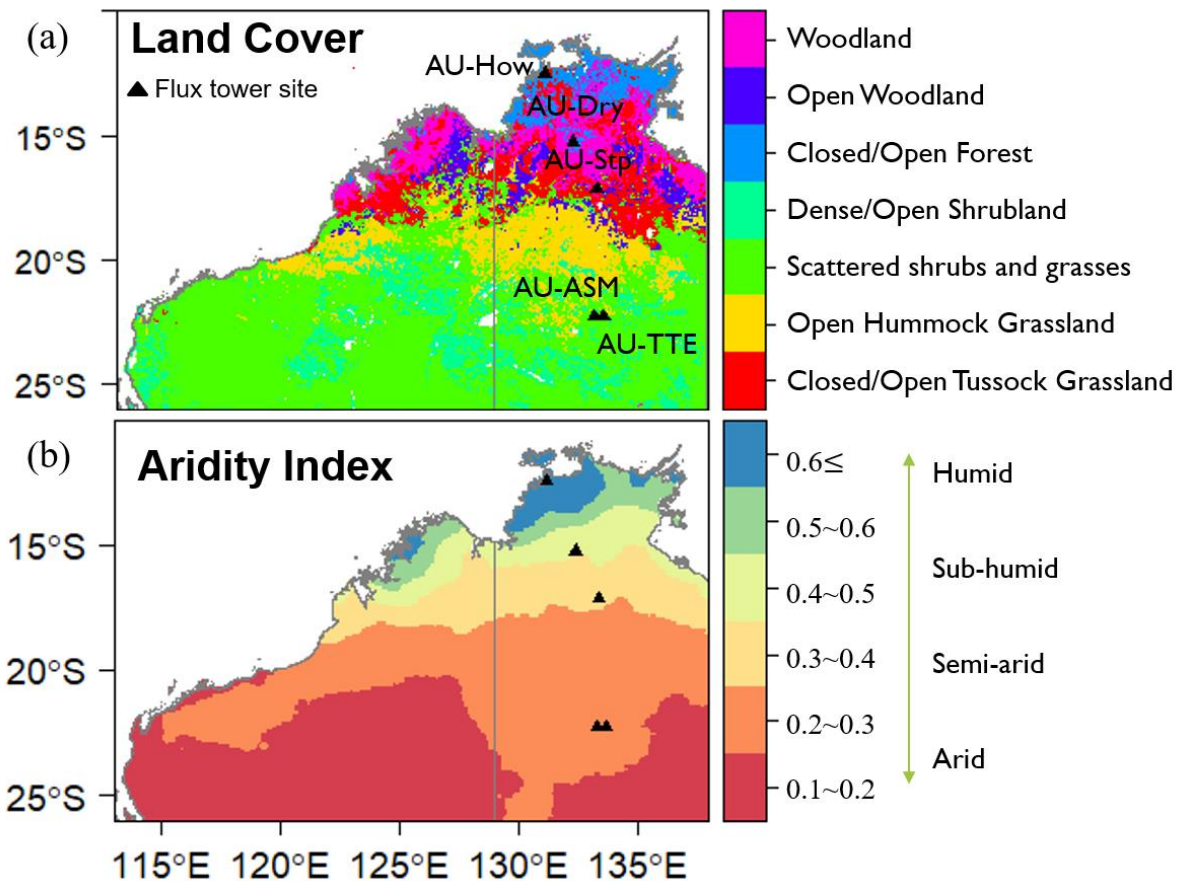


Figure 3-1 (a) Land cover map based on national Dynamic Land Cover Dataset (DLCD). (b) Spatial pattern of aridity index. Black triangles refer to five flux tower sites.

Correspondingly, the vegetation follows a wet-dry gradient that shifts from Eucalyptus dominated forests, open forests, and woodlands in the coastal northern areas to Acacia-dominated open woodlands, scattered shrubs, and hummock grassland into the vast inland (Ma 2013) (Figure 3-1a).

To assess satellite observation with ground-based evidence, we selected five representative flux tower sites across the extensive study area: Howard Springs (AU-How [131.15°E, 12.495°S]), Dry River (AU-Dry [132.371°E, 15.259°S]), Sturt Plain (AU-Stp [133.3502°E, 17.1507°S]), Alice Spring Mulga (AU-ASM, [133.2493°E, 22.2828°S]), and Ti Tree East (AU-TTE [133.64°E, 22.287°S])

(Beringer et al. 2016). Apart from two northern site (AU-How and AU-Dry) under moderate dry, the remaining sites were experiencing extreme dry condition in monsoon season of 2018-2019.

### **3.2.2 Satellite data**

In this study, we utilised two set of satellite-based SIF records. (1) The first dataset was obtained from Global Ozone Monitoring Experiment-2 (GOME-2) on board EUMETSAT's MetOp-A as well as MetOp-B platform (indicated as GOME-2A and GOME-2B respectively). The GOME-2 instrument is a nadir-scanning spectrometer, which measures at around 9:30 local equator crossing time, and it has a relatively large footprint (approximately 40 km x 80 km at nadir, before 15 July 2013, and 40 km x 40 km since 15 July 2013). GOME-2 comprises four main optical channels with the spectral range from 240 to 790 nm, and the fourth channel ranges between 590 and 790 nm with a spectral resolution of approximately 0.5 nm and a relatively high signal-to-noise ratio (Joiner et al., 2013; Song et al., 2018a). This dataset is primarily retrieved from the filling-in of solar Fraunhofer lines in the vicinity of the 740 nm far-red fluorescence emission peak, based on a simplified radiative transfer model in the company of a principal component analysis in order to disentangle the fluorescence signals from atmospheric absorption, surface reflectance (Joiner et al. 2013; Köhler, Guanter & Joiner 2015). GOME-2 SIF records with a limited amount of validation provide substantially enhanced sampling and precision

relative to the filling-in signal at 758 nm from Japanese Greenhouse gases Observing SATellite (GOSAT) TANSO-FTS instrument (Joiner et al., 2013)

Both datasets (GOME-2A, GOME-2B) are retrieval of the far-red chlorophyll fluorescence peaking at 740 nm, based on a simplified radiative transfer model in the company of a principal component analysis (Joiner et al. 2014). Monthly global coverage of SIF data at  $0.5^{\circ} \times 0.5^{\circ}$  spatial resolution (level 3, Version 28) from February 2007 to March 2019 was obtained from NASA Goddard Space Flight Centre (<https://avdc.gsfc.nasa.gov/>). Given the degradation of GOME-2 instrument during its life time, SIF data observed from MetOp-B platform was also downloaded, that spans from March 2013 to March 2019. The daily orbital data (level 2, Version) was also used to aggregate 16-day interval records for higher temporal-resolution analysis. (2) We also used a newly released SIF dataset based on TROPOMI onboard Sentinel-5 Precursor satellite. Relative to GOME-2, TROPOMI measures SIF signals at substantially enhanced spatial resolution with a footprint of  $3.5 \times 7 \text{ km}^2$  at nadir (Köhler et al., 2018; Wang et al., 2020). The satellite's local time of ascending node crossing of 13:30 has been chosen to facilitate the so-called loose formation operation with NASA's Suomi-NPP spacecraft (Doughty et al., 2019; Köhler et al., 2018). The TROPOMI instrument combines the strengths of the Scanning Imaging Absorption spectrometer for Atmospheric Chartography (SCIAMACHY), Ozone Monitoring Instrument (OMI), and state-of-the-art technology to provide observations with performances that can be superior to the current instruments

in space. A data-driven method was employed to retrieve the SIF signal using spectral measurements ranging from 743 nm to 758 nm (Köhler et al. 2018). Daily corrected ungridded TROPOMI SIF data at a 0.05 spatial resolution (2018-2019) was available at (<ftp://fluo.gps.caltech.edu/data/tropomi/>). In this study, the daily orbital TROPOMI SIF were likewise aggregated to monthly and 16-day series by mean value.

We used Moderate Resolution Imaging Spectroradiometer (MODIS on board Aqua, Collection 6) MYD13C1 (0.05°, 16-day) and MYD13C2 (0.05°, monthly) Vegetation Indices products from January 2007 to June 2019 downloaded from NASA Earth Observation data (<https://search.earthdata.nasa.gov/search>). EVI is an optimized version of vegetation indices that effectively reduces soil background influences and is widely used as a proxy of canopy greenness. The equation of EVI is:

$$EVI = 2.5 \frac{\rho_{NIR} - \rho_{red}}{\rho_{NIR} + 6\rho_{red} - 7.5\rho_{blue} + 1} \quad (6)$$

where  $\rho_{blue}$ ,  $\rho_{red}$ ,  $\rho_{NIR}$  are reflectance in the blue, red and near infrared bands respectively. To reduce noise and uncertainties, only best quality data was remained in this study through removing pixels of which quality control flag of the first 2 bits neither 00 nor 01, and pixel-wise EVI time series data was smoothed using Savitzky-Golay filter.

As a spatial reference, satellite-based data-driven gross primary productivity (FluxSat\_GPP, version 1.1, 2007-2019) derived primarily from MODIS reflectance product were obtained from NASA Goddard Space Flight Centre (<https://avdc.gsfc.nasa.gov/>). This is a monthly dataset with 0.5° spatial resolution, calibrated by a set of the FLUXNET 2015 eddy covariance data (Joiner et al. 2018).

To assess the response of dryland biomes to heat stress, MODIS daytime land surface temperature (LST, MYD11C3) at monthly scale was included in this study, collected from NASA Earth Observation data (<https://search.earthdata.nasa.gov/search>). Similarly, best quality data was remained through eliminating pixels with quality control flag.

Monthly photosynthetic active radiation (PAR) at 1° resolution grid was downloaded from the NASA Langley Research Centre, Cloud and Earth's Radiant Energy System (CERES, Ed4.1), including adjusted surface PAR both direct and diffuse fluxes under all sky condition. The total PAR was computed as the sum of both direct and diffuse PAR (Wang 2019), and then used to remove the effects of PAR on SIF by normalizing after aggregating into SIF grid resolution:

$$SIF_{PAR} = \frac{SIF}{PAR} \quad (7)$$

Global monthly precipitation at 0.1° resolution grid based on Integrated Multi-Satellite Retrievals for Global Precipitation Measurement (IMERG, Version 6, Final run, 2007-2019) was collected from NASA Precipitation Processing System (<https://pps.gsfc.nasa.gov/>).

### **3.2.3 Climate Data and Land cover map**

In this study, we utilised monthly the Standardized Precipitation Evapotranspiration Index to characterize the spatial and temporal dynamics of the 2018-2019 extreme drought event across Australia. This dataset with 1-month, 6-month time-scale (indicated as SPEI<sub>1-month</sub>, SPEI<sub>6-month</sub> respectively) at 1° spatial resolution, representing the cumulative water status (deficit or surplus) over the preceding 1 or 6 months, was downloaded from SPEI Global Drought Monitor (<https://spei.csic.es/>).

To assess the relationship between climatic drivers and vegetation variables under drought stress, monthly air temperature (at 2-m height) and soil moisture content (surface 0-7cm depth, root zone 28-100 cm depth) based on ERA-5 reanalysis data were downloaded from Copernicus Climate Change Service (<https://cds.climate.copernicus.eu/>).

Gridded annual potential evapotranspiration (PET) and monthly mean decadal precipitation were collected from Bureau of Meteorology (<http://www.bom.gov.au/>). Firstly, we converted monthly precipitation into

annual scale, and then aggregated into 0.1 spatial grid consistent with PET. Secondly, aridity index was computed as annual precipitation normalized by annual PET. The equation is:

$$AI = \frac{P}{PET} \quad (8)$$

where  $P$  refers to mean annual precipitation (unit: mm), and  $PET$  refers to mean annual potential evapotranspiration (unit: mm). Finally, pixels within the entire study area were binned by AI (every 0.1 increment) into 6 groups from humid to arid region, as shown in Figure 1b.

National Dynamic Land Cover Dataset (DLCD) was used in this research, obtained from Geoscience Australia and Bureau of Agricultural and Resource Economics and Sciences (<http://www.ga.gov.au/scientific-topics/earth-obs/landcover>). Given that some biome types were covering few pixels within entire study region, Closed tussock grassland, Dense shrubland, and Closed forest was respectively re-grouped into Open/closed tussock grassland, Dense /open shrubland, and Closed/open forest (Figure 3-1a). This dataset validated with abundant field sites was aggregated to 0.5° spatial resolution by most frequent values.

### **3.2.4 Eddy Covariance data**

We used five selected flux towers to interpret the satellite-observed dynamic of vegetation under different drought severity. The original level 3 (AU-How, AU-

Dry, AU-Stp) and level 6 (AU-ASM, AU-TTE) flux data provided by the OzFlux network (<http://www.ozflux.org.au/>) were used to pre-process, including quality control assessment, removal of outliers, and gap-filling (Cleverly et al. 2013). Flux partitioning for level 3 data was conducted in open source R scientific computation environment (Version 3.5.1) associated with REdDyProc package (Version 1.2). The half hour flux data were aggregated into monthly and 16-day GPP to match with satellite-based observations.

### **3.2.5 Analysis**

To investigate the responses of dryland vegetation to different drought severity, we defined two categories of dry condition based on  $SPEI_{6\text{-month}}$  in April 2019, extreme drought ( $SPEI \leq -2$ ) and medium drought ( $-2 < SPEI \leq -0.5$ ).

Subsequently, the statistic ( $SPEI_{1\text{-month}} \leq -2$ ) was conducted during the 2018-2019 monsoon season (November to April) for generating the pixel-wise number of extreme-dry month. Besides, we aim to examine the spatiotemporal variability of SIF and EVI under different drought severity over Australia's dryland ecosystem. Therefore recent drought events including 2018-2019, 2015-2016, and 2012-2013 in central Australia were also investigated and inter-compared.

To further examine the response of dryland biomes to diverse drought severity at regional scale, we selected four-pair region of interest (ROI 1-4) distributed

from mesic northern to xeric southern areas. The ROI selection criteria are: (1) identical or highly similar biome types in each pair; (2) among each pair, the one was under extreme dry condition and the other under medium dry; (3) covering major dryland region (sub-humid, semi-arid, to arid). ROI-1 are mainly covered by woodlands & open woodlands. ROI-2 and ROI-3 are covered by scattered shrubs & grasses. Vegetation in ROI-4 is dominated by Hummock grasses mixed with scattered shrubs. In addition, two pairs of selected ROIs also experienced respectively the 2012-2013 and 2015-2016 drought event to test the coherence of vegetation in response to drought severity.

With the purpose of drought-related signals detection by eliminating seasonality, monthly anomalies ( $\Delta X$ ) and standardized anomalies ( $SA$ ) of all the aforementioned variables were calculated as a deviation from their corresponding multiyear (2007-2018) mean of each month. The equations are:

$$\Delta X_i = X_i - \bar{X}_i \quad (9)$$

$$SA_{ij} = \frac{X_{ij} - \bar{X}_j}{\sigma_j} \quad (10)$$

where  $i$  is the yearly temporal coverage from 2007 to 2018,  $X_{ij}$  is the monthly ranging from July to June,  $\bar{X}_j$  and  $\sigma_j$  are the mean and standard deviation of time series  $x$  at month  $j$ .

To quantify the relationship between satellite-based observation and tower-based measurement under drought stress, the coefficient of determination ( $r^2$ ) was calculated across five selected tower sites at different spatial (GOME-2 SIF:  $0.5^\circ$ ; TROPOMI SIF:  $0.05^\circ$ ) and temporal (monthly, 16-day) resolutions. MODIS EVI at  $0.05^\circ$  spatial resolution was also aggregated in  $0.5^\circ$  grid, with the purpose of contrasting with GOME-2 SIF at a coarser scale. All satellite datasets were extracted from a  $3 \times 3$  window centered on each flux tower site respectively. A  $t$  test was utilized to examine the statistical significant level of the relationships ( $p$ -value).

Data processing, analysis, and visualization were conducted in open source R scientific computation environment (Version 3.6.2) and associated packages contributed by the R user community (<http://cran.r-project.org>).

### **3.3 Results**

#### **3.3.1 Spatiotemporal dynamics of the 2018-2019 extreme drought**

The extreme, 4-month drought spanning from December 2018 to March 2019 was the worst drought event during the last two decades over central and northwest Australia (Fig. 3-2a, 3-2b), of which almost entire region was influenced by this event (Fig. 3-3a) based on  $SPEI_{6\text{-month}}$ . During whole 2018-2019 monsoon season, nearly 75% of the area was under extreme dry condition covering from north to xeric southern central Australia ( $15^\circ$ - $26^\circ$ S and  $118^\circ$ - $138^\circ$ E), particularly in December 2018 and January 2019. In addition, the xeric

inland experienced longer extreme dry period (more than 2 months) relative to the mesic northern coastal regions (Fig. 3-3).

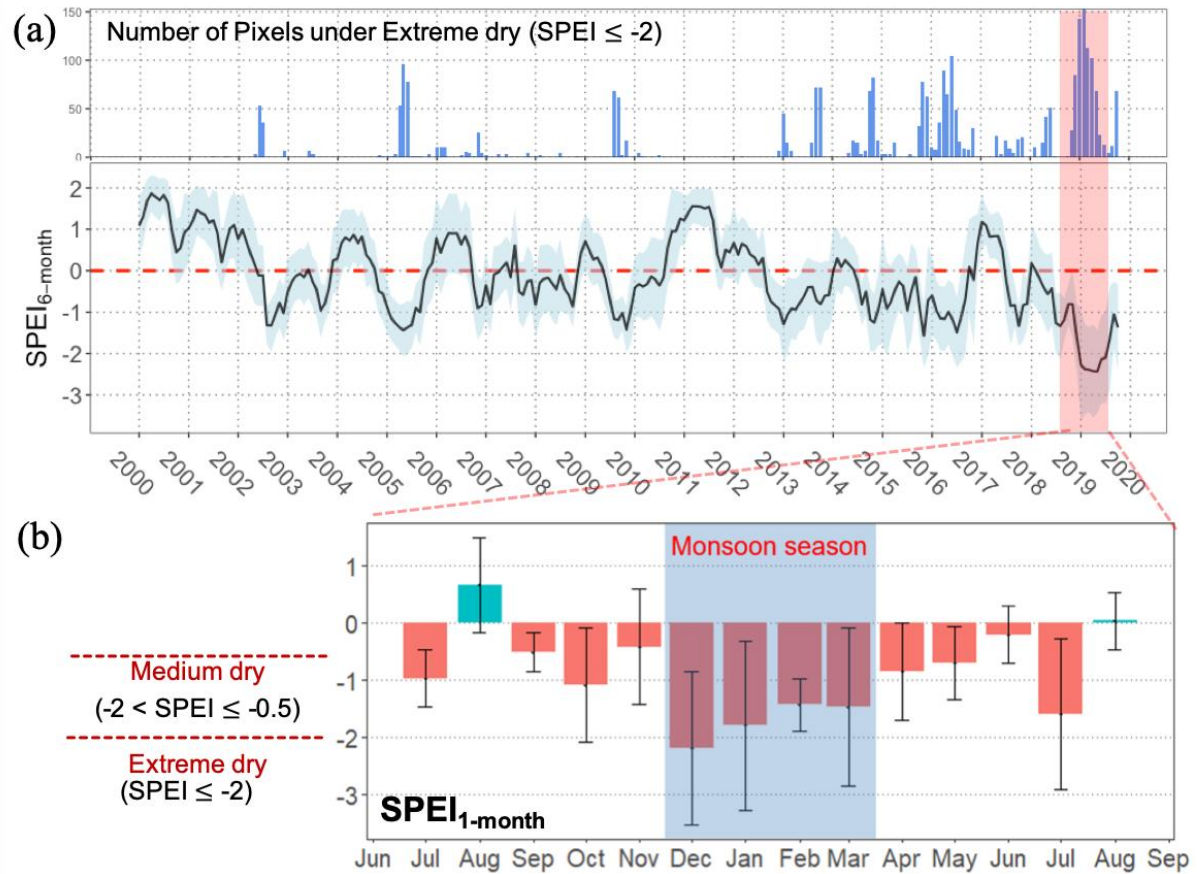


Figure 3-2 (a) Region-wide mean monthly SPEI<sub>6-month</sub> along with pixel counting under extreme dry (SPEI ≤ -2) from 2000-2019 and (b) monthly SPEI<sub>1-month</sub> during 2018-2019.

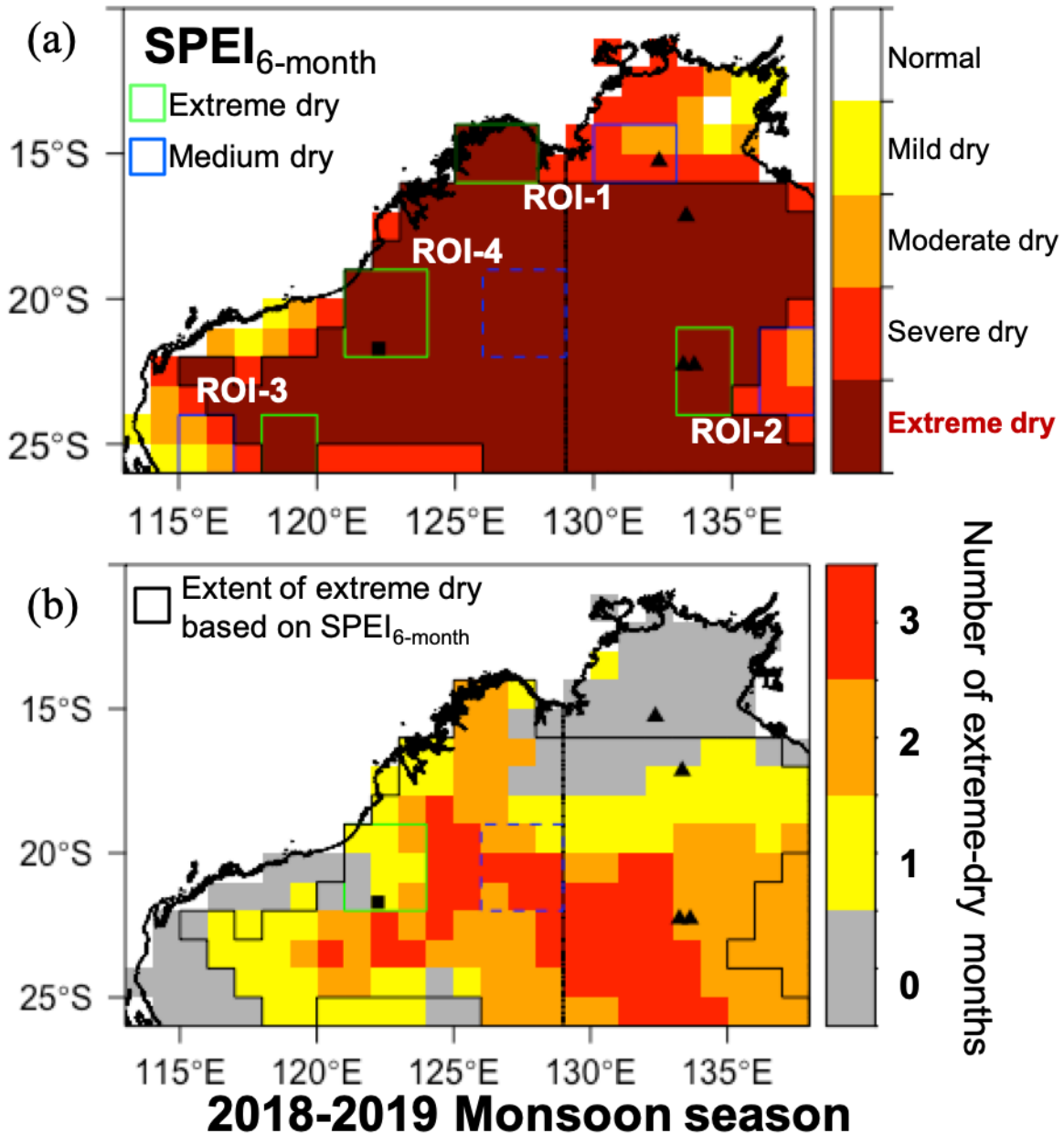


Figure 3-3 (a) Spatial pattern of drought severity based on  $SPEI_{6\text{-month}}$  during 2018-2019 monsoon season (November - April). (b) Pixel-wise number of extreme-dry months during 2018-2019 monsoon season based on  $SPEI_{1\text{-month}}$ . Four pairs of ROIs (1-4) are shown in Fig.3a. The black boundary represents the extent of extreme (within) and medium (outside) dry in 2018-2019.

Temporal variations in satellite-based SIF,  $SIF_{PAR}$ , EVI, and GPP averaged within the extent of extreme and medium dry respectively are displayed in Fig. 3-4. Compared with approximately one standard deviation (SD) decline in all

vegetation variables under medium dry, those exhibited 2-3 times SD decrease relative to climatology under extreme situation. Correspondingly, both  $SIF_{PAR}$  and EVI showed largest reduction from January 2019 as a result of persistent rainfall deficit as well as increased temperature ( $2-3^{\circ}C$ ) since November 2018.

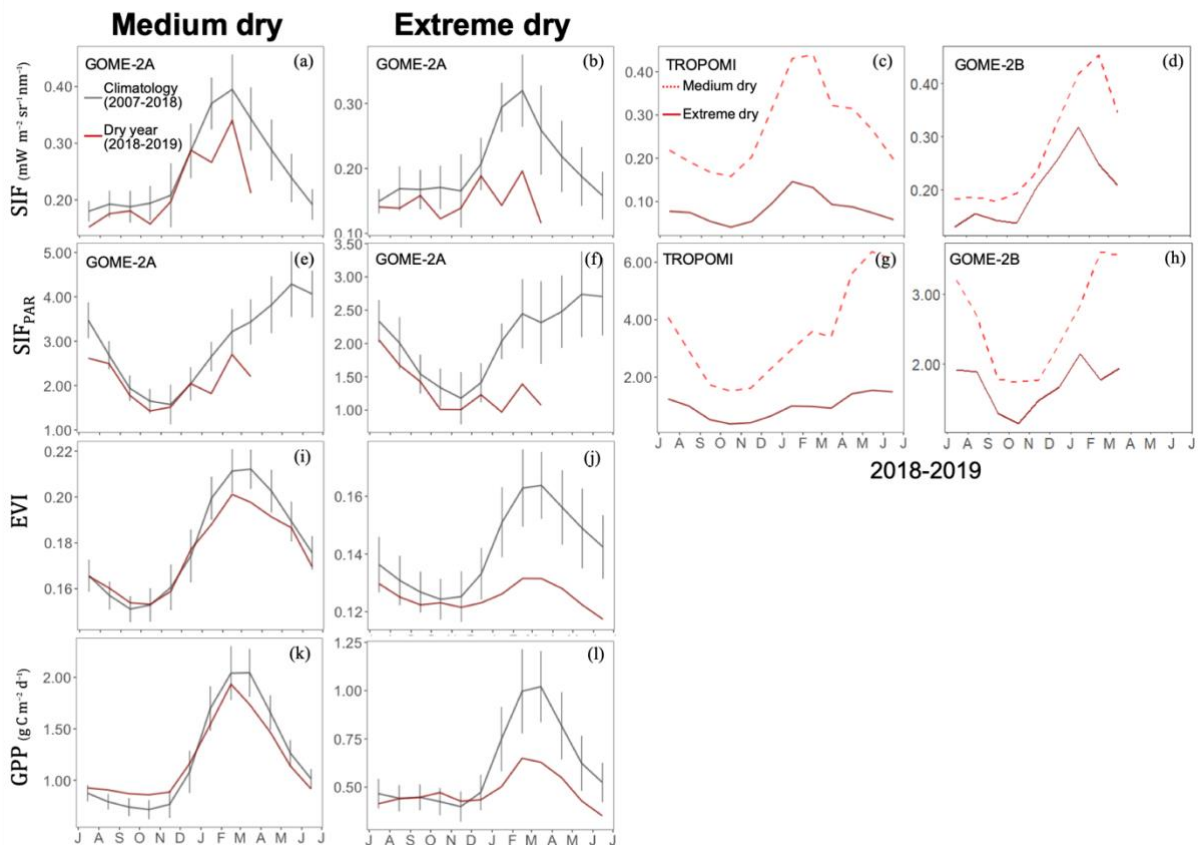


Figure 3-4 The spatially-averaged seasonal cycles of GOME-2A SIF,  $SIF_{PAR}$ , MODIS EVI, and FluxSat GPP within (a, e, i, k) medium and (b, f, j, l) extreme dry extent from July 2018 to June 2019. The grey curves represent the monthly multiyear mean of each variable between 2007 and 2018. Vertical lines refer to  $\pm 1$  standard deviation. (c, d, g, h) the spatially-averaged seasonal profiles of SIF,  $SIF_{PAR}$  from TROPOMI and GOME-2B in 2018-2019 respectively.

The spatial patterns of standardized anomalies of precipitation, surface and root zone soil moisture, LST, SIF,  $SIF_{PAR}$ , EVI, and GPP during 2018-2019 extreme drought are shown in Fig.3-5, along with their pixel density classified by extreme and medium dry. Meteorological data show that 87%, 25% of study

region appeared rainfall anomalies  $< -1$  SD,  $-2$  SD respectively, and 91%, 60% of the area exhibited air temperature anomalies larger than 1 SD and 2 SD, revealing it was a large-scale drought event coupled with an extreme heatwave during 2018-2019 monsoon season. The persistently reduced precipitation along with higher temperature results in depletion of both surface and root zone soil water content over most area, of which 70%, 50% showed less than  $-1$  SD respectively.

Vegetation growth is largely affected by the extreme drought, and the majority of the area showed negative anomalies for all vegetation variables relative to multiyear mean.  $SIF_{PAR}$  and EVI exhibited similar spatial pattern, where those were remarkably negative anomalies ( $< -2$  SD) between  $17^{\circ}$ - $20^{\circ}$ S and  $129^{\circ}$ - $138^{\circ}$ E (Fig. 3-5). SIF and  $SIF_{PAR}$  showed proportional pixels distribution under extreme and medium dry condition, while there was an obviously distinction for EVI. This discrepancy between SIF and EVI was mainly caused by the divergent responses over northern humid northern Australia ( $11^{\circ}$ - $15^{\circ}$ S), where EVI exhibited evidently positive anomalies in comparison to slightly depressed SIF,  $SIF_{PAR}$ .

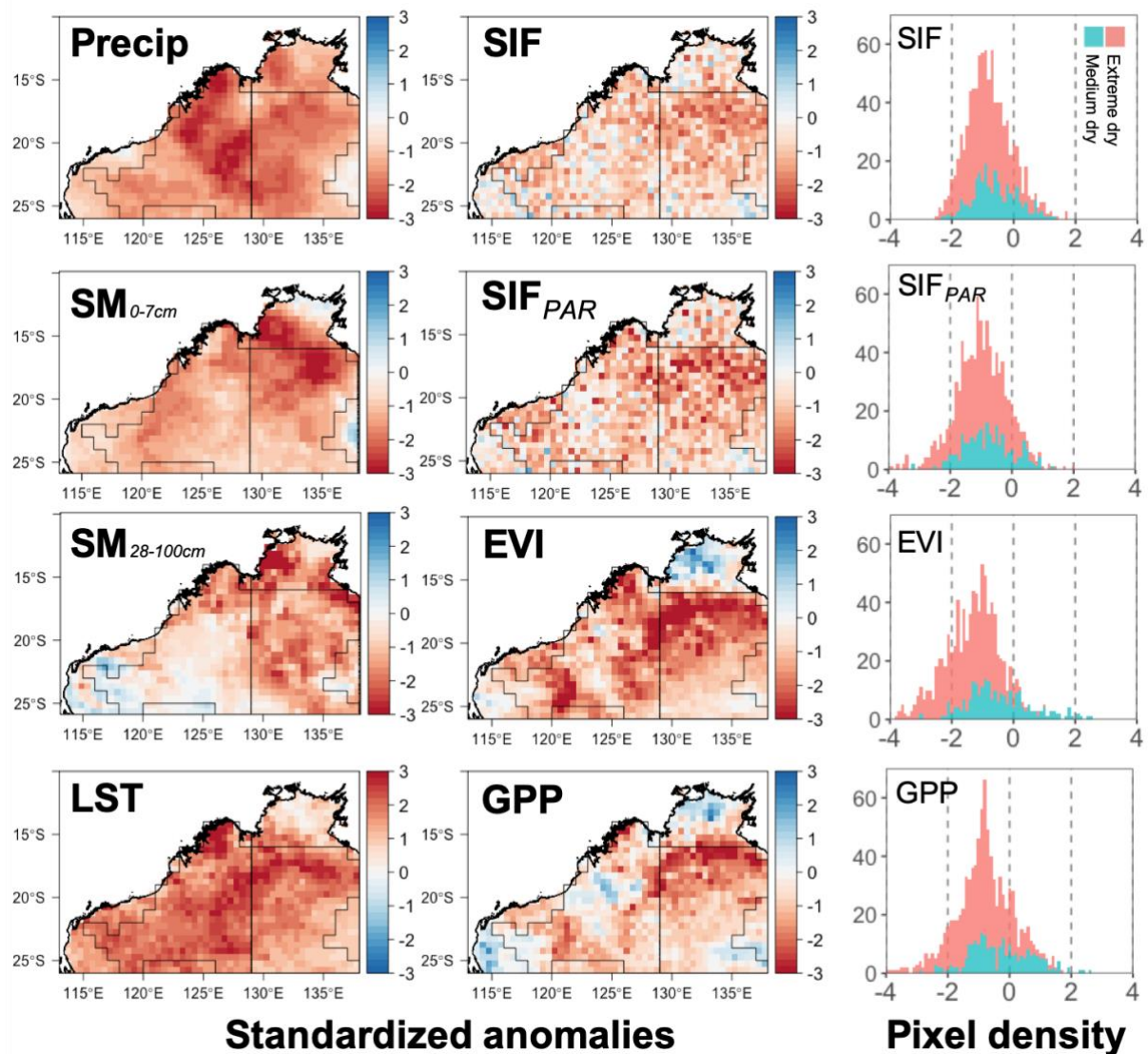


Figure 3-5 The spatial distributions of the standardized anomalies of IMERG precipitation, ERA-5 surface and root zone soil moisture, MODIS LST, GOME-2A SIF, SIF<sub>PAR</sub>, EVI, and FluxSat GPP averaged from November 2018 to March 2019. Pixel density of vegetation variables within the extent of extreme and medium dry respectively are shown in right column.

### 3.3.2 Responses of dryland vegetation to drought at diverse severity and time scales

In order to investigate the response of major biome types of dryland vegetation to different drought severity, four pairs of ROIs were inter- and intra-compared during 2018-2019 extreme drought as well as associated 2012-2013 and 2015-

2016 drought events. Temporal variation in SIF, EVI averaged by four pairs of ROI in 2018-2019 as well as the corresponding ROI-2 in 2012-2013, ROI-4 in 2015-2016 are presented (Fig. 3-6). For humid ROI-1 and arid ROI-3, there was notably difference between extreme and medium region, of which both SIF and EVI showed larger negative anomalies under extreme dry. For semi-arid ROI-2, both vegetation variables exhibited equivalent magnitude of anomalies regardless of drought severity under two contrasting drought events (2018-2019 and 2012-2013). Similarly semi-arid region partially covered with hummock grass (ROI-4), SIF also showed comparably negative anomalies under both extreme and normal dry of 2015-2016 (Fig. 3-6l), while EVI displayed a contrasting response (Fig. 3-6k).

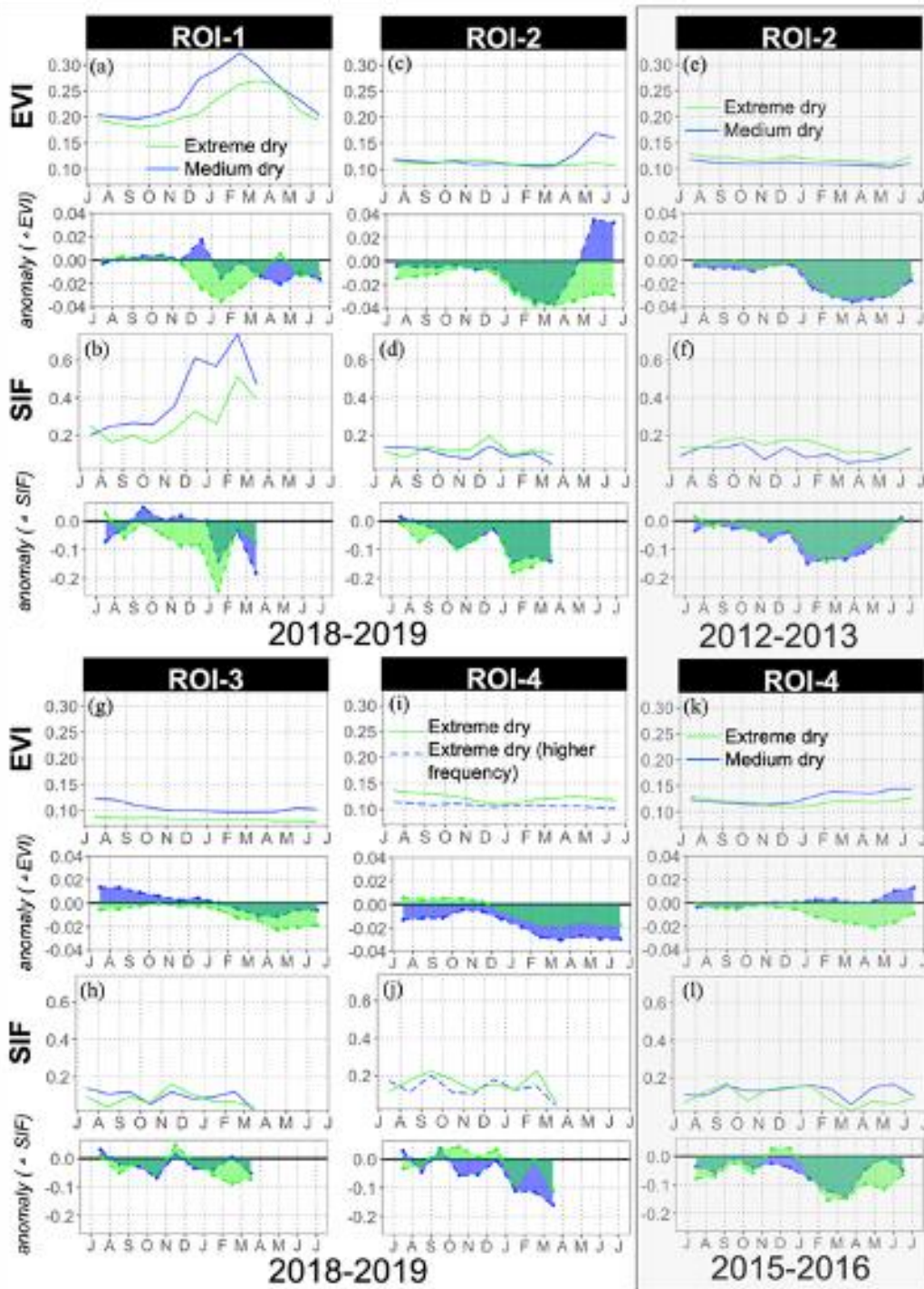


Figure 3-6 Region-wide seasonal cycles and anomalies of (a, c, g, i) EVI and (b, d, h, j) SIF within four pairs of ROIs in 2018-2019. Seasonal profiles of SIF and EVI within (e, f) ROI-2 in 2012-2013 and (k, l) ROI-4 in 2015-2016. Bottom panels of each figure refer to the anomalies of SIF or EVI relative to climatology (2007-2018).

In addition to the drought severity, response of vegetation was also affected by time scales of extreme dry, as evident by ROI-4 in 2018-2019 (Fig 3-6i, 3-6j).

We found both sub-region of ROI-4 were under extreme dry condition but with different lengths of extreme-dry period (Fig. 3-3), that leads to the larger reduction of SIF and EVI under longer periods of extreme dry.

Figure 3-7 presents the anomalies of SIF and EVI for all pixels by diverse extreme-dry months in 2018-2019 monsoon season. Semi-arid ecosystem (AI: 0.3-0.4) showed largest reduction under medium dry or short-lived dry condition for both SIF and EVI. For mesic ecosystem (AI > 0.6), EVI remained positive anomalies even under 1-month extreme dry in contrast to negative anomalies of SIF. On the other hand, both variables capture the comparable reduction of arid or semi-arid vegetation (AI ≤ 0.4) in spite of drought severity or time scales.

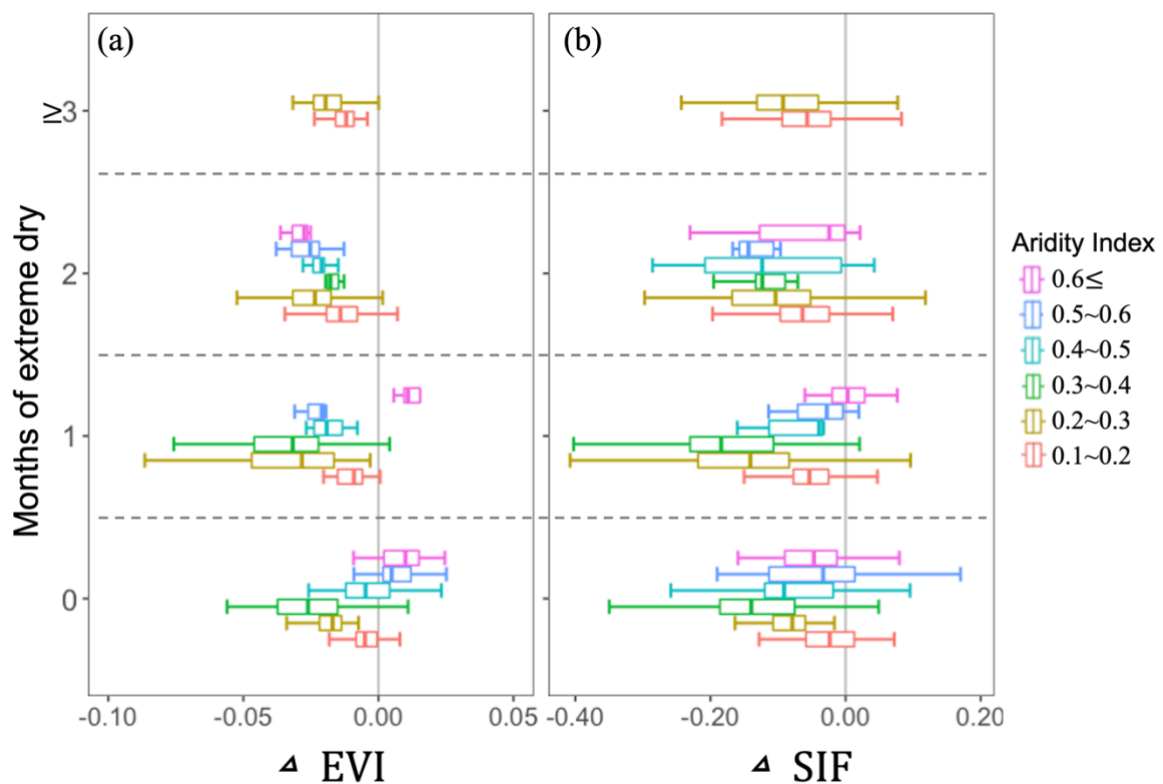


Figure 3-7 The boxplot of anomalies of (a) EVI and (b) SIF by different extreme-dry months along all pixels grouped by aridity index during 2018-2019.

### **3.3.3 Comparison of SIF and EVI in response to extreme drought**

To further explore the difference in response of biome-specific vegetation of SIF and EVI to 2018-2019 extreme drought, anomalies of two variables among entire region under extreme and medium dry are shown in Fig. 3-8. In general, the magnitude of anomalies of SIF and EVI was proportional to the mean SPEI among each category (Fig. 3-8a, 3-8d). Tussock grasslands under the worst dry situation in 2018-2019 also exhibited largest reduction of both SIF and EVI compared with other major biomes. Apart from this, it was also shown largest divergent magnitude of anomalies under extreme and normal dry condition. Likewise, the mesic ecosystems (e.g. woodland, open woodland) exhibited larger difference under two drought level relative to arid and semiarid biomes (e.g. hummock grassland, open shrubland, and scattered shrubs & grasses, Fig. 3-8b, 3-8c). There was an evident trend for EVI with amplified difference between extreme and medium dry from arid to humid climate regimes (Fig. 3-8f), especially for positively anomalous EVI under medium dry ( $AI > 0.5$ ). Conversely, the majority of SIF across different biome type or climate regimes showed negative anomalies in regardless of drought severity (Fig 3-8b, 3-8e).

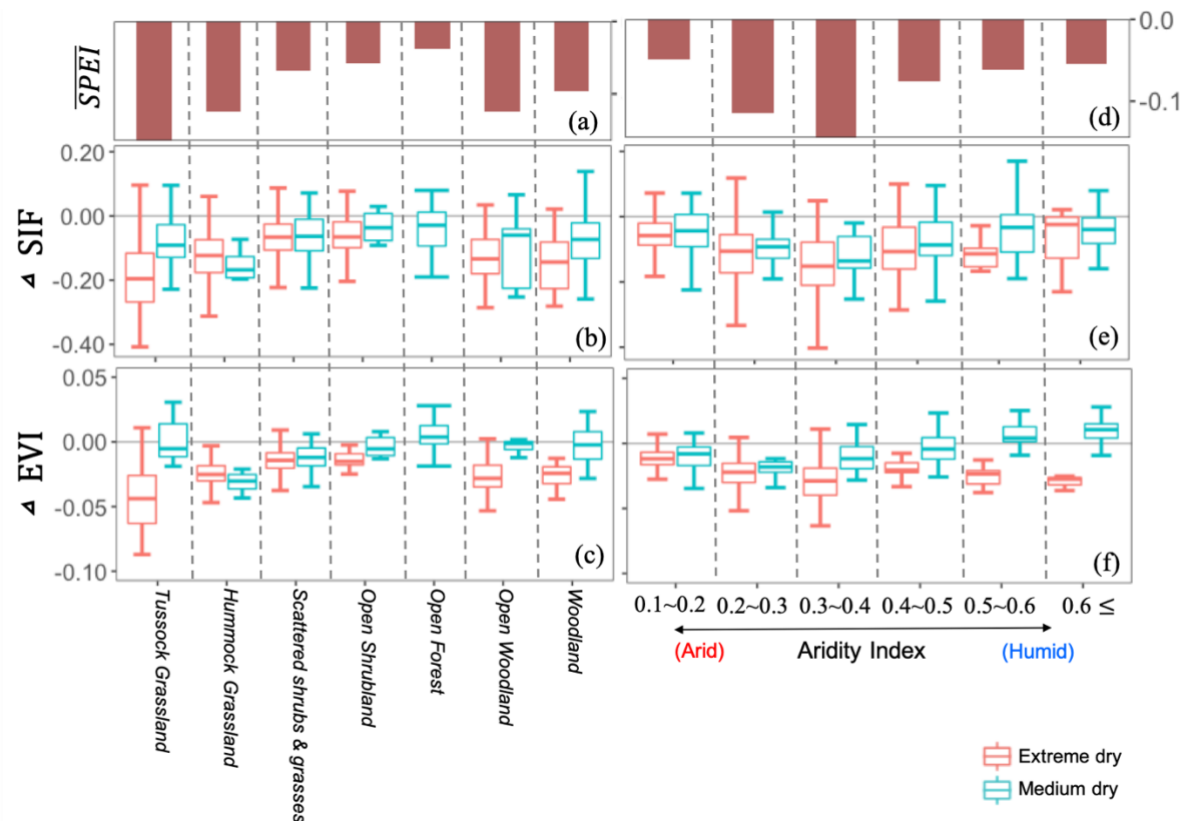


Figure 3-8 The boxplot of anomalies of EVI and SIF under extreme and medium drought along all pixels grouped by major biome types and aridity index during 2018-2019.

Temporal percentage of drought-related vegetation decline indicated by EVI and SIF at monthly and 16-day scale are shown in Fig.3-9. At the beginning of this drought event (November), approximately 38%, 20% of the area was affected by moderate ( $< -0.5\sigma$ ) and severe ( $< -1\sigma$ ) losses respectively indicated by EVI, and increased to over 80%, 50% with the development of extreme drought (Fig. 3-9a). The percentage of moderate and severe reduction observed by SIF/SIF<sub>PAR</sub> in November of 2018 were around 36%, 18%, comparable to those by EVI (Fig. 3-9b, 3-9c). In addition, the percentages of affected area revealed by SIF were slight decrease after reaching the peak in February of 2019, while the impacted region indicated by EVI remained growing.

To further contrast the responses of SIF and EVI at a higher temporal scale, 16-day time series of percentage of moderate/severe/extreme anomalies indicated by EVI and SIF was presented in Fig. 3-9d, 3-9e. There were apparently larger proportion of vegetation decline indicated by EVI than SIF at each category of anomalies, especially over 20% of the area in middle of March (DOY=73) was affected by extreme ( $< -2\sigma$ ) reduction observed by EVI relative to the maximum 7% of that indicated by SIF at the end of February (DOY=57). Besides, the percent of pixels with no seasonality detected by EVI was also higher than that observed by SIF.

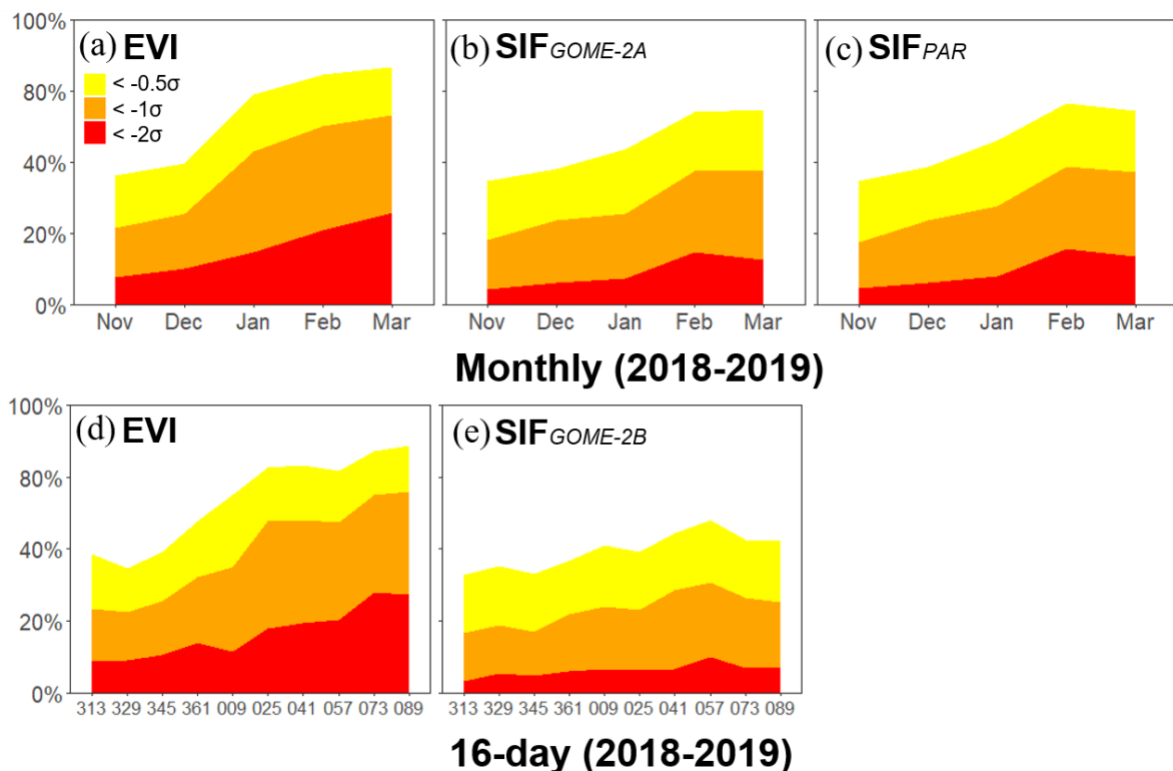


Figure 3-9 (a, b, c) Monthly and (d, e) 16-day time series of the percentage of drought-induced vegetation reduction indicated by EVI, SIF, and SIFPAR under moderately ( $< -0.5\sigma$ ), severely ( $< -1\sigma$ ) and extremely ( $< -2\sigma$ ) negative anomalies.  $\sigma$  indicates the standard deviation of the monthly SIF, EVI during 2007–2018 as well as 16-day SIF/EVI during

2013–2018. The text of x-axis in Fig.9d, 8e refer to the day of year (DOY) from November 2018 to March 2019.

### 3.3.4 Cross-comparison with in-situ measurements

With the purpose of validating satellite-based observation with field measurement, temporal variations in GPP, SIF, EVI over 5 selected flux tower sites in 2018-2019 are shown in Fig. 3-10. For two northern mesic sites (AU-How, AU-Dry) under medium dry condition, both tower-based GPP and satellite-based SIF, EVI exhibited comparable amplitude of seasonal cycle in 2018-2019 relative to that of climatology (Fig. 3-10a-h). Conversely for three southern sites (AU-Stp, AU-ASM, AU-TTE) suffered extremely dry in 2018-2019, there were large reduction and barely seasonal amplitude detected by neither in-situ measurement nor satellite observation (Fig. 3-10i ~ 3-10t).

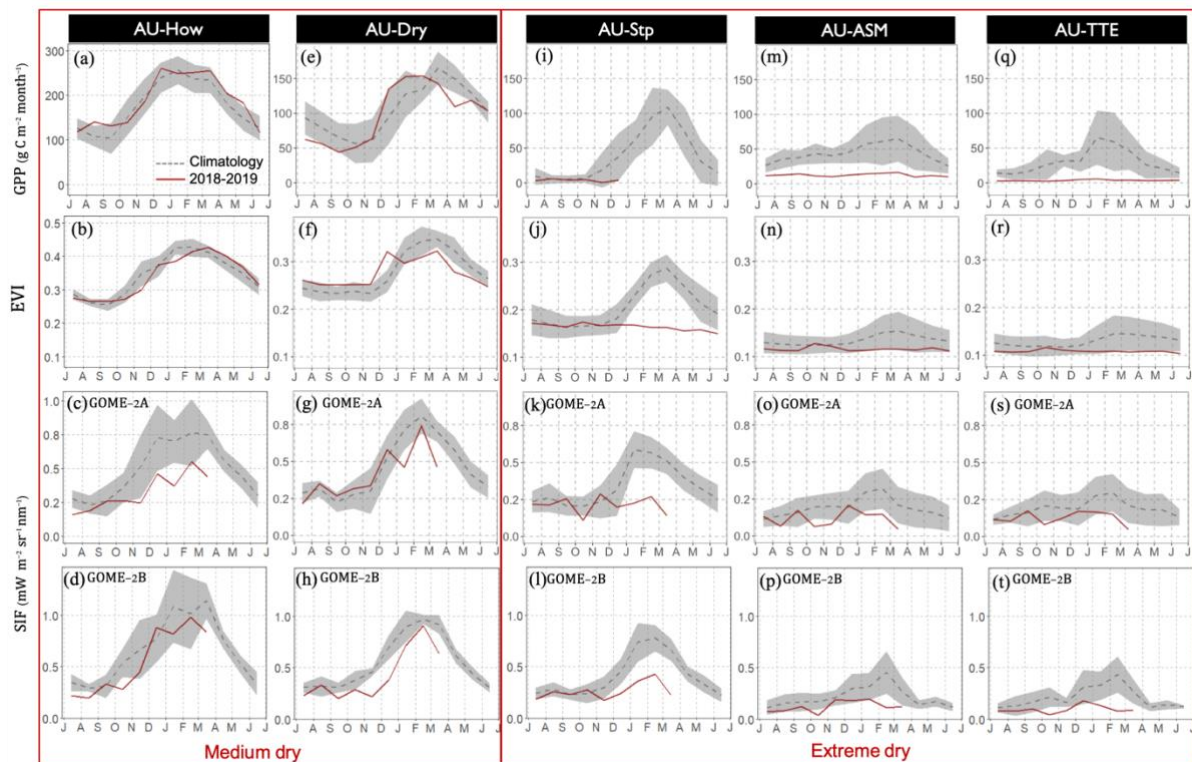


Figure 3-10 Seasonal cycles of monthly tower-based GPP, satellite-observed SIF, EVI over five flux tower sites from July 2018 to June 2019 as well as multiyear mean. The grey area refers to  $\pm 1$  standard deviation.

Figure 3-11 presents the relationship between tower-based GPP and satellite-based vegetation variables (SIF, EVI) in 2018-2019 across five selected sites at different spatial and temporal resolution. In spite of diverse spatiotemporal resolution, both satellite-observed SIF, EVI were overall significantly ( $p < 0.001$ ) associated with in-situ measurement GPP ( $r^2$  ranging from 0.65 to 0.94) in the extreme dry year of 2018-2019. In particular, there was an enhanced correspondence between GPP and SIF with increasing spatial resolution (from  $0.5^\circ$  to  $0.05^\circ$  grid) for both monthly and 16-day temporal scale (Fig. 3-11a, 3-11b, 3-11e, 3-11f). Besides, we found stronger relationship between field measurement and satellite-based observation at monthly series ( $r^2 = 0.77, 0.94$ ) relative to 16-day series ( $r^2 = 0.65, 0.88$ ). The close correlation between GPP and EVI remained across different spatial and temporal resolution ( $r^2$  ranging from 0.86 to 0.91, Fig. 3-11c, 3-11d, 3-11g, 3-11h).

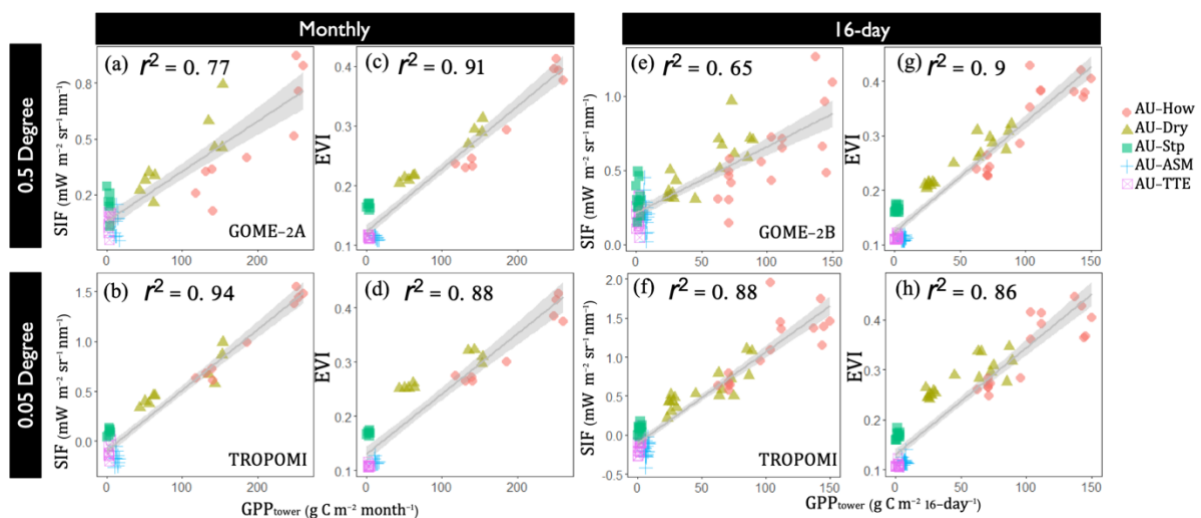


Figure 3-11 Relationship between tower-based GPP and satellite-based SIF, EVI in 2018-2019 across five flux tower sites at different spatial (0.5°, 0.05° grid) and temporal (monthly, 16-day) resolution. ( $p$  value < 0.001)

### **3.4 Discussion**

#### **3.4.1 Potential of space-borne SIF for drought monitoring over water-limited ecosystems**

Satellite-based SIF observations capture the spatial and temporal variations in dryland vegetation under 2018-2019 extreme drought in Australia (Fig. 3-4, 3-5). Relative to EVI and GPP, the fluctuated SIF series and notable spatial speckling were probably owing to its high retrieval noise in sparsely vegetated regions (Geruo et al., 2017), especially for lower signal level under extreme drought. Overall, SIF and EVI exhibited resembling spatial and temporal responses of dryland vegetation to this extreme event, wherein the central study area (between 17-20°S and 129-138°E) showed most remarkable reduction (Fig. 3-5). The primary difference in spatial dynamics of two variables occurred over northern humid region (between 12-15°S and 129-138°E) under medium drought, where SIF showed marginally negative anomalies in comparison to positive anomalous EVI (Fig. 3-5). This is consistent with previous studies (Walther et al. 2016; Wang, Qiu, et al. 2019; Yang et al. 2018; Zhang et al. 2019), revealing that there was a considerable decoupling of photosynthesis and greenness dynamics under moderate dry condition over mesic ecosystems (e.g. forests, and woodlands).

Nonetheless, there was concurrently substantial loss in both SIF and EVI over arid and semiarid biome types, those suffered from extreme rainfall deficit as well as severe heat wave (Fig. 3-5). In particular, higher percentage of the area indicated by EVI was affected by extreme ( $< -2\sigma$ ) losses than that by SIF throughout the entire 2018-2019 monsoons season (Fig. 3-5, Fig. 3-9). This finding was against with a similar study (Qiu et al. 2020), that concludes satellite SIF observations are more sensitive to water and heat stress than EVI over arid central Australia in the 2019 heatwave. However, the divergent results were primarily ascribed to the different methods to define the anomaly, that they utilised the relative anomaly (a departure from the climatology and divided by the multiyear mean) instead of standardized anomaly used in this study. The larger variation in magnitude of SIF than that of greenness-based VIs gave rise to the sharper reduction in SIF indicated by relative anomaly relative to EVI. In addition, insufficient baseline years (2015-2018) in their study may induce more uncertainties as a consequence of highly dynamic climate regime over inland Australia.

On the contrary, we contrasted the responses of two source of SIF data derived from GOME-2A and GOME-2B with MODIS EVI under two reference climatologies (2007-2018 and 2014-2018) respectively. We found that the percentage of the drought-affected area captured by EVI was consistently higher than that by SIF regardless of different sensors and diverse temporal scales (Fig.

3-9). The reason causing the more significantly negative standardized anomalies of EVI relative to those of SIF was possibly owing to the fact that the dramatically drought-induced reduction in vegetation leads to barely increased magnitude of seasonal cycles over the vast of inland area (Fig. 3-11). Apart from this, high-retrieval noise provokes the larger variability of SIF signal over arid/semiarid ecosystems.

Compared with coarse SIF data derived from GOME-2, the state-of-the-art TROPOMI SIF observation with substantially improved spatiotemporal resolution shows an enhanced correlation with tower-based GPP in the extremely dry year of 2018-2019 (Fig. 3-11), implying this advanced dataset has promising potential for drought monitoring over heterogeneous arid and semiarid ecosystems. As opposed to the fluctuated temporal series and spatial speckling of GOME-2 SIF signal (Fig.3-4, Fig.3-5, Fig.3-6, Fig.3-11), SIF retrieved from remarkable radiometric performance of TROPOMI exhibit more spatial and temporal consistency, representing a step change in SIF remote sensing capabilities (Köhler et al. 2018; Wang et al. 2020). It is worth noting that abundant of negative values of TROPOMI SIF was observed over central Australia in 2018-2019 (AU-ASM, AU-TTE, Fig.3-10), probably owing to the retrieval noise. Köhler et al. (2018) suggested negative SIF values mainly occur for single TROPOMI measurements, which should not be over-interpreted. A

comprehensive assessment of capability of the newly dataset over dryland ecosystem needs to be conducted in future.

### **3.4.2 Dynamics of dryland vegetation under different drought scenarios**

Varying responses of major biome types of dryland vegetation to different drought severity (extreme dry vs medium dry) were observed (Fig. 3-6, Fig. 3-8b, 3-8c). We found enhanced magnitude of reduction of both SIF and EVI in conjunction with increasing drought severity over humid/sub-humid biomes (e.g. forest, woodland, and tussock grasslands). In northern tropical ecosystems, higher soil water storage resulting from large amounts of precipitation along with larger water holding capacity contribute to higher resilience against water deficit under drought stress (Ma et al. 2013). Therefore, we found that EVI of humid vegetation (forest, open forest, and woodland) remained positive anomalies under medium dry condition (Fig. 3-8c), and SIF of those showed slightly negative anomalies (Fig. 3-8b). By contrast, the two vegetation variables (SIF and EVI) of arid/semiarid vegetation (e.g. hummock grasslands, open shrublands) showed comparable losses under extreme and moderate dry condition, indicating the largest sensitivity and vulnerability of semiarid ecosystems to the hydroclimatic variations (Felton, Zavislan-Pullaro & Smith 2019; Ma et al. 2015). It is not only as evident by the 2018-2019 extreme drought, but also 2012-2013, 2015-2016 drought event in central Australia (Fig. 3-6e, 3-6f, 3-6k, 3-6l). Given that soil organic content in Australia's water-

limited areas is lower than that in costal humid regions (Ma et al. 2013), arid/semiarid vegetation in the interior of Australia has a relatively lower water holding capacity against water and heat stress even under medium dry condition. As prolonged drought is projected to increase both frequently and intensely (Huang et al. 2016; Min et al. 2011), drylands will act as a more critical role in regulating global carbon and water cycle (Ahlström et al. 2015; Poulter et al. 2014).

Given that the coarse spatial grid ( $0.5^\circ$ ) induced uncertainty of biome-specific analysis over heterogeneous drylands, re-grouped pixels based on aridity index were used to investigate the responses to the extreme drought at different time scales (Fig.3-7). As opposed to notably depressed SIF over mesic ecosystem ( $AI > 0.6$ ), EVI remained positive anomalies even under one-month extreme dry, in line with reported studies concerning dry-season greening of forests (Morton et al. 2014; Saleska et al. 2016). Despite that, canopy greenness of humid ecosystem exhibited significant reduction when the extreme-dry period exceeded one month ( $\geq 2$ ). Likewise, we found larger magnitude of decline in arid region ( $AI < 0.3$ ) resulting from the increasing extreme-dry months although both sub-regions of ROI-4 suffered from extreme dry in 2018-2019 (Fig.3-3, Fig. 3-6, Fig.3-7). In contrast, both SIF and EVI in semiarid region ( $AI: 0.3-0.4$ ) exhibited largest reduction under short time-scales (extreme-dry

month  $\leq 1$ ), confirming semiarid biomes are the most susceptible to extreme drought.

### **3.5 Conclusions**

In summary, we investigated the spatial and temporal responses of SIF and EVI of dryland vegetation to 2018-2019 extreme drought over Australia using multi-source satellite-based SIF observations. We found that space-borne SIF has capability of characterizing the spatiotemporal dynamics of drought over water-limited ecosystems despite of high retrieval noises. The unprecedented SIF derived from TROPOMI shows remarkably enhanced agreement with tower-based GPP in the dry year of 2018-2019, demonstrating the great potential of the advanced dataset to track the dynamics of dryland vegetation under future changing climates. In addition, semiarid ecosystems exhibiting largest reduction regardless of drought severity and time scales are the most sensitive to climatic extremes.

## **Chapter 4 Spatiotemporal variations of dryland vegetation phenology revealed by satellite-observed fluorescence and greenness across the North Australian Tropical Transect**

### **Abstract**

Accurate characterization of spatial patterns and temporal variations in vegetation is of great importance for improving our understandings of terrestrial ecosystem functioning under changing climates. Owing to the highly variable climate as well as heterogeneous composition of vegetation types, understanding the phenology dynamics of Australia's dryland vegetation remains challenging. Here, we explored the spatiotemporal variability of dryland vegetation phenology using satellite-observed Solar-Induced chlorophyll Fluorescence (SIF), Enhanced Vegetation Index (EVI), as well as eddy covariance measurement of vegetation productivity (GPP) along the North Australian Tropical Transect. Substantial impacts of extreme drought and intense wet on phenology and function of dryland vegetation are indicated by both SIF and EVI, especially in arid/semiarid interior of Australia without detectable seasonality in the dry year of 2018-2019. Besides, greenness-based phenological metrics over southern arid/semiarid region, such as Hummock grasslands and shrublands, exhibit a considerable delayed senescence as compared with SIF and tower-based GPP in the wet year. By contrast, EVI could more accurately capture the seasonal and interannual variation in

vegetation production than SIF over northern mesic woodlands and forest ( $r^2 = 0.86$ ). In spite of high retrieval noises, spaceborne SIF observations, offsetting the drawbacks of greenness-based phenology products with potentially lags of end of season, have the capability of mapping and characterizing spatiotemporal dynamics of dryland vegetation phenology.

## **Keywords**

SIF, EVI, Phenology, NATT

## **4.1 Introduction**

Vegetation phenology, the study of the periodic biological life cycle events of plants, is a critical regulator of carbon and water cycling in terrestrial ecosystems (Peng et al. 2018). The trend of global warming has aroused great interests in understanding and monitoring the dynamics of vegetation phenology under the changing climate (Piao et al. 2019). As a valuable indicator of climate variability and ecosystem responses (Peng et al. 2018), accurate measurements of land surface phenology (LSP) are crucial for better explaining the land-atmosphere-energy exchange and its representation in terrestrial biosphere models (Ma et al. 2013; Zhang et al. 2018).

Phenological studies are usually conducted at the species- or ecosystem-level through ground-based field techniques (Ma et al. 2013), such as visual inspection, eddy covariance flux towers, near-surface spectral radiometer and

digital cameras (Verger et al. 2016). Satellite-based observations, providing unique and feasible ways for examining broader scale phenomena (Ma et al. 2013), have notably expanded the horizon of traditional phenology observations (Piao et al. 2019). Vegetation indices, which are combinations of surface reflectance at two or more wavelengths designed to highlight a particular property of vegetation (Huete et al. 2002), can depict spatiotemporal patterns of the timing of plant growth, senescence, and dormancy at seasonal and inter-annual time scales (Broich et al. 2018). The enhanced vegetation index (Huete et al. 2002), normalized difference vegetation index (Tucker 1979) , and leaf area index (LAI) (Watson, 1947) derived from optical satellite sensors are widely applied for tracking large-scale vegetation seasonality.

Dryland vegetation, covering approximately 40% of the global land surface (Reynolds et al. 2007), is exceedingly susceptible to climate conditions, mainly owing to the chronic physiological stress (Walker, De Beurs & Wynne 2014). Numerous phenology studies based on satellite remote sensing are examined over temperature-driven ecosystems of northern hemisphere (Ma et al. 2013), however, the phenological dynamics of dryland vegetation under climate variability and extreme events have not been thoroughly investigated as a result of the intrinsic sensitivity and complexity (Walker, De Beurs & Wynne 2014). Given the mixed and heterogeneous arrangement of water-limited ecosystems confounds the extraction of phenological transition, Walker, De Beurs &

Wynne (2014) assessed dryland vegetation phenology across an elevation gradient in Arizona, USA through fusing synthetic MODIS and Landsat imagery. The significant spatiotemporal variations in savanna biomes with diverse tree-grass ratios implies that grass-containing xeric savanna is especially sensitive and vulnerable to hydro-climatic variability (Ma et al. 2020). Besides, previous studies found that growing season retrieved from greenness-based approach overestimates the photosynthetically-active duration, indicating a divergence between greenness and photosynthesis (Jeong et al. 2017; Joiner et al. 2014). On the basis of the complex composition of plant functional types as well as highly dynamic climate in Australia, accurately assessing the phenological characteristics of dryland vegetation still remains challenging (Wang et al., 2019).

In contrast to the reflectance-based approaches, SIF signal directly emitted from the core of photosynthetic machinery present a fresh manner of remotely sensing vegetation growth and response (Sun et al., 2017). Recent studies found that satellite-based observations of SIF can detect interannual and seasonal variations in gross primary production of vegetation in North America (Yang et al. 2015; Zhang et al. 2016; Zuromski et al. 2018). Wu et al. (2018) found strong spatiotemporal consistency between satellite-based SIF and GPP products across the contiguous United States. Although photosynthesis and greenness exhibit an analogous seasonality in deciduous forests, satellite

chlorophyll fluorescence measurements reveal large-scale decoupling of photosynthesis and greenness dynamics in boreal evergreen forests (Chang et al. 2019; Walther et al. 2016). Continuous observations of both SIF and vegetation indices contribute to the understanding of the differences between, and information carried by, seasonal variations vegetation structure and greenness and physiology (Jeong et al. 2017).

By comparing with EVI and photochemical reflectivity index, Smith et al. (2018) demonstrated that chlorophyll fluorescence derived from GOME-2 more accurately captures seasonal and interannual variations of gross primary productivity across dryland ecosystems of southwestern North America. Through evaluating the SIF time series derived from GOME-2 with tower-based GPP in Australia, Sanders et al. (2016) found natural biome types, such as savanna and open woodland, showed weaker correlations relative to agricultural biomes. Taking into account sparsely spatial resolution of existing spaceborne SIF product as well as the varying mixtures of trees, shrubs, and grasses in Australia's dryland ecosystems, a high-resolution contiguous SIF product ( $SIF_{oco2\_005}$ ) was utilized to explore the phenology dynamics of dryland vegetation along the North Australian Tropical Transect (Wang, Beringer, et al. 2019). They found this up-scaled SIF data at  $0.05^\circ$  spatial resolution outperformed EVI for characterizing seasonal onset and senescence of dryland vegetation, and suggested it had potential for large-scale mapping of phenology

dynamics as opposed to traditional reflectance-based vegetation indices. Nevertheless,  $SIF_{oco2\_005}$  was generated by OCO-2 native SIF along with MODIS reflectance using machine learning (Yu et al. 2019), and it therefore showed an enhanced accuracy of determining the phenological transition of GPP derived from flux tower measurement as a consequence of its containing both the structural and physiological information. However, whether the original SIF observation can accurately capture the phenology dynamics of Australia's dryland vegetation under climate variability remains unclear.

In arid and semiarid ecosystems, rainfall strongly affects the strength and occurrence of photosynthetic and respiratory activities and is the dominant driver for vegetation phenology and productivity (Cleverly et al. 2013).

Seasonality of Acacia-dominated woodlands (as measured by EVI) was found to show a substantial responsiveness to hydroclimatic variability (Ma et al. 2013). Additionally, approximately 80% of the variations in the length of growing season of major dryland biomes along the NATT could be attributed to the variability of annual precipitation (Ma et al. 2013). Nevertheless, there is a knowledge gap regarding how and to what extent do major environmental and climatic drivers determine the phenological dynamic of fluorescence (as a surrogate of photosynthesis).

The objectives of this study were: (1) to evaluate the spatial patterns and seasonal variations of dryland vegetation phenology derived from SIF and EVI;

(2) to determine the phenology dynamics of major plant function types, C<sub>3</sub>-dominated woodlands/shrublands (Mulga, Eucalypt) and C<sub>4</sub>-dominated grasslands (Hummock, Tussock); (3) to assess the interaction of environmental drivers and vegetation function types on photosynthetic dynamics.

## 4.2 Materials and Methods

### 4.2.1 Study area

This study was conducted at a regional scale between 12°S to 23°S and 128°E to 138°E, which is known as the Northern Australian Tropical Transect (NATT) (Figure 4-1). This region, particularly for northern NATT, has a classic monsoon climate pattern, which receives more than 80% of annual precipitation during November to April (Ma et al. 2013). From northern mesic tropics to the xeric central Australia, mean annual rainfall ranges from 1700 mm to approximately 300 mm (Ma et al. 2013).

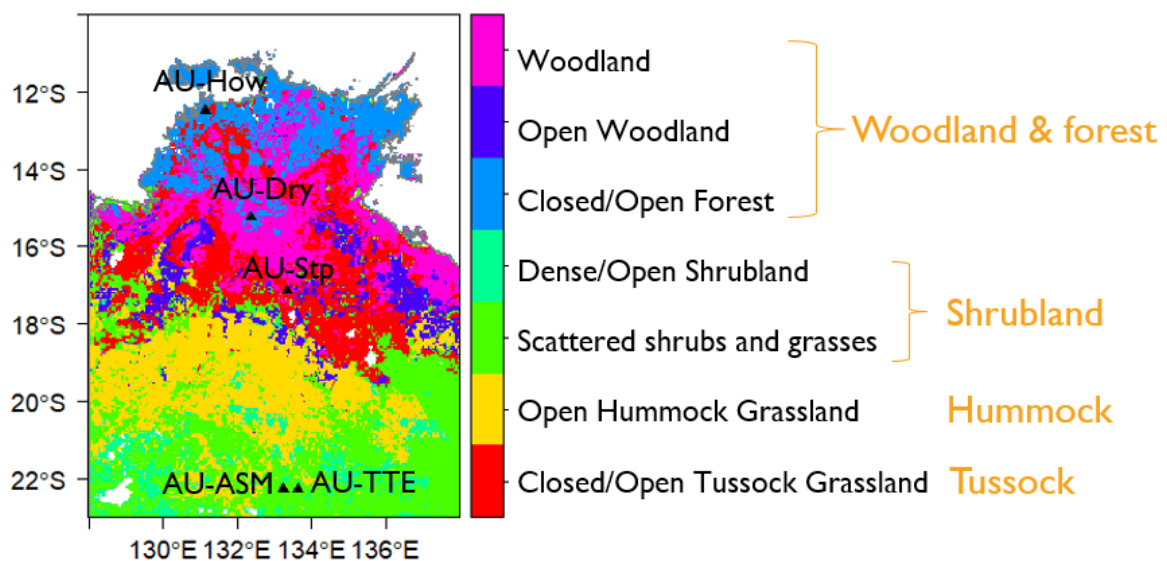


Figure 4-1 Land cover map of the Northern Australian Tropical Transect (NATT) study area. Black triangles refer to the five flux tower sites.

Correspondingly, the vegetation follows a wet-dry gradient that shifts from Eucalyptus dominated forests, open forests, and woodlands in the coastal northern areas to Acacia-dominated open woodlands, scattered shrubs, and hummock grassland into the vast inland (Ma et al. 2013). More detailed description with respect to ecosystems, climate, and soils of the entire study region can be found in Ma et al. (2013) and Hutley et al. (2011).

To contrast satellite observation with ground-based evidence, we selected five representative flux tower sites across the extensive study area: Howard Springs (AU-How [131.15°E, 12.495°S]), Dry River (AU-Dry [132.371°E, 15.259°S]), Sturt Plains (AU-Stp [133.3502°E, 17.1507°S]), Alice Springs Mulga (AU-ASM, [133.2493°E, 22.2828°S]), and Ti Tree East (AU-TTE [133.64°E, 22.287°S]) (Beringer et al. 2016). The major vegetation types over five sites respectively are Eucalypt woodland (AU-How), Eucalypt open forest (AU-Dry), Tussock grassland (AU-Stp), Mulga open woodland (AU-ASM), and Corymbia savanna (AU-TTE).

#### **4.2.2 Satellite data**

In this study, we utilised satellite-based SIF records obtained from Global Ozone Monitoring Experiment-2 (GOME-2) on board EUMETSAT's MetOp-A as well as MetOp-B platform (indicated as GOME-2A and GOME-2B respectively). The GOME-2 instrument is a nadir-scanning spectrometer, which

measures at around 9:30 local equator crossing time, and it have a relatively large footprint (approximately 40 km x 80 km at nadir before 15 July 2013 and 40 km x 40 km since 15 July 2013). GOME-2 comprises four main optical channels with the spectral range from 240 to 790 nm, and the fourth channel ranges between 590 and 790 nm with a spectral resolution of approximately 0.5 nm and a relatively high signal-to-noise ratio (Joiner et al., 2013; Song et al., 2018a). This dataset is primarily retrieved from the filling-in of solar Fraunhofer lines in the vicinity of the 740 nm far-red fluorescence emission peak, based on a simplified radiative transfer model in the company of a principal component analysis in order to disentangle the fluorescence signals from atmospheric absorption, surface reflectance (Joiner et al. 2013; Köhler, Guanter & Joiner 2015). GOME-2 SIF records with a limited amount of validation provide substantially enhanced sampling and precision relative to the filling-in signal at 758 nm from Japanese Greenhouse gases Observing SATellite (GOSAT) TANSO-FTS instrument (Joiner et al., 2013). This dataset is retrieval of the far-red chlorophyll fluorescence peaking at 740 nm, based on a simplified radiative transfer model in the company of a principal component analysis (Joiner et al. 2014). Monthly global coverage of SIF data at  $0.5^{\circ} \times 0.5^{\circ}$  spatial resolution (level 3, Version 28) from February 2007 to March 2019 was obtained from NASA Goddard Space Flight Centre (<https://avdc.gsfc.nasa.gov/>). Given the degradation of GOME-2A instrument during its life time, SIF data observed from MetOp-B platform was also downloaded, that spans from March 2013 to

March 2019. The daily orbital data (level 2, Version) was also used to aggregate 16-day interval records for higher temporal-resolution analysis.

We used Moderate Resolution Imaging Spectroradiometer (MODIS on board Aqua, Collection 6) MYD13C1 (0.05°, 16-day) and MYD13C2 (0.05°, monthly) Vegetation Indices products from January 2007 to June 2019 downloaded from NASA Earth Observation data (<https://search.earthdata.nasa.gov/search>). EVI is an optimized version of vegetation indices that effectively reduces soil background influences and is widely used as a proxy of canopy greenness. To reduce noise and uncertainties, only best quality data was remained in this study through removing pixels of which quality control flag of the first 2 bits neither 00 nor 01, and pixel-wise EVI time series data was smoothed using Savitzky-Golay filter.

MODIS daytime Land Surface Temperature (LST, MYD11C3) at monthly scale and 0.05° spatial resolution was included in this study, collected from NASA Earth Observation data (<https://search.earthdata.nasa.gov/search>). Similarly, bad quality data was removed through eliminating pixels with quality control flag.

To examine the impact of solar radiation on vegetation seasonality, monthly Photosynthetic Active Radiation (PAR) at 1° spatial resolution was downloaded from the NASA Langley Research Centre, Cloud and Earth's Radiant Energy System (CERES, Ed4.1), including adjusted surface PAR both direct and diffuse fluxes under all sky conditions. The total PAR was computed as the sum

of both direct and diffuse PAR (Wang, Qiu, et al. 2019). As recent studies suggested EVI outperformed the MODIS fPAR (fraction of absorbed PAR) products in estimating APAR (Lu et al. 2018), we referred to  $EVI \times PAR$  as an alternative estimate of APAR:

$$APAR \approx EVI \times PAR \quad (12)$$

### 4.2.3 Climate Data and Land cover map

To assess the interaction of environmental drivers and vegetation, monthly air temperature (at 2-meter height) and soil moisture content (surface 0-7cm depth, root zone 28-100 cm depth) based on ERA-5 reanalysis data were downloaded from Copernicus Climate Change Service (<https://cds.climate.copernicus.eu/>).

Global monthly precipitation based on Integrated Multi-Satellite Retrievals for Global Precipitation Measurement (IMERG, Version 6, Final run, 2007-2019) at monthly scale and  $0.1^\circ$  spatial resolution was collected from NASA Precipitation Processing System (<https://pps.gsfc.nasa.gov/>).

National Dynamic Land Cover Dataset (DLCD) was used in this research, obtained from Geoscience Australia and Bureau of Agricultural and Resource Economics and Sciences (<http://www.ga.gov.au/scientific-topics/earth-obs/landcover>). Given that some biome types were only covered by a few pixels over the study region, Closed tussock grassland, Dense shrubland, and Closed forest was respectively re-grouped into Open/closed tussock grassland, Dense

/open shrubland, and Closed/open forest (Figure 4-1). This dataset validated with abundant field sites was aggregated to 0.5° spatial resolution by most frequent values.

#### **4.2.4 Eddy Covariance data**

The original level 3 (AU-How, AU-Dry, AU-Stp) and level 6 (AU-ASM, AU-TTE) flux data provided by the OzFlux network (<http://www.ozflux.org.au/>) were used to pre-process, including quality control assessment, removal of outliers, and gap-filling (Cleverly et al. 2013). Flux partitioning for level 3 data was conducted in open source R scientific computation environment (Version 3.5.1) associated with REddyProc package (Version 1.2). The half hour flux data were aggregated into monthly and 16-day GPP to match with satellite-based observations. For the purpose of comparing with in-situ measurement, satellite observations were extracted within a 3×3 (pixels) window centered at each flux tower site. In order to reduce uncertainties of mismatch footprints between satellite observations and flux tower measurements, satellite-based datasets are extracted at the original spatial resolutions (MODIS EVI: 0.05°; GOME-2 SIF: 0.5°).

#### **4.2.5 Phenological metrics**

Owing to the fact that Ma et al. (2013) demonstrated the capability of the Singular Spectrum Analysis (SSA) for the analysis of nonlinear dynamics in

NATT, we also employed the same method to smooth and reduce the noise in satellite-based SIF, EVI time series. Correspondingly following with (Ma et al. 2013), 37 composite periods of the window length and four leading components were selected to configure the parameters in SSA implementation. After interpolating to daily time series from SSA re-constructed SIF, EVI series, we used PhenoDeriv function from ‘GreenBrown’ package to derive the key phenological metrics. Five metrics were extracted (Figure 4-2):

- The start of growing season (SOS), defined as the date halfway between the minimum value and the fastest greening rate;
- The peak of growing season (POS), the date of the maximum value;
- The end of growing season (EOS), the date halfway between the fastest brown-down rate and minimum value;
- The rate of spring green-up (RSP), the amplitude of EVI or SIF between POS and SOS divided by the periods (days) between POS and SOS;
- The rate of autumn senescence (RAU), the amplitude of EVI or SIF between POS and EOS divided by the periods (days) between POS and EOS.

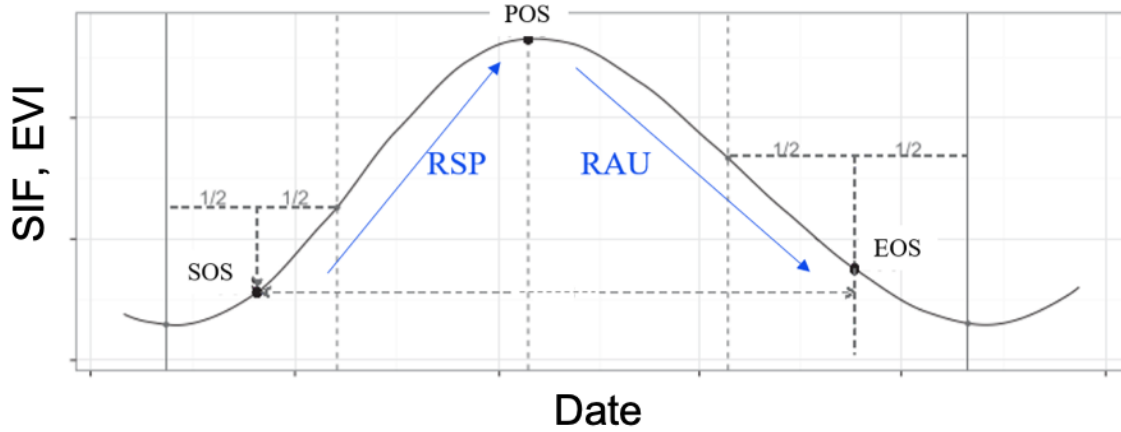


Figure 4-2 Schematic diagram of phenological metrics retrieval. The curve refers to the seasonal SSA re-reconstructed EVI or SIF profile at daily scale. SOS: the start of growing season; POS: the peak of growing season; EOS: the end of growing season; RSP: the rate of spring green-up; RAU: the rate of autumn senescence.

To examine the interaction of environmental drivers and vegetation variables, the coefficient of determination ( $r^2$ ) was calculated across four major biome types. A  $t$  test was utilized to examine the statistical significant level of the relationships ( $p$ -value). To further explore the difference between SIF and EVI, we interpreted SIF with fPAR and  $SIF_{yield}$  (Shen et al., 2020; Song et al., 2018b; Sun et al., 2015), expressed as:

$$SIF_{PAR} = \frac{SIF}{PAR} \quad (13)$$

$$SIF_{yield} = \frac{SIF}{EVI \times PAR} \quad (14)$$

Where  $SIF_{PAR}$  refers to PAR (unit:  $W\ m^{-2}$ ) normalized SIF (unit:  $W\ m^{-2}\ nm^{-1}\ sr^{-1}$ ),  $SIF_{yield}$  refer to APAR normalized SIF, which is the product of the actual fluorescence yield of the canopy and the fractional amount of fluorescence that

escapes from the top of canopy. Data processing, analysis, and visualization were conducted in open source R scientific computation environment (Version 3.6.2) and associated packages contributed by the R user community (<http://cran.r-project.org>).

## **4.3 Results**

### **4.3.1 Seasonal and inter-annual variations over local sites**

Figure 4-3 shows the inter-annual variations in tower-based GPP and satellite-based SIF, EVI over 5 selected flux sites during 2014-2019. Generally, both satellite variables, especially EVI, exhibited the capacity for capturing the seasonal and inter-annual dynamics of dryland vegetation as indicated by tower-based GPP ( $r^2$  ranging from 0.47 to 0.86). Compared with northern mesic sites, the two southern semi-arid sites (AU-ASM, AU-TTE) displayed much higher inter-annual variability, of which there were no seasonality detected by satellite observation or field measurement in 2018-2019 (Figure 4-3d, 4-3e). Likewise, there was a significant hysteretic senescence in EVI as opposed to GPP and SIF over two southern sites, particularly in the wet year of 2016-2017 (Figure 4-3d, 4-3e). The POS of SIF mostly advanced than those of EVI. Furthermore, we found that multi-year series of GOME-2 SIF were more erratic and deviated from the fitted SSA-reconstructed curves than GPP and EVI across northern humid sites as well as southern arid sites.

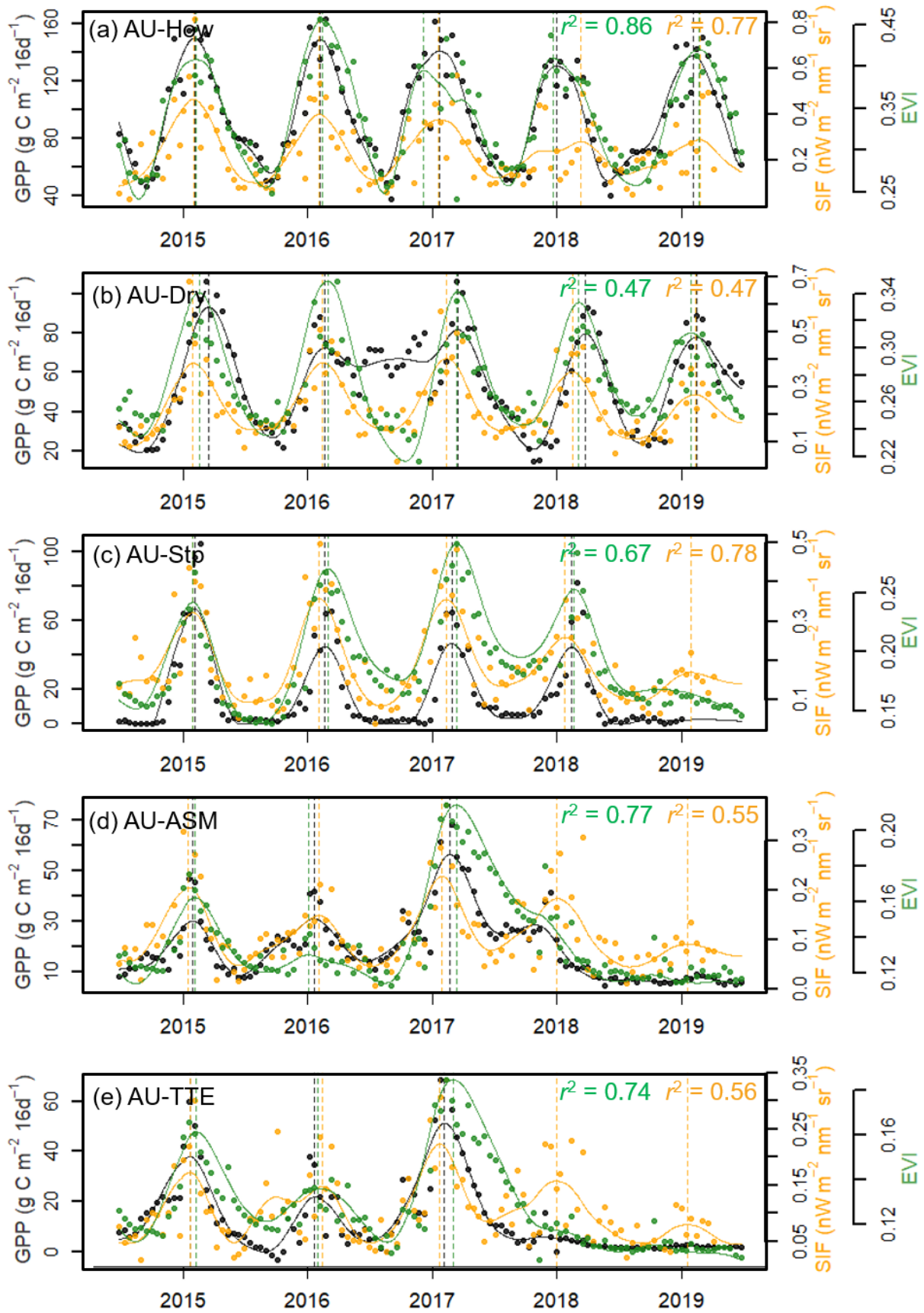


Figure 4-3 Time series of SSA-reconstructed tower-based GPP, GOME-2 SIF, MODIS EVI over 5 flux tower sites. R-squared ( $r^2$ ) refer to the correlations between GPP and EVI (green), GPP and SIF (orange) respectively. Vertical dashed lines refer to the peak of growing season in each hydrological year.

To assess the ability of SIF and EVI to track the seasonal dynamics of dryland vegetation as delineated by tower-based GPP, mean seasonal cycles of vegetation variables (normalized to unity at the maxima) over 5 selected tower sites during 2014-2019 are shown in Figure 4-4. For northern mesic site AU-How, GOME-2 SIF indicates a consistent growing season with tower data, in contrast to 1-2 months lagged seasonal profile of EVI during both green-up and senescent periods (Figure 4-4a). Conversely, a notably advanced springtime increase and earlier autumn drop is observed in SIF relative to tower-based GPP and EVI for AU-Dry site (Figure 4-4b). For three semi-arid and arid sites (AU-Stp, AU-ASM, AU-TTE), both GPP and SIF show a slightly narrower mean seasonal profile as opposed to two northern sites (Figure 4-4c, 4-4d, 4-4e). Besides, there are a substantial later senescence in EVI as compared with GPP, SIF, and APAR ( $EVI \times PAR$ ) over southern water-limited sites. Likewise, the seasonal profiles of APAR significantly shifted 1~2 month earlier relative to those of EVI over all selected sites.

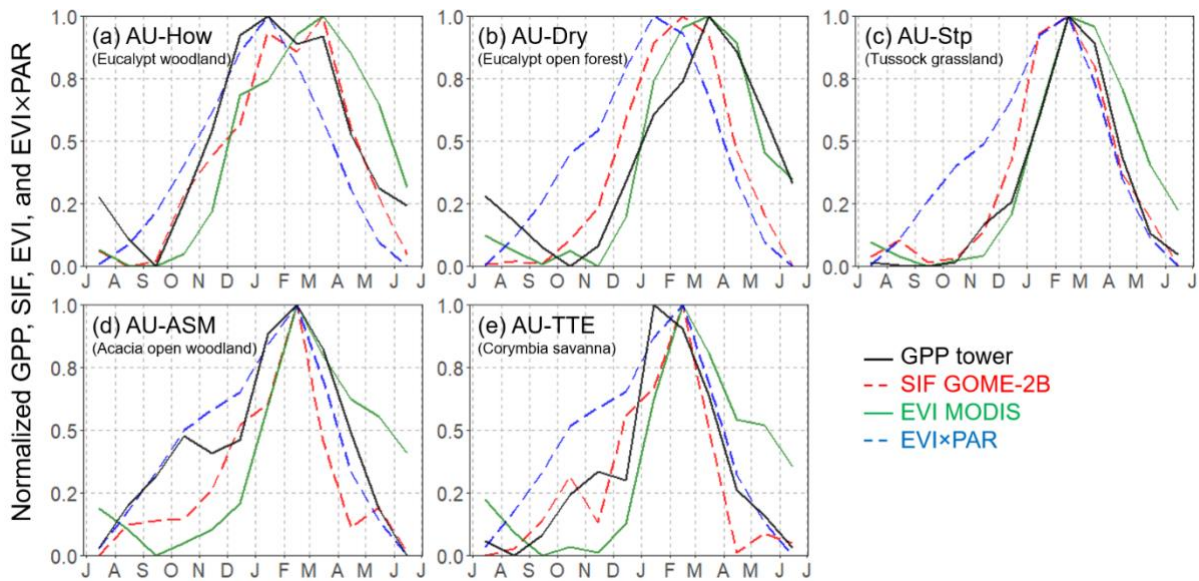


Figure 4-4 Seasonal cycle (mean) of tower-based GPP, GOME-2 SIF, MODIS EVI, and EVI×PAR over 5 selected local sites during 2014-2019. Curves are normalized with respect to unity at the maximum annual value. Satellite observations were extracted within a 3×3 window centered at each flux tower site (SIF: 1.5°×1.5°, EVI and EVI×PAR: 0.15°×0.15°).

The differences of key phenological metrics (SOS and EOS) derived from satellite-observed SIF and EVI as compared with tower-based GPP over 5 flux tower sites during 2014-2019 are presented in Table 4-1. For SOS over northern three sites (AU-How, AU-Dry, and AU-Stp), the mean absolute errors (MAE) of both SIF and EVI ranging from 7 to 32 days were generally less than that over two southern arid sites (AU-ASM and AU-TTE, ranging from 31 to 54 days). On the contrary, there were a larger discrepancy in EOS at AU-How and AU-Dry (MAE ranges from 39 to 60 days). Besides for two southern sites (AU-ASM and AU-TTE), the differences of EOS between EVI and GPP were notably larger than those between SIF and GPP.

Table 4-1 Summary of differences (days) in SOS and EOS derived from SIF, EVI compared with that derived from tower-based GPP. MAE: mean absolute error. Negative values represent an earlier green-up (SOS) or senescence (EOS) of SIF, EVI relative to that of GPP.

Site	Data	SOS					MAE	EOS					MAE
		2014-2015	2015-2016	2016-2017	2017-2018	2018-2019		2014-2015	2015-2016	2016-2017	2017-2018	2018-2019	
AU-How	SIF-GPP	6	24	-4	-21	0	11	-80	20	7	44	-42	39
	EVI-GPP	-17	-12	10	3	-6	10	9	74	83	24	15	41
AU-Dry	SIF-GPP	-56	3	-53	-38	-10	32	-63	-71	-42	-47	-75	60
	EVI-GPP	-6	5	-27	-16	-8	12	-39	-55	-5	-23	-78	40
AU-Stp	SIF-GPP	2	-21	-33	-21		19	-5	-14	-14	0		8
	EVI-GPP	-3	0	6	17		7	3	12	22	10		12
AU-ASM	SIF-GPP	22	108	-25			52	-11	9	-31			17
	EVI-GPP	37	86	-10			44	14	84	34			44
AU-TTE	SIF-GPP	15	-134	-13			54	-2	9	-27			13
	EVI-GPP	67	-25	1			31	20	84	42			49

### 4.3.2 Biogeographic patterns of vegetation phenology

To contrast the difference in the timing of seasonal greening derived from two satellite-based vegetation indicators and assess spatial variability over the NATT, the region-wide phenology maps based on EVI (Figure 4-5) and SIF (Figure 4-6) were generated. Besides, three representative years including 2014-2015 (normal year), 2016-2017 (wet year), and 2018-2019 (dry year) were selected to evaluate the impact of inter-annual precipitation variability on vegetation phenology. We found large spatial and inter-annual variation in the timing of key phenology transition dates retrieved from EVI (Figure 4-5), particularly in

the arid/semi-arid southern NATT (18°S ~ 23°S). In the extreme dry year of 2018-2019, nearly all pixels in the southern NATT exhibited no seasonality as compared with detectable phenology in normal and wet years (Figure 4-5c, 4-5f, 4-5i). There is a remarkable lagging trend in key phenological metrics (especially POS and EOS) in 2014-2015 and 2016-2017 from north to south across study area, of which Eucalyptus-dominated woodlands distributed in the humid northern NATT started to green-up earlier (September to October). By contrast, SOS of Acacia-dominated woodlands and Hummock-dominated grasslands distributed in the arid inland was generally 1-2 month behind (November to December). Similarly, the peak and end of growing season in the southern were 2-3 month delayed than those in the north during the normal/wet years.

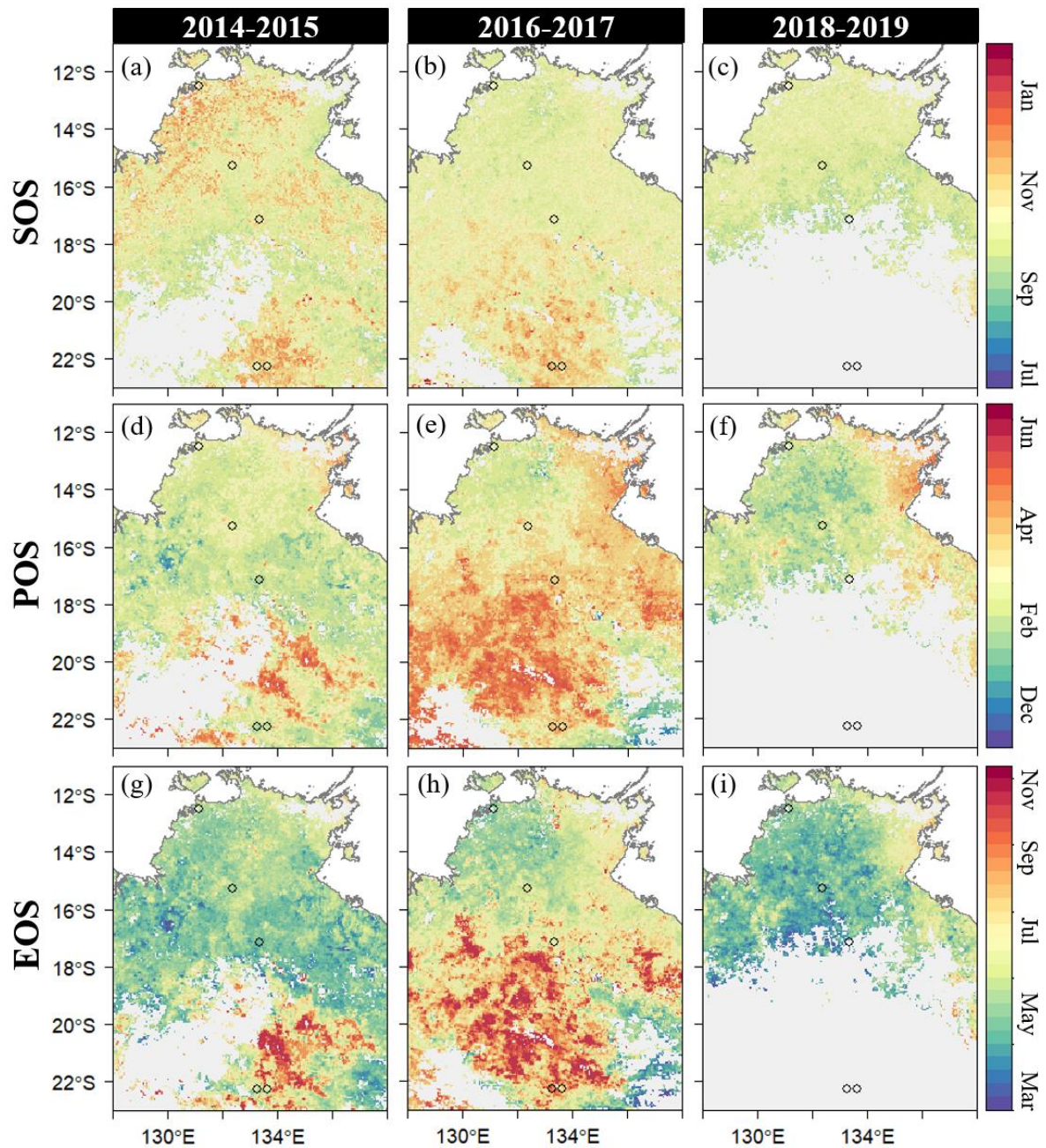


Figure 4-5 Spatial patterns of vegetation phenology based on EVI over the NATT study area across three representative hydrological years (2014-2015 normal year, 2016-2017 wet year, 2018-2019 dry year). The filled pixels (grey shaded areas) are either water body or without detectable phenology.

The spatial patterns of vegetation phenology derived from SIF across NATT were shown in Figure 4-6. Consistent with in-situ comparison, key phenological metrics of most pixels derived from SIF were generally earlier than those

derived from EVI. There was a contrary spatial pattern in the timing of transition dates between EVI and SIF, in which arid/semiarid ecosystems over southern NATT exhibited advanced POS (December to January) and EOS (March to April) as opposite to POS (February to March) and EOS (April to May) over northern humid area (Figure 4-6d~h). With reference to the normal/wet years, larger latitudinal changes in the peak of season between north ( $11^{\circ}\text{S}$ - $17^{\circ}\text{S}$ ) and south ( $17^{\circ}\text{S}$ - $23^{\circ}\text{S}$ ) NATT under the extremely dry condition of 2018-2019 were observed, and fractional pixels in the south were likewise without detectable phenology (Figure 4-6c, 4-6f).

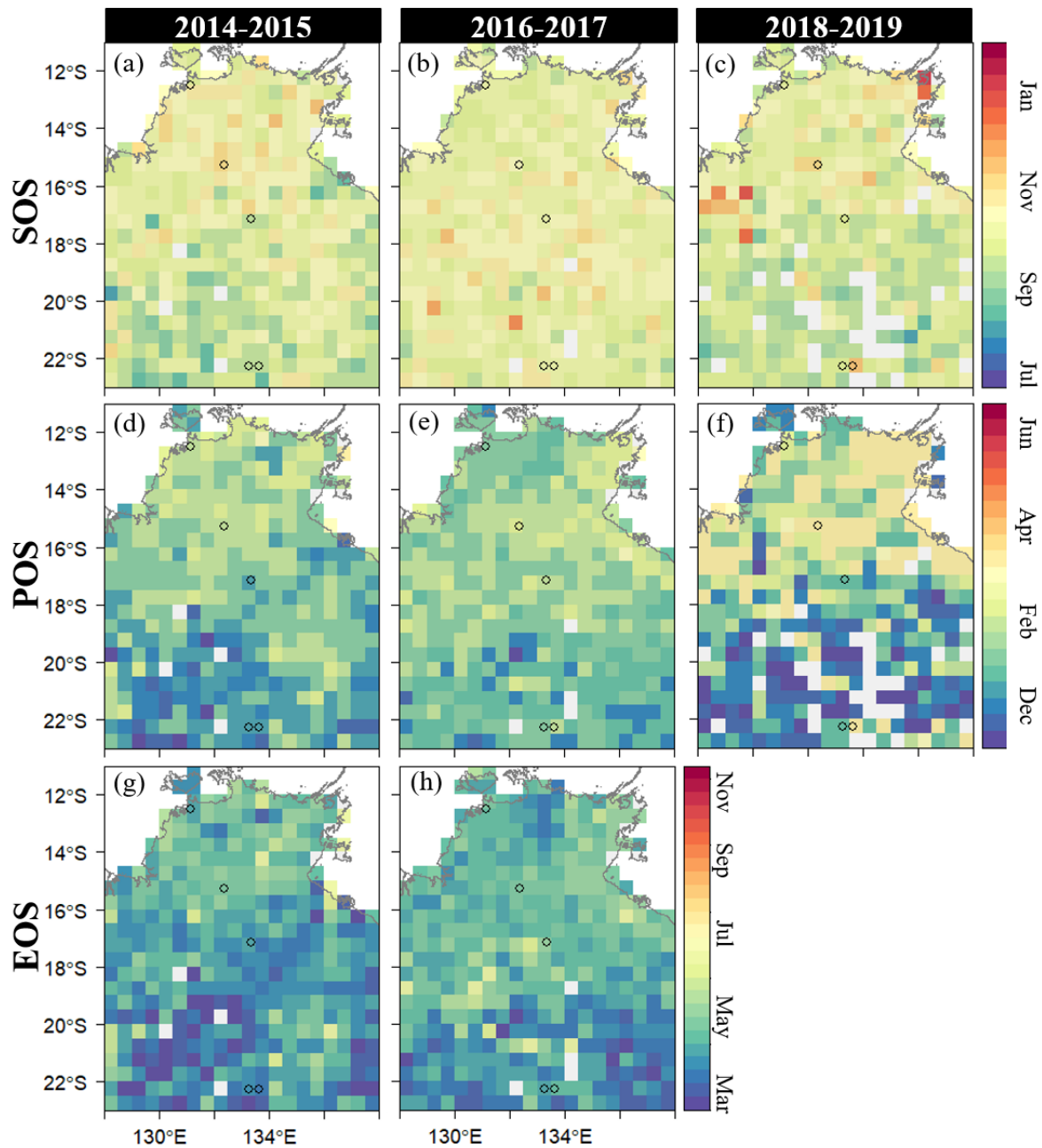


Figure 4-6 Spatial patterns of vegetation phenology based on SIF over the NATT study area across three representative hydrological. (2014-2015 normal year, 2016-2017 wet year, 2018-2019 dry year). The filled pixels (grey shaded areas) are either water body or without detectable phenology.

With the purpose of further contrasting the differences in the seasonal profile derived from SIF and EVI, relationship between green-up rate and brown-down rate of two satellite-based indicators among four major vegetation types were shown in Figure 4-7. For the semiarid/arid biomes (Hummock grasslands and

shrublands), the majority of pixels displayed considerably higher green-up rates than senescence rates ( $RSP_{EVI} > |RAU_{EVI}|$ ), of which the absolute senescence rate ( $|RAU_{EVI}|$ ) of Hummock grasslands were mostly less than  $0.002 \text{ d}^{-1}$  (Figure 4-7a, 4-7b). By contrast for northern sub-humid/humid biomes (Eucalyptus-dominated forests & woodlands and Tussock grasslands), there were notably rapid and comparable rates of green-up and senescence ( $0.0005 \text{ d}^{-1} \sim 0.004 \text{ d}^{-1}$ ) (Figure 4-7c, 4-7d). On the other hand, both rates of SIF ( $RSP_{SIF}$ ,  $RAU_{SIF}$ ) were less discrepancies in spite of diverse biomes (Figure 4-7e~7h).

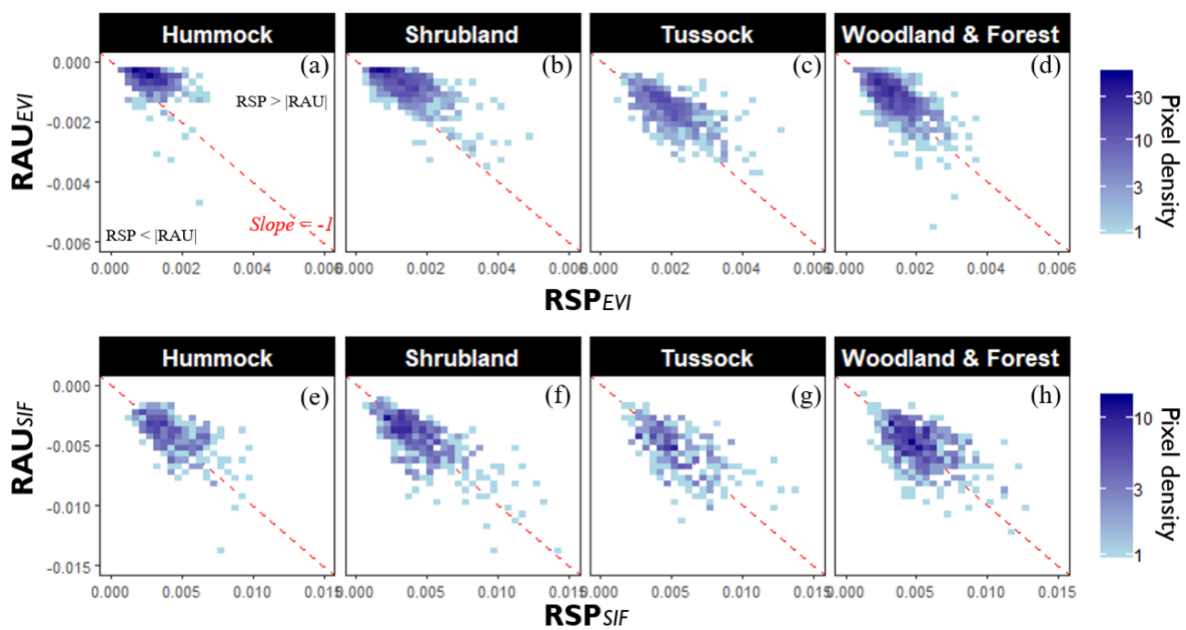


Figure 4-7 Scatter plot between spring green-up rates (RSP) and autumn senescence rates (RAU) of EVI and SIF among four major biomes across entire study region. Red dashed lines refer to -1:1 diagonal.

### 4.3.3 Interaction between environmental drivers and vegetation variables

To investigate the dominant factors controlling the seasonal and inter-annual variations in vegetation, biome-specific relationships of time series of principle

environmental drivers and vegetation variables (SIF, SIF<sub>PAR</sub>, SIF<sub>yield</sub>, and EVI) during 2014-2019 were shown in Figure 4-8. Apart from forests & woodlands, root zone soil moisture was most relevant with EVI ( $r^2$ : 0.42 ~ 0.79) relative to other drivers, among those temperature-related drivers were poorly correlated ( $r^2 < 0.16$ ) (Figure 4-8.a2~8.a4). By contrast, both moisture-related drivers as well as land surface temperature were highly corresponding with EVI over northern humid forests and woodlands ((Figure 8.a1). There was strongly correlation ( $r^2 > 0.8$ ) between SIF and EVI over forests, woodlands and tussock grasslands as compared with moderately correlation ( $r^2$ : 0.21, 0.38) over water-limited ecosystems (Figure 4-8b). Similarly compared with temperature-related drivers ( $r^2$ : 0 ~ 0.3), water-related factors (especially soil moisture) were more associated with SIF among all biomes. After removing the impact of solar radiation, there were an enhanced agreement between EVI and PAR-normalized SIF (SIF<sub>PAR</sub>) over tussock grassland, shrublands and hummock grasslands ( $r^2$ : 0.51 ~ 0.86) (Figure 4-8c). Likewise, the correlation between root zone soil moisture and SIF<sub>PAR</sub> were strengthened relative to those with SIF regardless of different vegetation types. Precipitation and surface soil moisture well agreed with APAR-normalized SIF (SIF<sub>yield</sub>) over forests & woodlands as well as tussock grasslands ( $r^2$ : 0.38 ~ 0.62) (Figure 4-8d). In addition, there was moderately increased correlation between air temperature and SIF<sub>yield</sub> ( $r^2$ : 0.22 ~ 0.4) in comparison to those with SIF or SIF<sub>PAR</sub> ( $r^2$ : 0 ~ 0.2).

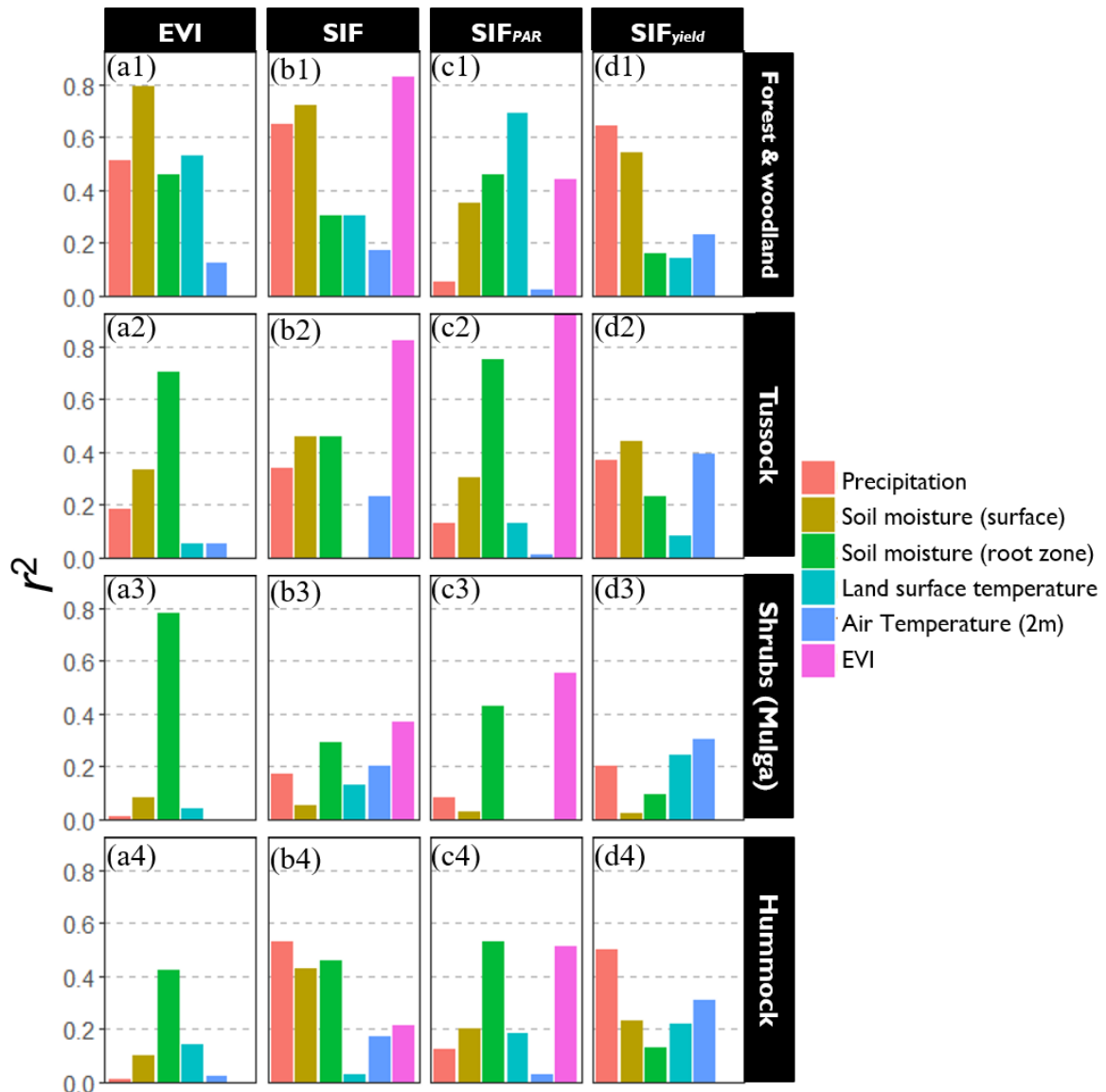


Figure 4-8 Relationship between environmental drivers and vegetation variables averaged by four major biome types across NATT. ( $p$  value < 0.001)

## 4.4 Discussion

### 4.4.1 Ground interpretations of the satellite-observed vegetation phenology

Although the selected five sites exhibited distinct seasonality revealed by eddy covariance flux measurements of photosynthesis, both satellite-based SIF and EVI generally captured seasonal dynamics and inter-annual variations over a variety of biomes (Figure 4-3, 4-4). In comparison with greenness-based

vegetation index, GOME-2 SIF displayed more consistently seasonal profile with tower-based GPP (Figure 4-4). Especially there was a significant “hysteresis effect” during the senescent period of EVI relative to that of GPP over water-limited ecosystems (Hummock grasslands and Shrublands), consistent with previous findings (Ma et al. 2013). In the wet year of 2016-2017, there was a considerable delayed senescence of EVI over two southern sites (AU-ASM and AU-TTE), relative to those of GPP and SIF (Figure 3). Besides, we found that the autumn senescence rates of EVI were considerably slower than the spring green-up rates of EVI over these arid/semiarid biomes (Figure 4-7), however, RAU and RSP of SIF were generally comparable. Aside from the slow chlorophyll degradation leading to gradual decrease of EVI (Huemmrich et al. 2005; Jenkins et al. 2007), another possible reason causing the discrepancies between EVI and SIF during the brown-down phase is that rapid decline in solar radiation in arid southern NATT gave rise to the swiftly dropping SIF signals. After removing the impact of PAR on SIF, there was a remarkably enhanced correlation between EVI and SIF across southern water-limited biomes (Figure 4-8b).

In contrast to GOME-2 SIF, MODIS EVI has improved capability (stronger  $r^2$ ) of tracking the interannual variations in GPP over most sites (except AU-Stp, Figure 4-3), probably owing to the substantial footprint mismatch between flux tower measurement and satellite observations (EVI: ~15km, SIF: ~150km).

Moreover, as compared with reflectance-based vegetation index, the high retrieval noises over low-productivity region result in more erratic SIF signals (A et al. 2017), giving rise to relatively weaker correlation with tower-based GPP. Given the sparsely spatial resolution of satellite-based SIF data, Wang, Beringer, et al. (2019) utilized a high-resolution contiguous SIF product ( $SIF_{OCO2\_005}$ ) over NATT, and found that  $SIF_{OCO2\_005}$  outperformed EVI at AU-ASM with a stronger temporal consistency with tower-based GPP. However, the up-scaled dataset was generated by native OCO-2 SIF signals along with MODIS reflectance through machine learning method (Yu et al. 2019), and it therefore contains information of canopy structure and chlorophyll content, like greenness-based indices. Even though, EVI showed tighter correlation with GPP (higher  $r^2$ ) than  $SIF_{OCO2\_005}$  at AU-Dry and AU-Stp in Wang, Beringer, et al. (2019) studies, congruent with our results. Nevertheless, the high spatiotemporal SIF data, such as TROPOMI SIF exhibiting striking consistency with field measurement (Chapter-3), has the great potential of characterizing the phenological dynamics of dryland vegetation in future.

#### **4.4.2 Spatial patterns of vegetation phenology**

Distinct biogeographic patterns in the timing of transition dates, especially POS and EOS, derived from SIF and EVI were observed (Figure 4-5, 4-6), of which there was a considerable latitudinal shift in vegetation phenology (EVI) with gradually delayed trend from north to south. This is in accordance with the in-

situ comparison that EVI displayed significantly late senescence at southern xeric sites as compared with GPP and SIF, particularly in the wet year of 2016-2017. In addition, the spatial phenomenon was in line with (Ma et al. 2013) findings, that the majority of EOS based on EVI in wet years (2005-2006, 2010-2011, and 2016-2017), especially in the southern NATT, was generally later than those in normal (2001-2002, 2014-2015) and drought years (2007-2008, 2018-2019) (Figure 4-5), probably as a consequence of the aforementioned “hysteresis effect”. On the contrary, there was less difference in the spatial patterns of EOS based on SIF between north and south NATT as well as in normal/wet years (Figure 4-6), of which both showed apparently earlier EOS, presumably due to the rapidly decreasing solar radiation over the southern inland. However, as an example of moderately inconsistent phenological metrics compared with field measurement GPP (Table 4-1), the coarse spatial and temporal resolution of GOME-2 SIF, as well as high retrieval noises, impede the full potential for capturing the seasonal and interannual variations in vegetation. Considering the drawbacks of existing greenness-based phenology products as well as the highly heterogeneous composition of dryland ecosystems, our findings imply that newly spaceborne SIF with improved spatiotemporal resolution, such as TROPOMI, has great capability for advancing our understanding of phenological characterization in Australia.

Furthermore, SIF and EVI displayed a stronger temporal consistency over northern mesic biomes (forests & woodlands and tussock grasslands) relative to southern xeric biomes (hummock grasslands and shrublands) (Figure 4-8). Soil moisture can explain more than 60% of the seasonal and interannual variability in EVI over most biomes (except hummock grasslands), suggesting it is the dominant factor controlling the dynamics of vegetation greenness. By contrast, the temperature-related drivers could barely explain more than 5% (except forests and woodlands). Despite the fact that solar radiation has substantial impacts on SIF signal, temperature- and moisture-related factors were almost equally contributing to the process of light use efficiency for fluorescence ( $SIF_{yield}$ , except forests & woodlands). It could partially explain the temporal discrepancies between SIF and EVI across diverse biomes.

#### **4.5 Conclusions**

In summary, we utilized satellite-based SIF and EVI observations to investigate the spatial patterns and seasonal dynamics of vegetation phenology across wet and dry years along the North Australian Tropical Transect. Considerable impacts of drought and wet extremes on phenology and function of dryland vegetation are revealed by both SIF and EVI, especially in arid/semiarid interior of Australia. In spite of sparse sampling and high retrieval noises, spaceborne SIF has the promising potential of assessing the characterization of phenology dynamics of dryland ecosystems.

## **Chapter 5 Conclusions**

### **5.1 Summary of key methodology, results, and conclusions**

#### **5.1.1 Chapter 2**

The responses of major biomes (Mulga woodland/shrubland and Hummock grassland) to two extreme wet pulses (2010-2011 and 2016-2017) were examined, utilising multi-satellite observations of solar-induced chlorophyll fluorescence (SIF) as a proxy for photosynthetic activity, enhanced vegetation index (EVI) as a measure of surface chlorophyll or greenness, as well as in-situ flux measurement. Wet intensity was defined by cumulative precipitation anomalies during the wet period, and were classified into five categories including Extreme wet, Severe wet, Intense wet, Moderate wet, and Dry. Three relatively “pure” test-pixels (TPs) at a 0.5° spatial resolution representing the major vegetation types were selected to examine variation in response to extreme wet events across vegetation types along with biome-specific vegetation-moisture relationship.

The results showed EVI with markedly amplified seasonal amplitude was considerably responsive to both extreme wet events. Due to weak responsiveness of Hummock grassland in 2016-2017 wet pulse, enhancement of SIF was notably lower than that in 2010-2011. Mulga woodland was invariably most responsive among major biomes, ascribed to its strong sensitivity to soil moisture availability. Despite a robust linear SIF-GPP relationship at site level,

spatially coarse SIF derived from the GOME-2 has imperfect capacity for capturing spatiotemporal dynamics over xeric central Australia.

### **5.1.2 Chapter 3**

In this chapter, we utilised monthly the Standardized Precipitation Evapotranspiration Index to characterize the spatial and temporal dynamics of the 2018-2019 extreme drought event across Australia. Two categories of dry condition including extreme drought ( $\text{SPEI} \leq -2$ ) and non-extreme drought ( $-2 < \text{SPEI} \leq -0.5$ ) were defined to investigate the responses of dryland vegetation to different drought severity. Four-pair region of interest distributed from mesic northern to xeric southern areas were selected to further examine biome-specific responses the at regional scale. The correlations between tower-based GPP and satellite-based SIF, EVI at different spatial ( $0.5^\circ$ ,  $0.05^\circ$ ) and temporal (monthly, 16-day) resolutions was calculated.

The results demonstrate satellite-observed SIF has potential for characterizing and monitoring the spatiotemporal dynamics of drought over water-limited ecosystem in spite of sparse sampling and high-retrieval noise. While SIF could earlier detect drought-related loss than enhanced vegetation index in northern mesic ecosystem, both SIF and EVI simultaneously captured the losses of arid/semiarid plants growth in the beginning of drought at monthly and 16-day scales. Semiarid ecosystem showing largest reduction was most sensitive to

climate extremes regardless of drought severity and time scales. Furthermore, our study highlight that SIF retrieved from recently launched TROPOMI featuring substantially enhanced spatiotemporal resolution has promising capability of accurately tracking the drought-induced variation of heterogeneous dryland vegetation.

### **5.1.3 Chapter 4**

Five key phenological metrics, such as start of season, peak of season, end of season, spring green-up rate, and autumn senescent rate, were retrieved from SSA re-constructed SIF, EVI series during recent five years including a wet year (2016-2017) and a dry year (2018-2019). Relationship between primary environmental drivers and vegetation variables (SIF,  $SIF_{PAR}$ ,  $SIF_{yield}$ , EVI) across four major biome types was calculated to examine the interaction and further explore the difference between SIF and EVI.

The results show that substantial impacts of extreme drought and intense wet on phenology and function of dryland vegetation are revealed by both SIF and EVI, especially in arid/semiarid interior of Australia without detectable seasonality in the dry year of 2018-2019. Besides, greenness-based phenological metrics over southern xeric region, such as Hummock grasslands and shrublands, exhibit a considerable delayed senescence as compared with SIF and tower-based GPP in the wet year of 2016-2017. In spite of sparse sampling and high retrieval noises, spaceborne SIF observations, offsetting the

drawbacks of greenness-based phenology products, have great potential of mapping and characterizing spatiotemporal dynamics of dryland ecosystems.

## **5.2 Limitation and future research directions**

In this research, I contributed to a better understanding of spatial variations and temporal dynamics of Australia's dryland vegetation under a variety of climate extremes with the help of the incorporation of satellite-observed greenness and fluorescence. Spaceborne SIF present a more direct means to assess plants photosynthesis relative to the frequently-used traditional greenness indices.

Although the existing longest satellite-based SIF records retrieved from GOME-2 show a strong correspondence with field measurement of GPP, the high retrieval noises over low-productivity region result in more erratic SIF signals.

On a basis of spatially coarse resolution and degradation of GOME-2 instrument, heterogeneity remains in the biome-level analysis though we set stringent criteria for "pure" pixels selection. Besides, the largely mismatch footprints between satellite observations and eddy covariance measurement give rise to more uncertainties in assessing the SIF-GPP relationship as well as underlay mechanism. In chapter 3, the high spatiotemporal SIF data based on newly-launched TROPOMI were utilized to assess the dryland vegetation under extreme drought, and it exhibited a more striking consistency with tower-based GPP relative to GOME-2 SIF and MODIS EVI, implying that TROPOMI SIF has the great potential of characterizing the phenological dynamics of dryland

vegetation in future. However, it is worth noting that abundant of negative values of TROPOMI SIF was observed over central Australia in the dry year of 2018-2019, owing to the retrieval noise. Therefore, for a more in-depth study, a comprehensive assessment of capability of this newly dataset over dryland ecosystem under a variety of climate scenarios needs to be conducted in future. In this study, an another SIF data from OCO-2 with high spatiotemporal resolution have not taken into account, mainly as a consequence of its discontinuous spatial coverage. Recent studies reported the combined SIF products based on OCO-2 data as well as MODIS reflectance (OCO) show great capability for characterizing and mapping the dynamics of dryland vegetation. Moreover, there are only two adjacent flux tower sites (AU-ASM and AU-TTE) within the vast interior of Australia, particularly excluding the largest single vegetation group of Hummock grasslands. The scarcity of field measurements over arid/semiarid ecosystems impedes broad validation of satellite observations over most vegetation types. With the increasing field observations, such as OzFlux Network, TERN's supersites, and Australian Phenocam Network, those will provide the substantial "ground truth" and contribute to the enhanced understanding of the intrinsic vegetation community properties and the plant ecophysiological mechanisms that benefits for the interpretation of satellite observation.

# References

- A, G., Velicogna, I., Kimball, J.S., Du, J., Kim, Y., Colliander, A. & Njoku, E. 2017, 'Satellite-observed changes in vegetation sensitivities to surface soil moisture and total water storage variations since the 2011 Texas drought', *Environmental Research Letters*, vol. 12, no. 5.
- Ahlström, A., Raupach, M.R., Schurgers, G., Smith, B., Arneeth, A., Jung, M., Reichstein, M., Canadell, J.G., Friedlingstein, P. & Jain, A.K. 2015, 'The dominant role of semi-arid ecosystems in the trend and variability of the land CO<sub>2</sub> sink', *Science*, vol. 348, no. 6237, pp. 895-9.
- Allan, G.E. & Southgate, R.I. 2002, 'Fire regimes in spinifex landscapes', *Flammable Australia: The Fire Regimes and Biodiversity of a Continent*. (Eds RA Bradstock, JE Williams and MA Gill.) pp, pp. 145-76.
- Andela, N., Liu, Y., Van Dijk, A., De Jeu, R. & McVicar, T. 2013, 'Global changes in dryland vegetation dynamics (1988-2008) assessed by satellite remote sensing: comparing a new passive microwave vegetation density record with reflective greenness data', *Biogeosciences*, vol. 10, no. 10.
- Anderson, B.M., Thiele, K.R., Grierson, P.F., Krauss, S.L., Nevill, P.G., Small, I.D., Zhong, X. & Barrett, M.D. 2019, 'Recent range expansion in Australian hummock grasses (*Triodia*) inferred using genotyping-by-sequencing', *AoB Plants*, vol. 11, no. 2, p. plz017.
- Andrew, R.L., Guan, H. & Batelaan, O. 2017, 'Large-scale vegetation responses to terrestrial moisture storage changes', *Hydrology and Earth System Sciences*, vol. 21, no. 9, pp. 4469-78.
- Aragão, L.E., Anderson, L.O., Fonseca, M.G., Rosan, T.M., Vedovato, L.B., Wagner, F.H., Silva, C.V., Junior, C.H.S., Arai, E. & Aguiar, A.P. 2018, '21st Century drought-related fires counteract the decline of Amazon deforestation carbon emissions', *Nature communications*, vol. 9, no. 1, pp. 1-12.
- Arias-Ortiz, A., Serrano, O., Masqué, P., Lavery, P.S., Mueller, U., Kendrick, G.A., Rozaimi, M., Esteban, A., Fourqurean, J.W. & Marbà, N. 2018, 'A marine heatwave drives massive losses from the world's largest seagrass carbon stocks', *Nature Climate Change*, vol. 8, no. 4, p. 338.
- Asner, G.P. & Martin, R.E. 2008, 'Spectral and chemical analysis of tropical forests: Scaling from leaf to canopy levels', *Remote Sensing of Environment*, vol. 112, no. 10, pp. 3958-70.
- Barron-Gafford, G.A., Scott, R.L., Jenerette, G.D., Hamerlynck, E.P. & Huxman, T.E. 2012, 'Temperature and precipitation controls over leaf- and ecosystem-level CO<sub>2</sub> flux along a woody plant encroachment gradient', *Global Change Biology*, vol. 18, no. 4, pp. 1389-400.
- Beard, J., Beeston, G., Harvey, J., Hopkins, A. & Shepherd, D. 2013, 'The vegetation of Western Australia at the 1: 3,000,000 scale. Explanatory memoir', *Conservation Science Western Australia*, vol. 9, no. 1.
- Bellprat, O., Guemas, V., Doblás-Reyes, F. & Donat, M.G. 2019, 'Towards reliable extreme weather and climate event attribution', *Nature communications*, vol. 10, no. 1, pp. 1-7.
- Biederman, J.A., Scott, R.L., Bell, T.W., Bowling, D.R., Dore, S., Garatuza-Payan, J., Kolb, T.E., Krishnan, P., Krofcheck, D.J. & Litvak, M.E. 2017, 'CO<sub>2</sub> exchange and evapotranspiration across dryland ecosystems of southwestern North America', *Global change biology*, vol. 23, no. 10, pp. 4204-21.
- Bliege Bird, R., Bird, D.W. & Coddling, B.F. 2016, 'People, El Niño southern oscillation and fire in Australia: fire regimes and climate controls in hummock grasslands', *Philosophical Transactions of the Royal Society B: Biological Sciences*, vol. 371, no. 1696, p. 20150343.
- Boening, C., Willis, J.K., Landerer, F.W., Nerem, R.S. & Fasullo, J. 2012, 'The 2011 La Niña: So strong, the oceans fell', *Geophysical Research Letters*, vol. 39, no. 19.
- Bowman, D., Boggs, G.S. & Prior, L. 2008, 'Fire maintains an *Acacia aneura* shrubland—*Triodia* grassland mosaic in central Australia', *Journal of Arid Environments*, vol. 72, no. 1, pp. 34-47.
- Braswell, B., Schimel, D.S., Linder, E. & Moore, B. 1997, 'The response of global terrestrial ecosystems to interannual temperature variability', *Science*, vol. 278, no. 5339, pp. 870-3.

- Broich, M., Huete, A., Paget, M., Ma, X., Tulbure, M., Coupe, N.R., Evans, B., Beringer, J., Devadas, R. & Davies, K. 2015, 'A spatially explicit land surface phenology data product for science, monitoring and natural resources management applications', *Environmental Modelling & Software*, vol. 64, pp. 191-204.
- Broich, M., Huete, A., Tulbure, M.G., Ma, X., Xin, Q., Paget, M., Restrepo-Coupe, N., Davies, K., Devadas, R. & Held, A. 2014, 'Land surface phenological response to decadal climate variability across Australia using satellite remote sensing', *Biogeosciences*, vol. 11, no. 18, pp. 5181-98.
- Broich, M., Tulbure, M.G., Verbesselt, J., Xin, Q. & Wearne, J. 2018, 'Quantifying Australia's dryland vegetation response to flooding and drought at sub-continental scale', *Remote Sensing of Environment*, vol. 212, pp. 60-78.
- Cao, M. & Woodward, F.I. 1998, 'Dynamic responses of terrestrial ecosystem carbon cycling to global climate change', *Nature*, vol. 393, no. 6682, pp. 249-52.
- Chang, Q., Xiao, X., Jiao, W., Wu, X., Doughty, R., Wang, J., Du, L., Zou, Z. & Qin, Y. 2019, 'Assessing consistency of spring phenology of snow-covered forests as estimated by vegetation indices, gross primary production, and solar-induced chlorophyll fluorescence', *Agricultural and Forest Meteorology*, vol. 275, pp. 305-16.
- Chen, C., Cleverly, J., Zhang, L., Yu, Q. & Eamus, D. 2016, 'Modelling Seasonal and Inter-annual Variations in Carbon and Water Fluxes in an Arid-Zone Acacia Savanna Woodland, 1981–2012', *Ecosystems*, vol. 19, no. 4, pp. 625-44.
- Chen, T., de Jeu, R.A.M., Liu, Y.Y., van der Werf, G.R. & Dolman, A.J. 2014, 'Using satellite based soil moisture to quantify the water driven variability in NDVI: A case study over mainland Australia', *Remote Sensing of Environment*, vol. 140, pp. 330-8.
- Cleverly, J., Boulain, N., Villalobos-Vega, R., Grant, N., Faux, R., Wood, C., Cook, P.G., Yu, Q., Leigh, A. & Eamus, D. 2013, 'Dynamics of component carbon fluxes in a semi-arid Acacia woodland, central Australia', *Journal of Geophysical Research: Biogeosciences*, vol. 118, no. 3, pp. 1168-85.
- Cleverly, J., Eamus, D., Restrepo Coupe, N., Chen, C., Maes, W., Li, L., Faux, R., Santini, N.S., Rumman, R., Yu, Q. & Huete, A. 2016, 'Soil moisture controls on phenology and productivity in a semi-arid critical zone', *Sci Total Environ*, vol. 568, pp. 1227-37.
- Cleverly, J., Eamus, D., Van Gorsel, E., Chen, C., Rumman, R., Luo, Q., Coupe, N.R., Li, L., Kljun, N., Faux, R., Yu, Q. & Huete, A. 2016, 'Productivity and evapotranspiration of two contrasting semiarid ecosystems following the 2011 global carbon land sink anomaly', *Agricultural and Forest Meteorology*, vol. 220, pp. 151-9.
- Dai, A. 2011, 'Characteristics and trends in various forms of the Palmer Drought Severity Index during 1900–2008', *Journal of Geophysical Research: Atmospheres*, vol. 116, no. D12.
- De Beurs, K.M. & Henebry, G.M. 2005, 'Land surface phenology and temperature variation in the International Geosphere–Biosphere Program high-latitude transects', *Global Change Biology*, vol. 11, no. 5, pp. 779-90.
- Detmers, R.G., Hasekamp, O., Aben, I., Houweling, S., van Leeuwen, T.T., Butz, A., Landgraf, J., Köhler, P., Guanter, L. & Poulter, B. 2015, 'Anomalous carbon uptake in Australia as seen by GOSAT', *Geophysical Research Letters*, vol. 42, no. 19, pp. 8177-84.
- Dickman, C., Wardle, G., Foulkes, J. & de Preu, N. 2014, '10 Desert complex environments', *Biodiversity and environmental change: monitoring, challenges and direction*, p. 379.
- Dikty, S., Richter, A., Weber, M., Noël, S., Bovensmann, H., Wittrock, F. & Burrows, J. 2011, 'GOME-2 on MetOp-A Support for Analysis of GOME-2 In-Orbit Degradation and Impacts on Level 2 Data Products', *Final Report, Version*, vol. 1, p. 14.
- Dixon, R.K., Solomon, A., Brown, S., Houghton, R., Trexler, M. & Wisniewski, J. 1994, 'Carbon pools and flux of global forest ecosystems', *Science*, vol. 263, no. 5144, pp. 185-90.

- Eamus, D., Cleverly, J., Boulain, N., Grant, N., Faux, R. & Villalobos-Vega, R. 2013, 'Carbon and water fluxes in an arid-zone Acacia savanna woodland: An analyses of seasonal patterns and responses to rainfall events', *Agricultural and Forest Meteorology*, vol. 182-183, pp. 225-38.
- Eamus, D., Huete, A., Cleverly, J., Nolan, R.H., Ma, X., Tarin, T. & Santini, N.S. 2016, 'Mulga, a major tropical dry open forest of Australia: recent insights to carbon and water fluxes', *Environmental Research Letters*, vol. 11, no. 12, p. 125011.
- Evans, J.P., Meng, X. & McCabe, M.F. 2017, 'Land surface albedo and vegetation feedbacks enhanced the millennium drought in south-east Australia', *Hydrology and Earth System Sciences*, vol. 21, no. 1, pp. 409-22.
- Flanagan, L.B. & Adkinson, A.C. 2011, 'Interacting controls on productivity in a northern Great Plains grassland and implications for response to ENSO events', *Global Change Biology*, vol. 17, no. 11, pp. 3293-311.
- Flechtner, F., Dahle, C., Landerer, F., Webb, F., Watkins, M., Massmann, H. & Bettadpur, S. 2018, 'GRACE Follow-On: Current Mission Status and next steps', *EGU General Assembly Conference Abstracts*, vol. 20, p. 8990.
- Frank, D., Reichstein, M., Bahn, M., Thonicke, K., Frank, D., Mahecha, M.D., Smith, P., van der Velde, M., Vicca, S., Babst, F., Beer, C., Buchmann, N., Canadell, J.G., Ciais, P., Cramer, W., Ibrom, A., Miglietta, F., Poulter, B., Rammig, A., Seneviratne, S.I., Walz, A., Wattenbach, M., Zavala, M.A. & Zscheischler, J. 2015, 'Effects of climate extremes on the terrestrial carbon cycle: concepts, processes and potential future impacts', *Glob Chang Biol*, vol. 21, no. 8, pp. 2861-80.
- Frankenberg, C., Fisher, J.B., Worden, J., Badgley, G., Saatchi, S.S., Lee, J.E., Toon, G.C., Butz, A., Jung, M. & Kuze, A. 2011, 'New global observations of the terrestrial carbon cycle from GOSAT: Patterns of plant fluorescence with gross primary productivity', *Geophysical Research Letters*, vol. 38, no. 17.
- Frankenberg, C., O'Dell, C., Guanter, L. & McDuffie, J. 2012, 'Remote sensing of near-infrared chlorophyll fluorescence from space in scattering atmospheres: implications for its retrieval and interferences with atmospheric CO<sub>2</sub> retrievals', *Atmospheric Measurement Techniques*, vol. 5, no. 8, pp. 2081-94.
- Friedl, M., Henebry, G., Reed, B., Huete, A., White, M., Morisette, J., Nemani, R., Zhang, X., Myneni, R. & Friedl, M. 2006, 'Land surface phenology', *A Community White Paper requested by NASA*, vol. 10.
- Gentine, P. & Alemohammad, S.H. 2018, 'Reconstructed Solar-Induced Fluorescence: A Machine Learning Vegetation Product Based on MODIS Surface Reflectance to Reproduce GOME-2 Solar-Induced Fluorescence', *Geophys Res Lett*, vol. 45, no. 7, pp. 3136-46.
- Gonsamo, A., Chen, J.M., He, L., Sun, Y., Rogers, C. & Liu, J. 2019, 'Exploring SMAP and OCO-2 observations to monitor soil moisture control on photosynthetic activity of global drylands and croplands', *Remote Sensing of Environment*, vol. 232, p. 111314.
- Grace, J., José, J.S., Meir, P., Miranda, H.S. & Montes, R.A. 2006, 'Productivity and carbon fluxes of tropical savannas', *Journal of Biogeography*, vol. 33, no. 3, pp. 387-400.
- Griffin, G. & Hodgkinson, K. 1986, 'The use of fire for the management of the mulga land vegetation in Australia', *The mulga lands*.(Ed. PS Sattler) pp, pp. 93-7.
- Guan, K., Pan, M., Li, H., Wolf, A., Wu, J., Medvigy, D., Caylor, K.K., Sheffield, J., Wood, E.F., Malhi, Y., Liang, M., Kimball, J.S., Saleska, Scott R., Berry, J., Joiner, J. & Lyapustin, A.I. 2015, 'Photosynthetic seasonality of global tropical forests constrained by hydroclimate', *Nature Geoscience*, vol. 8, no. 4, pp. 284-9.
- Guanter, L., Zhang, Y., Jung, M., Joiner, J., Voigt, M., Berry, J.A., Frankenberg, C., Huete, A.R., Zarco-Tejada, P., Lee, J.E., Moran, M.S., Ponce-Campos, G., Beer, C., Camps-Valls, G., Buchmann, N., Gianelle, D., Klumpp, K., Cescatti, A., Baker, J.M. & Griffis, T.J. 2014, 'Global and time-resolved monitoring of crop photosynthesis with chlorophyll fluorescence', *Proc Natl Acad Sci U S A*, vol. 111, no. 14, pp. E1327-33.

- Hansen, J., Sato, M. & Ruedy, R. 2012, 'Perception of climate change', *Proceedings of the National Academy of Sciences*, vol. 109, no. 37, pp. E2415-E23.
- Haverd, V., Smith, B. & Trudinger, C. 2016, 'Process contributions of Australian ecosystems to interannual variations in the carbon cycle', *Environmental Research Letters*, vol. 11, no. 5.
- Hiddink, J.G., Burrows, M.T. & García Molinos, J. 2015, 'Temperature tracking by North Sea benthic invertebrates in response to climate change', *Global Change Biology*, vol. 21, no. 1, pp. 117-29.
- Hmimina, G., Dufrêne, E., Pontailier, J.-Y., Delpierre, N., Aubinet, M., Caquet, B., De Grandcourt, A., Burban, B., Flechard, C. & Granier, A. 2013, 'Evaluation of the potential of MODIS satellite data to predict vegetation phenology in different biomes: An investigation using ground-based NDVI measurements', *Remote Sensing of Environment*, vol. 132, pp. 145-58.
- Huang, J., Li, Y., Fu, C., Chen, F., Fu, Q., Dai, A., Shinoda, M., Ma, Z., Guo, W. & Li, Z. 2017, 'Dryland climate change: Recent progress and challenges', *Reviews of Geophysics*, vol. 55, no. 3, pp. 719-78.
- Huang, J., Yu, H., Guan, X., Wang, G. & Guo, R. 2016, 'Accelerated dryland expansion under climate change', *Nature Climate Change*, vol. 6, no. 2, p. 166.
- Huete, A., Didan, K., Miura, T., Rodriguez, E.P., Gao, X. & Ferreira, L.G. 2002, 'Overview of the radiometric and biophysical performance of the MODIS vegetation indices', *Remote sensing of environment*, vol. 83, no. 1-2, pp. 195-213.
- Huete, A.R., Restrepo-Coupe, N., Ratana, P., Didan, K., Saleska, S.R., Ichii, K., Panuthai, S. & Gamo, M. 2008, 'Multiple site tower flux and remote sensing comparisons of tropical forest dynamics in Monsoon Asia', *Agricultural and Forest Meteorology*, vol. 148, no. 5, pp. 748-60.
- Hufkens, K., Friedl, M., Sonnentag, O., Braswell, B.H., Milliman, T. & Richardson, A.D. 2012, 'Linking near-surface and satellite remote sensing measurements of deciduous broadleaf forest phenology', *Remote Sensing of Environment*, vol. 117, pp. 307-21.
- Jenkins, J., Richardson, A.D., Braswell, B., Ollinger, S.V., Hollinger, D.Y. & Smith, M.-L. 2007, 'Refining light-use efficiency calculations for a deciduous forest canopy using simultaneous tower-based carbon flux and radiometric measurements', *Agricultural and Forest Meteorology*, vol. 143, no. 1-2, pp. 64-79.
- Jeong, S.-J., Schimel, D., Frankenberg, C., Drewry, D.T., Fisher, J.B., Verma, M., Berry, J.A., Lee, J.-E. & Joiner, J. 2017, 'Application of satellite solar-induced chlorophyll fluorescence to understanding large-scale variations in vegetation phenology and function over northern high latitude forests', *Remote Sensing of Environment*, vol. 190, pp. 178-87.
- Jiang, P., Liu, H., Piao, S., Ciais, P., Wu, X., Yin, Y. & Wang, H. 2019, 'Enhanced growth after extreme wetness compensates for post-drought carbon loss in dry forests', *Nat Commun*, vol. 10, no. 1, p. 195.
- Joiner, J., Guanter, L., Lindstrot, R., Voigt, M., Vasilkov, A., Middleton, E., Huemmrich, K., Yoshida, Y. & Frankenberg, C. 2013, 'Global monitoring of terrestrial chlorophyll fluorescence from moderate-spectral-resolution near-infrared satellite measurements: methodology, simulations, and application to GOME-2', *Atmospheric Measurement Techniques*, vol. 6, no. 10, pp. 2803-23.
- Joiner, J., Yoshida, Y., Guanter, L. & Middleton, E.M. 2016, 'New methods for the retrieval of chlorophyll red fluorescence from hyperspectral satellite instruments: simulations and application to GOME-2 and SCIAMACHY', *Atmospheric Measurement Techniques*, vol. 9, pp. 3939-67.
- Kath, J., Le Brocque, A.F., Reardon-Smith, K. & Apan, A. 2019, 'Remotely sensed agricultural grassland productivity responses to land use and hydro-climatic drivers under extreme drought and rainfall', *Agricultural and Forest Meteorology*, vol. 268, pp. 11-22.
- Knapp, A.K., Hoover, D.L., Wilcox, K.R., Avolio, M.L., Koerner, S.E., La Pierre, K.J., Loik, M.E., Luo, Y., Sala, O.E. & Smith, M.D. 2015, 'Characterizing differences in precipitation regimes of

- extreme wet and dry years: implications for climate change experiments', *Global change biology*, vol. 21, no. 7, pp. 2624-33.
- Köhler, P., Frankenberg, C., Magney, T.S., Guanter, L., Joiner, J. & Landgraf, J. 2018, 'Global retrievals of solar-induced chlorophyll fluorescence with TROPOMI: First results and intersensor comparison to OCO-2', *Geophysical Research Letters*, vol. 45, no. 19, pp. 10,456-10,63.
- Köhler, P., Guanter, L. & Joiner, J. 2015, 'A linear method for the retrieval of sun-induced chlorophyll fluorescence from GOME-2 and SCIAMACHY data'.
- Koutroulis, A.G. 2019, 'Dryland changes under different levels of global warming', *Science of The Total Environment*, vol. 655, pp. 482-511.
- Li, L., Wang, Y.P., Beringer, J., Shi, H., Cleverly, J., Cheng, L., Eamus, D., Huete, A., Hutley, L., Lu, X., Piao, S., Zhang, L., Zhang, Y. & Yu, Q. 2017, 'Responses of LAI to rainfall explain contrasting sensitivities to carbon uptake between forest and non-forest ecosystems in Australia', *Sci Rep*, vol. 7, no. 1, p. 11720.
- Liu, Y.Y., Van Dijk, A.I., De Jeu, R.A., Canadell, J.G., McCabe, M.F., Evans, J.P. & Wang, G. 2015, 'Recent reversal in loss of global terrestrial biomass', *Nature Climate Change*, vol. 5, no. 5, p. 470.
- Lu, H., Raupach, M.R., McVicar, T.R. & Barrett, D.J. 2003, 'Decomposition of vegetation cover into woody and herbaceous components using AVHRR NDVI time series', *Remote Sensing of Environment*, vol. 86, no. 1, pp. 1-18.
- Ma, X., Huete, A., Cleverly, J., Eamus, D., Chevallier, F., Joiner, J., Poulter, B., Zhang, Y., Guanter, L., Meyer, W., Xie, Z. & Ponce-Campos, G. 2016, 'Drought rapidly diminishes the large net CO<sub>2</sub> uptake in 2011 over semi-arid Australia', *Sci Rep*, vol. 6, p. 37747.
- Ma, X., Huete, A., Moore, C.E., Cleverly, J., Hutley, L.B., Beringer, J., Leng, S., Xie, Z., Yu, Q. & Eamus, D. 2020, 'Spatiotemporal partitioning of savanna plant functional type productivity along NATT', *Remote Sensing of Environment*, vol. 246, p. 111855.
- Ma, X., Huete, A., Moran, S., Ponce-Campos, G. & Eamus, D. 2015, 'Abrupt shifts in phenology and vegetation productivity under climate extremes', *Journal of Geophysical Research: Biogeosciences*, vol. 120, no. 10, pp. 2036-52.
- Ma, X., Huete, A., Yu, Q., Coupe, N.R., Davies, K., Broich, M., Ratana, P., Beringer, J., Hutley, L.B., Cleverly, J., Boulain, N. & Eamus, D. 2013, 'Spatial patterns and temporal dynamics in savanna vegetation phenology across the North Australian Tropical Transect', *Remote Sensing of Environment*, vol. 139, pp. 97-115.
- Ma, X., Huete, A., Yu, Q., Restrepo-Coupe, N., Beringer, J., Hutley, L.B., Kanniah, K.D., Cleverly, J. & Eamus, D. 2014, 'Parameterization of an ecosystem light-use-efficiency model for predicting savanna GPP using MODIS EVI', *Remote Sensing of Environment*, vol. 154, pp. 253-71.
- Ma, Z., Peng, C., Zhu, Q., Chen, H., Yu, G., Li, W., Zhou, X., Wang, W. & Zhang, W. 2012, 'Regional drought-induced reduction in the biomass carbon sink of Canada's boreal forests', *Proceedings of the National Academy of Sciences*, vol. 109, no. 7, pp. 2423-7.
- Madani, N., Kimball, J., Jones, L., Parazoo, N. & Guan, K. 2017, 'Global Analysis of Bioclimatic Controls on Ecosystem Productivity Using Satellite Observations of Solar-Induced Chlorophyll Fluorescence', *Remote Sensing*, vol. 9, no. 6.
- Madsen, H., Lawrence, D., Lang, M., Martinkova, M. & Kjeldsen, T. 2014, 'Review of trend analysis and climate change projections of extreme precipitation and floods in Europe', *Journal of Hydrology*, vol. 519, pp. 3634-50.
- Middleton, N. & Thomas, D. 1997, *World atlas of desertification.. ed. 2*, Arnold, Hodder Headline, PLC.
- Min, S.-K., Zhang, X., Zwiers, F.W. & Hegerl, G.C. 2011, 'Human contribution to more-intense precipitation extremes', *Nature*, vol. 470, no. 7334, p. 378.
- Moore, C.E., Beringer, J., Donohue, R.J., Evans, B., Exbrayat, J.F., Hutley, L.B. & Tapper, N.J. 2018, 'Seasonal, interannual and decadal drivers of tree and grass productivity in an Australian tropical savanna', *Glob Chang Biol*, vol. 24, no. 6, pp. 2530-44.

- Moreno-de las Heras, M., Saco, P.M., Willgoose, G.R. & Tongway, D.J. 2012, 'Variations in hydrological connectivity of Australian semiarid landscapes indicate abrupt changes in rainfall-use efficiency of vegetation', *Journal of Geophysical Research: Biogeosciences*, vol. 117, no. G3, pp. n/a-n/a.
- Moss, R.H., Edmonds, J.A., Hibbard, K.A., Manning, M.R., Rose, S.K., Van Vuuren, D.P., Carter, T.R., Emori, S., Kainuma, M. & Kram, T. 2010, 'The next generation of scenarios for climate change research and assessment', *Nature*, vol. 463, no. 7282, pp. 747-56.
- Nicholas, A.M.M., Franklin, D.C. & Bowman, D.M.J.S. 2011, 'Floristic uniformity across abrupt boundaries between *Triodia* hummock grassland and *Acacia* shrubland on an Australian desert sandplain', *Journal of Arid Environments*, vol. 75, no. 11, pp. 1090-6.
- Nicolai-Shaw, N., Zscheischler, J., Hirschi, M., Gudmundsson, L. & Seneviratne, S.I. 2017, 'A drought event composite analysis using satellite remote-sensing based soil moisture', *Remote Sensing of Environment*, vol. 203, pp. 216-25.
- Nix, H. & Austin, M. 1973, 'Mulga: a bioclimatic analysis', *Tropical Grasslands*, vol. 7, no. 1, pp. 9-21.
- Peng, D., Wu, C., Zhang, X., Yu, L., Huete, A.R., Wang, F., Luo, S., Liu, X. & Zhang, H. 2018, 'Scaling up spring phenology derived from remote sensing images', *Agricultural and Forest Meteorology*, vol. 256-257, pp. 207-19.
- Phillips, O.L., Aragão, L.E., Lewis, S.L., Fisher, J.B., Lloyd, J., López-González, G., Malhi, Y., Monteagudo, A., Peacock, J. & Quesada, C.A. 2009, 'Drought sensitivity of the Amazon rainforest', *Science*, vol. 323, no. 5919, pp. 1344-7.
- Pianka, E.R. 1972, 'Zoogeography and speciation of Australian desert lizards: an ecological perspective', *Copeia*, pp. 127-45.
- Piao, S., Liu, Q., Chen, A., Janssens, I.A., Fu, Y., Dai, J., Liu, L., Lian, X., Shen, M. & Zhu, X. 2019, 'Plant phenology and global climate change: Current progresses and challenges', *Global change biology*, vol. 25, no. 6, pp. 1922-40.
- Poulter, B., Frank, D., Ciais, P., Myneni, R.B., Andela, N., Bi, J., Broquet, G., Canadell, J.G., Chevallier, F., Liu, Y.Y., Running, S.W., Sitch, S. & van der Werf, G.R. 2014, 'Contribution of semi-arid ecosystems to interannual variability of the global carbon cycle', *Nature*, vol. 509, no. 7502, pp. 600-3.
- Qi, J., Moran, M., Cabot, F. & Dedieu, G. 1995, 'Normalization of sun/view angle effects using spectral albedo-based vegetation indices'.
- Qiu, B., Xue, Y., Fisher, J.B., Guo, W., Berry, J.A. & Zhang, Y. 2018, 'Satellite Chlorophyll Fluorescence and Soil Moisture Observations Lead to Advances in the Predictive Understanding of Global Terrestrial Coupled Carbon-Water Cycles', *Global Biogeochemical Cycles*, vol. 32, no. 3, pp. 360-75.
- Rammig, A. & Mahecha, M.D. 2015, 'Ecology: Ecosystem responses to climate extremes', *Nature*, vol. 527, no. 7578, p. 315.
- Ratzmann, G., Gangkofner, U., Tietjen, B. & Fensholt, R. 2016, 'Dryland Vegetation Functional Response to Altered Rainfall Amounts and Variability Derived from Satellite Time Series Data', *Remote Sensing*, vol. 8, no. 12.
- Reichstein, M., Bahn, M., Ciais, P., Frank, D., Mahecha, M.D., Seneviratne, S.I., Zscheischler, J., Beer, C., Buchmann, N., Frank, D.C., Papale, D., Rammig, A., Smith, P., Thonicke, K., van der Velde, M., Vicca, S., Walz, A. & Wattenbach, M. 2013, 'Climate extremes and the carbon cycle', *Nature*, vol. 500, no. 7462, pp. 287-95.
- Reichstein, M., Ciais, P., Papale, D., Valentini, R., Running, S., Viovy, N., Cramer, W., Granier, A., Ogee, J. & Allard, V. 2007, 'Reduction of ecosystem productivity and respiration during the European summer 2003 climate anomaly: a joint flux tower, remote sensing and modelling analysis', *Global Change Biology*, vol. 13, no. 3, pp. 634-51.
- Reid, N., Hill, S.M. & Lewis, D.M. 2008, 'Spinifex biogeochemical expressions of buried gold mineralisation: the great mineral exploration penetrator of transported regolith', *Applied Geochemistry*, vol. 23, no. 1, pp. 76-84.

- Reynolds, J.F., Smith, D.M.S., Lambin, E.F., Turner, B., Mortimore, M., Batterbury, S.P., Downing, T.E., Dowlatabadi, H., Fernández, R.J. & Herrick, J.E. 2007, 'Global desertification: building a science for dryland development', *science*, vol. 316, no. 5826, pp. 847-51.
- Roman, A. & Ursu, T. 2016, 'Multispectral satellite imagery and airborne laser scanning techniques for the detection of archaeological vegetation marks', *Landscape Archaeology on The Northern Frontier of The Roman Empire at Porolissum-An Interdisciplinary Research Project. Mega Publishing House*, pp. 141-52.
- Sanders, A., Verstraeten, W., Kooreman, M., van Leth, T., Beringer, J. & Joiner, J. 2016, 'Spaceborne Sun-Induced Vegetation Fluorescence Time Series from 2007 to 2015 Evaluated with Australian Flux Tower Measurements', *Remote Sensing*, vol. 8, no. 11.
- Schwalm, C.R., Williams, C.A., Schaefer, K., Baldocchi, D., Black, T.A., Goldstein, A.H., Law, B.E., Oechel, W.C. & Scott, R.L. 2012, 'Reduction in carbon uptake during turn of the century drought in western North America', *Nature Geoscience*, vol. 5, no. 8, pp. 551-6.
- Smith, W.K., Biederman, J.A., Scott, R.L., Moore, D.J.P., He, M., Kimball, J.S., Yan, D., Hudson, A., Barnes, M.L., MacBean, N., Fox, A.M. & Litvak, M.E. 2018, 'Chlorophyll Fluorescence Better Captures Seasonal and Interannual Gross Primary Productivity Dynamics Across Dryland Ecosystems of Southwestern North America', *Geophysical Research Letters*, vol. 45, no. 2, pp. 748-57.
- Song, L., Guanter, L., Guan, K., You, L., Huete, A., Ju, W. & Zhang, Y. 2018, 'Satellite sun-induced chlorophyll fluorescence detects early response of winter wheat to heat stress in the Indian Indo-Gangetic Plains', *Glob Chang Biol*.
- Stocker, T.F., Qin, D., Plattner, G.-K., Tignor, M.M., Allen, S.K., Boschung, J., Nauels, A., Xia, Y., Bex, V. & Midgley, P.M. 2014, 'Climate Change 2013: The physical science basis. contribution of working group I to the fifth assessment report of IPCC the intergovernmental panel on climate change', Cambridge University Press.
- Sun, Y., Frankenberg, C., Wood, J.D., Schimel, D.S., Jung, M., Guanter, L., Drewry, D.T., Verma, M., Porcar-Castell, A., Griffis, T.J., Gu, L., Magney, T.S., Kohler, P., Evans, B. & Yuen, K. 2017, 'OCO-2 advances photosynthesis observation from space via solar-induced chlorophyll fluorescence', *Science*, vol. 358, no. 6360.
- Sun, Y., Fu, R., Dickinson, R., Joiner, J., Frankenberg, C., Gu, L., Xia, Y. & Fernando, N. 2015, 'Drought onset mechanisms revealed by satellite solar-induced chlorophyll fluorescence: Insights from two contrasting extreme events', *Journal of Geophysical Research: Biogeosciences*, vol. 120, no. 11, pp. 2427-40.
- Thornton, P.K., Ericksen, P.J., Herrero, M. & Challinor, A.J. 2014, 'Climate variability and vulnerability to climate change: a review', *Global change biology*, vol. 20, no. 11, pp. 3313-28.
- Trenberth, K.E., Fasullo, J.T. & Shepherd, T.G. 2015, 'Attribution of climate extreme events', *Nature Climate Change*, vol. 5, no. 8, pp. 725-30.
- Tucker, C. 1979, 'The NDVI has been proven to be well correlated with various vegetation parameters, such as green biomass', *Rouse et al*, pp. 605-790.
- Ustin, S.L., Roberts, D.A., Gamon, J.A., Asner, G.P. & Green, R.O. 2004, 'Using imaging spectroscopy to study ecosystem processes and properties', *Bioscience*, vol. 54, no. 6, pp. 523-34.
- Van Gorsel, E., Wolf, S., Cleverly, J., Isaac, P., Haverd, V., Ewenz, C., Arndt, S.K., Beringer, J., Resco de Dios, V. & Evans, B. 2016, 'Carbon uptake and water use in woodlands and forests in southern Australia during an extreme heat wave event in the "angry Summer" of 2012/2013', *Biogeosciences*, vol. 13, no. 21, pp. 5947-64.
- Verger, A., Filella, I., Baret, F. & Peñuelas, J. 2016, 'Vegetation baseline phenology from kilometeric global LAI satellite products', *Remote Sensing of Environment*, vol. 178, pp. 1-14.
- Vetter, M., Churkina, G., Jung, M., Reichstein, M., Zaehle, S., Bondeau, A., Chen, Y., Ciais, P., Feser, F. & Freibauer, A. 2008, 'Analyzing the causes and spatial pattern of the European 2003 carbon flux anomaly using seven models'.

- Vicente-Serrano, S.M., Gouveia, C., Camarero, J.J., Beguería, S., Trigo, R., López-Moreno, J.I., Azorín-Molina, C., Pasho, E., Lorenzo-Lacruz, J. & Revuelto, J. 2013, 'Response of vegetation to drought time-scales across global land biomes', *Proceedings of the National Academy of Sciences*, vol. 110, no. 1, pp. 52-7.
- Walker, J., De Beurs, K. & Wynne, R. 2014, 'Dryland vegetation phenology across an elevation gradient in Arizona, USA, investigated with fused MODIS and Landsat data', *Remote Sensing of Environment*, vol. 144, pp. 85-97.
- Walther, S., Voigt, M., Thum, T., Gonsamo, A., Zhang, Y., Kohler, P., Jung, M., Varlagin, A. & Guanter, L. 2016, 'Satellite chlorophyll fluorescence measurements reveal large-scale decoupling of photosynthesis and greenness dynamics in boreal evergreen forests', *Glob Chang Biol*, vol. 22, no. 9, pp. 2979-96.
- Wang, C., Beringer, J., Hutley, L.B., Cleverly, J., Li, J., Liu, Q. & Sun, Y. 2019, 'Phenology Dynamics of Dryland Ecosystems Along the North Australian Tropical Transect Revealed by Satellite Solar-Induced Chlorophyll Fluorescence', *Geophysical Research Letters*.
- Wang, L., d'Odorico, P., Evans, J., Eldridge, D., McCabe, M., Caylor, K. & King, E. 2012, 'Dryland ecohydrology and climate change: critical issues and technical advances'.
- Wang, Q., Yang, Y., Liu, Y., Tong, L., Zhang, Q.-p. & Li, J. 2019, 'Assessing the impacts of Drought on Grassland net primary production at the Global Scale', *Scientific reports*, vol. 9, no. 1, pp. 1-8.
- Wu, P., Christidis, N. & Stott, P. 2013, 'Anthropogenic impact on Earth's hydrological cycle', *Nature Climate Change*, vol. 3, no. 9, pp. 807-10.
- Wu, X., Xiao, X., Zhang, Y., He, W., Wolf, S., Chen, J., He, M., Gough, C.M., Qin, Y. & Zhou, Y. 2018, 'Spatiotemporal Consistency of Four Gross Primary Production Products and Solar-Induced Chlorophyll Fluorescence in Response to Climate Extremes Across CONUS in 2012', *Journal of Geophysical Research: Biogeosciences*, vol. 123, no. 10, pp. 3140-61.
- Xie, Z., Huete, A., Cleverly, J., Phinn, S., McDonald-Madden, E., Cao, Y. & Qin, F. 2019, 'Multi-climate mode interactions drive hydrological and vegetation responses to hydroclimatic extremes in Australia', *Remote Sensing of Environment*, vol. 231.
- Xie, Z., Huete, A., Restrepo-Coupe, N., Ma, X., Devadas, R. & Caprarelli, G. 2016, 'Spatial partitioning and temporal evolution of Australia's total water storage under extreme hydroclimatic impacts', *Remote Sensing of Environment*, vol. 183, pp. 43-52.
- Xu, H.-j., Wang, X.-p., Zhao, C.-y. & Yang, X.-m. 2018, 'Diverse responses of vegetation growth to meteorological drought across climate zones and land biomes in northern China from 1981 to 2014', *Agricultural and Forest Meteorology*, vol. 262, pp. 1-13.
- Yang, J., Tian, H., Pan, S., Chen, G., Zhang, B. & Dangal, S. 2018, 'Amazon drought and forest response: Largely reduced forest photosynthesis but slightly increased canopy greenness during the extreme drought of 2015/2016', *Glob Chang Biol*, vol. 24, no. 5, pp. 1919-34.
- Yang, X., Tang, J., Mustard, J.F., Lee, J.-E., Rossini, M., Joiner, J., Munger, J.W., Kornfeld, A. & Richardson, A.D. 2015, 'Solar-induced chlorophyll fluorescence that correlates with canopy photosynthesis on diurnal and seasonal scales in a temperate deciduous forest', *Geophysical Research Letters*, vol. 42, no. 8, pp. 2977-87.
- Yang, Y., Long, D., Guan, H., Scanlon, B.R., Simmons, C.T., Jiang, L. & Xu, X. 2014, 'GRACE satellite observed hydrological controls on interannual and seasonal variability in surface greenness over mainland Australia', *Journal of Geophysical Research: Biogeosciences*, vol. 119, no. 12, pp. 2245-60.
- Yang, Z.-L., Dickinson, R.E., Shuttleworth, W.J. & Shaikh, M. 1998, 'Treatment of soil, vegetation and snow in land surface models: a test of the Biosphere-Atmosphere Transfer Scheme with the HAPEX-MOBILHY, ABRACOS and Russian data', *Journal of Hydrology*, vol. 212, pp. 109-27.
- Yoshida, Y., Joiner, J., Tucker, C., Berry, J., Lee, J.E., Walker, G., Reichle, R., Koster, R., Lyapustin, A. & Wang, Y. 2015, 'The 2010 Russian drought impact on satellite measurements of solar-induced chlorophyll fluorescence: Insights from modeling and comparisons with parameters derived from satellite reflectances', *Remote Sensing of Environment*, vol. 166, pp. 163-77.

- Yu, L., Wen, J., Chang, C.Y., Frankenberg, C. & Sun, Y. 2019, 'High-Resolution Global Contiguous SIF of OCO-2', *Geophysical Research Letters*, vol. 46, no. 3, pp. 1449-58.
- Zhang, Q., Kong, D., Shi, P., Singh, V.P. & Sun, P. 2018, 'Vegetation phenology on the Qinghai-Tibetan Plateau and its response to climate change (1982–2013)', *Agricultural and Forest Meteorology*, vol. 248, pp. 408-17.
- Zhang, Y., Joiner, J., Gentine, P. & Zhou, S. 2018, 'Reduced solar-induced chlorophyll fluorescence from GOME-2 during Amazon drought caused by dataset artifacts', *Global change biology*, vol. 24, no. 6, pp. 2229-30.
- Zhang, Y., Xiao, X., Jin, C., Dong, J., Zhou, S., Wagle, P., Joiner, J., Guanter, L., Zhang, Y., Zhang, G., Qin, Y., Wang, J. & Moore, B. 2016, 'Consistency between sun-induced chlorophyll fluorescence and gross primary production of vegetation in North America', *Remote Sensing of Environment*, vol. 183, pp. 154-69.
- Zscheischler, J., Mahecha, M.D., Von Buttlar, J., Harmeling, S., Jung, M., Rammig, A., Randerson, J.T., Schölkopf, B., Seneviratne, S.I. & Tomelleri, E. 2014, 'A few extreme events dominate global interannual variability in gross primary production', *Environmental Research Letters*, vol. 9, no. 3, p. 035001.
- Zuromski, L.M., Bowling, D.R., Köhler, P., Frankenberg, C., Goulden, M.L., Blanken, P.D. & Lin, J.C. 2018, 'Solar-Induced Fluorescence Detects Interannual Variation in Gross Primary Production of Coniferous Forests in the Western United States', *Geophysical Research Letters*, vol. 45, no. 14, pp. 7184-93.